



**Tightly-Coupled Image-Aided Inertial Navigation System via a Kalman  
Filter**

THESIS

Michael G. Giebner, Captain, USAF

AFIT/GE/ENG/03-10

**DEPARTMENT OF THE AIR FORCE  
AIR UNIVERSITY**

**AIR FORCE INSTITUTE OF  
TECHNOLOGY**

---

---

**Wright-Patterson Air Force Base, Ohio**

APPROVED FOR PUBLIC RELEASE; DISTRIBUTION UNLIMITED

The views expressed in this thesis are those of the author and do not reflect the official policy or position of the United States Air Force, Department of Defense or the United States Government.

AFIT/GE/ENG/03-10

Tightly-Coupled Image-Aided Inertial Navigation System via a  
Kalman Filter

THESIS

Presented to the Faculty of the  
Department of Electrical and Computer Engineering  
Graduate School of Engineering and Management

Air Force Institute of Technology

Air University

In Partial Fulfillment of the  
Requirements for the Degree of  
Master of Science in Electrical Engineering

Michael G. Giebner, B.S.

Captain, USAF

March, 2003

Approved for public release; distribution unlimited


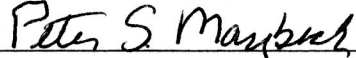
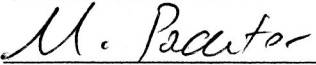
AFIT/GE/ENG/03-10

Tightly-Coupled Image-Aided Inertial Navigation System via a  
Kalman Filter

Michael G. Giebner, B.S.

Captain, USAF

Approved:

	<u>17 MAR 03</u>
Maj John F. Raquet Ph.D. Thesis Advisor	Date
	<u>17 MAR 03</u>
Dr. Peter S. Maybeck Ph.D. Committee Member	Date
	<u>March 17, 2003</u>
Dr. Meir Pachter Ph.D. Committee Member	Date

## *Acknowledgements*

I would like to acknowledge those who have helped me in the completion of this thesis. Thanks go to Major John Raquet for his expertise, guidance, and encouragement in helping make this thesis possible. Without long hours and his incredible expertise in debugging Matlab© code, I would still be attempting to defend this thesis. Thanks to Capt John Erickson for his donation of a Matlab© generated Kalman filter. I would also like to thank the other faculty members of the AFIT Electrical Engineering department, Dr. Peter Maybeck, Lt Col Mikel Miller, and Dr. Meir Pachter for their expert academic instruction and their patience when dealing with students.

There are not enough words in the world to express the gratitude I feel toward my AFIT “Peeps”. I was lucky enough to become friends with a great group of folks who made the AFIT experience not only bearable, but even downright fun at times. You guys rock: Heather Crooks, my Aussie pal Matt “Paps” Papaphotis, Greg “Gregarious Hibbidy Dibbidy” Hoffman, Dave “Crash, Bitter Dave” Garay, Christopher Hamilton and Kate, Christine Ellering, Scott and Bonnie Bergren, Mike and Gina Harvey, Ray “Buzz” and Theresa Toth, James “Haney” and Beth Hanley, and anyone else I managed to leave out (sorry about that).

Thanks go to the boys of USAF Test Pilot School class 02A. There is no way I would have made it through the  $2\frac{1}{2}$  year AFIT/TPS program without your help during the year at Edwards. You guys are the best. A special thanks goes to the Peeping Talon flight test team from 02A: Maj Bill “Ajax” Peris, Maj Jean Bilger (the coolest WSO in France), Maj Charles “DrEEvil” Havasy, Capt Stephen “Phürter” Frank, Capt Ron “Batta” Schwing, and Capt Clifton “Mojo” Janney.

Michael G. Giebner

## *Table of Contents*

	Page
Acknowledgements . . . . .	iii
List of Figures . . . . .	ix
List of Tables . . . . .	xi
List of Abbreviations . . . . .	xii
List of Symbols . . . . .	xiii
Abstract . . . . .	xiv
1. Introduction . . . . .	1-1
1.1 Background . . . . .	1-1
1.1.1 Inertial Navigation Systems . . . . .	1-2
1.1.2 GPS Systems . . . . .	1-3
1.1.3 Integrated INS/GPS Systems . . . . .	1-4
1.1.4 Current Trend in Navigation Systems . . . . .	1-5
1.1.5 How GPS Dependence Affects Aircraft . . . . .	1-5
1.1.6 How GPS Dependence Affects Munitions . . . . .	1-8
1.2 Problem to be Solved . . . . .	1-9
1.2.1 Do Visual Measurements Enhance Navigation Accuracy? . . . . .	1-9
1.3 Scope . . . . .	1-9
1.4 Literature Review . . . . .	1-10
1.4.1 Navigation Using Imaging Techniques . . . . .	1-10
1.5 Methodology . . . . .	1-11

	Page
1.6 Assumptions . . . . .	1-12
1.7 Materials and Equipment . . . . .	1-12
1.7.1 Air Force Flight Test Center . . . . .	1-12
1.7.2 Matlab© . . . . .	1-12
1.7.3 T-38A Aircraft . . . . .	1-13
1.7.4 GAINR . . . . .	1-13
1.7.5 Ashtech GPS Receiver . . . . .	1-14
1.7.6 Camera . . . . .	1-14
1.7.7 Camera Lenses . . . . .	1-14
1.7.8 Video Tapes . . . . .	1-14
1.7.9 Time Code Generator/Inserter . . . . .	1-14
1.7.10 Video Monitor . . . . .	1-15
1.8 Summary . . . . .	1-15
2. Background Theory . . . . .	2-1
2.1 Overview . . . . .	2-1
2.2 Kalman Filter Basics . . . . .	2-1
2.2.1 Kalman Filter . . . . .	2-1
2.2.2 Kalman Filter Equations . . . . .	2-1
2.2.3 Extended Kalman Filter . . . . .	2-4
2.2.4 State Vector . . . . .	2-5
2.2.5 State Covariance Matrix . . . . .	2-6
2.2.6 Dynamics Driving Noise Covariance Matrix . . . . .	2-7
2.2.7 State Transition Matrix . . . . .	2-7
2.2.8 Measurement Matrices . . . . .	2-7
2.2.9 Measurement Noise . . . . .	2-7
2.2.10 Kalman Filter Cycle . . . . .	2-7
2.3 Arc Length Equation . . . . .	2-9

	Page
2.3.1 Meridian Radius of Curvature . . . . .	2-9
2.3.2 Transverse Radius of Curvature . . . . .	2-10
2.4 Geometry . . . . .	2-10
2.4.1 Derivative of Inverse Tangent Function . . . . .	2-10
2.5 Navigation Orbit Geometry Determination . . . . .	2-12
2.5.1 Assumptions . . . . .	2-12
2.6 Summary . . . . .	2-12
3. Methodology . . . . .	3-1
3.1 Overview . . . . .	3-1
3.2 Visual Measurements . . . . .	3-1
3.3 Visual Measurement Generation . . . . .	3-2
3.4 Visual Measurement Error Estimation . . . . .	3-5
3.4.1 Generating the $\mathbf{H}(\hat{\mathbf{x}}^-)$ Matrix . . . . .	3-5
3.5 Visual Measurement Generation using a Camera . . . . .	3-7
3.5.1 Required Camera Specifications . . . . .	3-8
3.5.2 Generate Target Latitude/Longitude . . . . .	3-8
3.5.3 Generate Measurements from an Image . . . . .	3-13
3.5.4 Generate Measurement Estimates . . . . .	3-14
3.5.5 Camera-to-Body DCM Generation . . . . .	3-15
3.5.6 Visual Measurement $\mathbf{R}$ Matrix Generation . . . . .	3-15
3.5.7 Camera Calibration Procedures . . . . .	3-18
3.6 Estimation of Attitude Error States . . . . .	3-22
3.7 Summary . . . . .	3-23
4. Results and Analysis . . . . .	4-1
4.1 Sortie Overview . . . . .	4-1
4.2 General Filter Comments . . . . .	4-6



	Page
4.3 Unaided and Baro Filter Cases . . . . .	4-6
4.4 Different Cases . . . . .	4-7
4.5 Perfect Measurement Case . . . . .	4-9
4.6 Nominal Case . . . . .	4-10
4.7 Individual Axis Position Comparison . . . . .	4-12
4.8 Position State Error Comparison . . . . .	4-16
4.9 Velocity Comparison . . . . .	4-19
4.10 Velocity State Error Estimate Comparison . . . . .	4-20
4.11 Visual Residuals . . . . .	4-24
4.12 <b>R</b> Sensitivity Analysis . . . . .	4-28
4.13 Error Correlation with Angular Measurements . . . . .	4-32
4.14 Summary . . . . .	4-36
5. Conclusions and Recommendations . . . . .	5-1
5.1 Conclusions . . . . .	5-1
5.2 Recommendations . . . . .	5-1
Appendix A. Flight Test Methodology . . . . .	A-1
A.1 Overview . . . . .	A-1
A.2 Sortie Breakdown . . . . .	A-1
A.3 Prior to Flight . . . . .	A-1
A.4 Pre-flight and Taxi . . . . .	A-2
A.5 Takeoff . . . . .	A-2
A.6 Navigation Portion of Sortie . . . . .	A-2
A.7 Lessons Learned . . . . .	A-3
A.7.1 Ground Test . . . . .	A-3
A.7.2 Station Keeping During Circling Navigation Ma- neuver . . . . .	A-4

	Page
A.7.3 Things Do Not Always Work The Way They Are Supposed To Work . . . . .	A-4
A.7.4 Selected Target(s) Being Visible To Camera . . . . .	A-5
A.8 Summary . . . . .	A-6
Bibliography . . . . .	BIB-1
Vita . . . . .	VITA-1

*List of Figures*

Figure		Page
1.1.	PEEPING TALON T-38 . . . . .	1-13
2.1.	Kalman Filter Cycle . . . . .	2-8
3.1.	Sign Convention . . . . .	3-9
3.2.	Distances . . . . .	3-10
3.3.	Angles . . . . .	3-11
3.4.	Camera Calibration Target . . . . .	3-20
3.5.	Azimuth Error Surface . . . . .	3-21
4.1.	Ground Track . . . . .	4-2
4.2.	Altitude for Entire Sortie . . . . .	4-2
4.3.	Ramp Area and Navigation Orbit . . . . .	4-4
4.4.	GPS Filter Navigation Orbit . . . . .	4-5
4.5.	Navigation Orbit for Unaided Filter . . . . .	4-5
4.6.	3D Position Error for Unaided Filter (top) and Baro Filter (bottom) . . . . .	4-8
4.7.	Case 1 — 3D Position Error for Baro/Vis Filter . . . . .	4-9
4.8.	Case 1 — 3D Position Error for Vis Filter . . . . .	4-9
4.9.	Case 2 — 3D Position Error for Baro Filter . . . . .	4-10
4.10.	Case 2 — 3D Position Error for Baro/Vis Filter . . . . .	4-11
4.11.	Case 2 — 3D Position Error for Vis Filter . . . . .	4-11
4.12.	North Position Error for Unaided Filter (top), Baro Filter (middle), and Baro/Vis Filter (bottom). (Dashed Lines Indicate $\pm 1\text{-}\sigma$ Filter-Compensated Covariance) . . . . .	4-13

Figure		Page
4.13.	East Position Error for Unaided Filter (top), Baro Filter (middle), and Baro/Vis Filter (bottom). (Dashed Lines Indicate $\pm 1\text{-}\sigma$ Filter-Compensated Covariance) . . . . .	4-14
4.14.	Down Position Error for Unaided Filter (top), Baro Filter (middle), and Baro/Vis Filter (bottom). (Dashed Lines Indicate $\pm 1\text{-}\sigma$ Filter-Compensated Covariance) . . . . .	4-15
4.15.	State 1 (East) Position Error for Unaided Filter (top), Baro Filter (middle), and Baro/Vis Filter (bottom) . . . . .	4-17
4.16.	State 2 (North) Position Error for Unaided Filter (top), Baro Filter (middle), and Baro/Vis Filter (bottom) . . . . .	4-18
4.17.	North Velocity Error for Unaided Filter (top), Baro Filter (middle), and Baro/Vis Filter (bottom). (Dashed Lines Indicate $\pm 1\text{-}\sigma$ Filter-Compensated Covariance) . . . . .	4-21
4.18.	East Velocity Error for Unaided Filter (top), Baro Filter (middle), and Baro/Vis Filter (bottom). (Dashed Lines Indicate $\pm 1\text{-}\sigma$ Filter-Compensated Covariance) . . . . .	4-22
4.19.	Down Velocity Error for Unaided Filter (top), Baro Filter (middle), and Baro/Vis Filter (bottom). (Dashed Lines Indicate $\pm 1\text{-}\sigma$ Filter-Compensated Covariance) . . . . .	4-23
4.20.	State 4 (North) Velocity Error for Unaided Filter (top), Baro Filter (middle), and Baro/Vis Filter (bottom) . . . . .	4-25
4.21.	State 5 (East) Velocity Error for Unaided Filter (top), Baro Filter (middle), and Baro/Vis Filter (bottom) . . . . .	4-26
4.22.	Visual Residuals for the Baro/Vis Filter . . . . .	4-27
4.23.	3D Position Error for Cases 1 through 4 . . . . .	4-29
4.24.	3D Position Error for All Cases . . . . .	4-30
4.25.	Case 2 — Cost vs Benefit for Baro/Vis Filter . . . . .	4-31
4.26.	North Position Error and Angular Measurements . . . . .	4-33
4.27.	East Position Error and Angular Measurements . . . . .	4-34
4.28.	North and East Position Error . . . . .	4-35

*List of Tables*

Table		Page
3.1.	NED Frame Elevation and Azimuth Sense . . . . .	3-2
3.2.	Camera Frame Elevation and Azimuth Sense . . . . .	3-9
4.1.	Filter Configurations . . . . .	4-3
4.2.	Measurement Cases . . . . .	4-7
4.3.	Additional Measurement Cases . . . . .	4-28
A.1.	Modular Aircraft Components . . . . .	A-4

## *List of Abbreviations*

Abbreviation	Page
AFIT Air Force Institute of Technology . . . . .	1-1
TPS USAF Test Pilot School . . . . .	1-1
PVAT Position, Velocity, Attitude, and Time . . . . .	1-2
FLIR Forward-Looking Infrared . . . . .	1-3
HUD Heads Up Display . . . . .	1-3
LORAN Long-range Navigation . . . . .	1-3
RADAR Radio Detection and Ranging . . . . .	1-3
TACAN Tactical Air Navigation . . . . .	1-3
PVA Position, Velocity and Attitude . . . . .	1-4
HF High-Frequency . . . . .	1-6
ATC Air Traffic Control . . . . .	1-6
AWACS Airborne Warning and Control System . . . . .	1-7
JDAM Joint Direct Attack Munition . . . . .	1-8
JASSM Joint Air-to-Surface Standoff Missile . . . . .	1-8
JSOW Joint Stand-Off Weapon . . . . .	1-8
AFFTC Air Force Flight Test Center . . . . .	1-12
EKF Extended Kalman Filter . . . . .	2-4
$R_n$ Meridian Radius of Curvature . . . . .	2-9
$R_e$ Transverse Radius of Curvature . . . . .	2-10
NED North - East - Down . . . . .	3-1
DTED Digital Terrain Elevation Data . . . . .	3-2
DCM Direction Cosine Matrix . . . . .	3-12
SI Special Instrumentation . . . . .	A-2
RCA Radio Corporation of America . . . . .	A-3

*List of Symbols*

Symbol	Page
$\hat{\mathbf{x}}$ State Vector . . . . .	2-5
$\mathbf{P}$ State Covariance Matrix . . . . .	2-6
$\mathbf{Q}_d$ Dynamics Driving Noise Matrix . . . . .	2-7
$\Phi$ State Transition Matrix . . . . .	2-7
$\mathbf{h}(\hat{\mathbf{x}})$ Nonlinear Measurement Matrix . . . . .	2-7
$\mathbf{H}$ Linearized Measurement Matrix . . . . .	2-7
$\mathbf{R}$ Measurement Noise Matrix . . . . .	2-7

## *Abstract*

Inertial navigation systems and GPS systems have revolutionized the world of navigation. Inertial systems are incapable of being jammed and are the backbone of most navigation systems. GPS is highly accurate over long periods of time, and it is an excellent aid to inertial navigation systems. However, as a military force we must be prepared to deal with the denial of the GPS signal. This thesis seeks to determine if, via simulation, it is viable to aid an INS with visual measurements. Visual measurements represent a source of data that is essentially incapable of being jammed, and as such they could be highly valuable for improving navigation accuracy in a military environment.

The simulated visual measurements are two angles formed from the aircraft with respect to a target on the ground. Only one target is incorporated into this research. Five different measurement combinations were incorporated into a Kalman filter and compared to each other over a six-minute circular navigation orbit. The measurement combinations included were with respect to the navigation orbit: 1) GPS signals throughout the orbit, 2) no measurements during the orbit, 3) simulated barometric measurements during the orbit, 4) simulated barometric and visual measurements during the orbit, 5) and visual measurements only during the orbit.

The visual measurements were shown to significantly improve navigation accuracy during a GPS outage, decreasing the total 3-dimensional error after six minutes without GPS from 350m to 50m (with visual measurements). The barometric/visual measurement formulation was the most accurate non-GPS combination tested, with the pure visual measurement formulation being the next best visual measurement configuration. The results obtained indicate visual measurements can effectively aid an INS. Ideas for follow-on work are also presented.



# Tightly-Coupled Image-Aided Inertial Navigation System via a Kalman Filter

## *1. Introduction*

This thesis is the culmination of a course of study at the Air Force Institute of Technology (AFIT) in navigation theory, along with a year at USAF Test Pilot School (TPS). The academic portion dealt with the incorporation of visual measurements into a navigation Kalman filter. This work was performed at AFIT. The actual flight test took place within the TPS curriculum. The flight test (project PEEPING TALON [2]) supported the AFIT research and also a limited evaluation of a camera system on the T-38 aircraft (the aircraft was specifically modified for this test). Certain difficulties led to the use of simulated visual measurements rather than measurements from the collected images.

### *1.1 Background*

This research is in the area of navigation, which is the art and science of moving from one place to another. The type and quality of system(s) used determines the accuracy with which the navigation occurs. Many different systems have been used for navigation. Two of these systems are considered mainstays of modern navigation. These systems are the inertial navigation system (INS) [18] and the Global Positioning System (GPS) [18:371]. This research investigates the incorporation of a new type of visual measurement with the aforementioned two navigation systems. The INS and GPS systems are described in limited detail in Sections 1.1.1 and 1.1.2, while the visual measurements and their effects are discussed in much greater detail, as they are the thrust of this research.

*1.1.1 Inertial Navigation Systems.* Inertial systems sense specific force and rotation. These force and rotation measurements are combined with knowledge about the Earth's rotation and gravitational field and can be used to determine vehicular movement.

The most important components in an INS are accelerometers, gyroscopes and a computer. The accelerometers and gyroscopes are sensors which provide specific force and angular velocity measurements, respectively. These measurements are used by the computer to generate vehicle position, velocity, attitude and time (PVAT) in a chosen coordinate reference frame by using the necessary navigation equations for that frame. The computer is used for required computations and to track vehicle movement. Inertial systems have become vital aircraft systems tied to the efficient mission performance of civil and military aircraft. In many cases they would be unable to perform their missions at all without an INS. These inertial navigation systems are very effective and offer many advantages.

One of the main benefits of inertial systems is their passive nature. They emit no detectable signature and are incapable of being jammed. However, inertial systems require several key items to be effective. The first item is accurate position information during alignment. Any position error during alignment will grow over time (and there is always a position error between that entered into the INS and the actual position). This rate of growth is associated with the quality of the gyroscopes. A large alignment error with high-quality gyroscopes might actually be better than a small alignment error with low-quality gyroscopes. These systems also require a lengthy alignment time. If both of these requirements are not met, even the most accurate INS can be, or become, worthless. The quality of the accelerometers and gyroscopes are another source of error. Even the highest quality sensors are prone to some error. All of these errors integrate, and an INS system will drift away from its actual position over time. The INS drift problem brought about the need to update the INS during long flights. The updates provided by these outside, additional

measurements, are used to improve INS accuracy by bounding, or damping, the error growth inherent to the INS. However, some of these measurements are cumbersome to obtain or not always available. Some of these types of update measurements are [6:293-294]:

1. Altitude sensors
  - (a) Barometric Altimeter
  - (b) Radar Altimeter
2. Forward-Looking Infrared (FLIR)
3. GPS
4. Heads Up Display (HUD)
5. Long-Range Navigation (LORAN)
6. Radio Detection and Ranging (RADAR)
7. Star Trackers
8. Tactical Air Navigation (TACAN)
9. Overflying a known geographical point

Historically, new types of measurements have been integrated into the INS solution as they have become available. One of the best measurements for aiding an INS was provided by GPS.

*1.1.2 GPS Systems.* The Global Positioning System is a system of satellites in medium earth orbit that transmits signals to receivers on the Earth's surface, or flying in the earth's atmosphere, or even in space. These receivers are capable of determining their own position if at least four satellites are visible to that particular receiver. GPS systems do not require any alignment time (other than that required to lock onto the satellite signals) since there are no internal mechanical components.

GPS is highly accurate, does not drift over time, and is almost continuously available for many typical applications. Therefore, GPS is a very promising new type of measurement for integration with an INS. This was mainly due to the error characteristics of the GPS being beneficial in limiting INS weaknesses (most notably the INS errors growing or drifting over time).

*1.1.3 Integrated INS/GPS Systems.* It was seen above that INS systems have strengths and weaknesses, as do GPS systems. INS systems are very accurate over short periods of time (i.e., they are sensitive to high frequency dynamics), and their error characteristics grow slowly over time. The INS is capable of generating vehicle body orientation (which is very important in aircraft and submarines for which outside visual references may be unavailable). GPS systems are not highly accurate over short periods of time, but they are over long periods of time. They are not capable of generating vehicle body orientation (unless multiple antennas are used along with some additional processing). Luckily, INS weaknesses are compensated for by GPS strengths, and GPS weaknesses are compensated by INS strengths. As a result, these systems are often integrated together to take advantage of these strengths and reduce their individual weaknesses [6:342]. This is typically accomplished via a Kalman filter (see Chapter 2 for a discussion on Kalman filters). There are different ways to integrate INS and GPS [13], but the method used in this research is the only method that will be described in this thesis. The method that is used is a tightly-coupled integration. The GPS measurement is a pseudorange measurement from each visible satellite. The INS generates its own estimate of this same pseudorange measurement. These two measurements are differenced to obtain a “measurement”, which is then the input into the error state Kalman filter. This method of integration offers two advantages. First, even a single satellite can be used to update position, velocity and attitude (PVA), rather than the four being required for the GPS itself to determine its own position (such a GPS-alone solution is required in an alternative integration method known as “loose-coupling”). Second,

the measurement is still in its raw form and has not been previously processed by another filter. Kalman filters work better with raw measurements than with data that has already been processed [17:292]. Such tightly-coupled INS/GPS systems can be highly accurate; however, their reliance on GPS can lead to potential problems.

*1.1.4 Current Trend in Navigation Systems.* Many military systems have become heavily GPS-dependent. The trend is toward low-cost, lower quality inertial systems that are integrated with GPS. This is especially true in the realm of micro-electro mechanical systems (MEMS), in which high quality inertial systems are not currently available due to technological limitations. Economics might drive the low-cost, lower quality inertial systems even after the technological limitations have been overcome. This is even true in the world of aircraft. The C-141C navigation system relies on GPS so heavily that the original INS equipment from the C-141B was retained in the system and integrated with GPS (even though the original INS systems were old and not terribly accurate). This was deemed appropriate, due to the accuracies involved with GPS. In such systems, problems arise in the event of a GPS outage, and this is the primary motivation for this research. The potential problems caused by a GPS outage are discussed below in Sections 1.1.5 and 1.1.6.

*1.1.5 How GPS Dependence Affects Aircraft.* Typical aircraft sortie durations vary from approximately an hour to many hours of flight time. Inertial errors grow over time unless they are corrected in some way, and this is where GPS shows its strengths. However, a problem arises when the GPS signal is no longer available. These effects are felt throughout the spectrum of aircraft type, as described below (with a military emphasis).

*1.1.5.1 How GPS Loss Affects Strategic Airlift.* A typical strategic airlifter mission can easily last eight hours or longer, and can have an ocean crossing during the flight. Loss of the GPS signal and reliance on the on-board INS systems

can negatively impact two important areas. First, lack of radar coverage over the world's oceans causes aircraft deconfliction to be implemented by assigning aircraft to fly pre-determined routes at specific altitudes. This is performed via voice or data communication over high-frequency (HF) radio waves. There is no way to determine if an airplane is where it is supposed to be, other than its own on-board systems. An aircraft could easily be misplaced on the jet route as it unknowingly reports a faulty location to air traffic control (ATC). The aircraft could even be completely off the jet route. The second area impacted by GPS signal loss is coastal penetration. Aircraft "coasting in" to another country are required to pass over certain areas so they can be controlled and de-conflicted with other air traffic. An aircraft using only an INS could easily "coast in" miles from the intended location.

*1.1.5.2 How GPS Loss Affects Tactical Airlift.* Tactical airlifters don't often travel the same distances strategic airlifters do, but they suffer from their own particular navigation problems. Aircraft like the C-130 and other special operations aircraft are often required to transit areas in a clandestine manner at night, while offering minimal emissions to the outside world. This difficulty is sometimes compounded by having to perform this mission over featureless expanses of water or desert, while retaining the need to arrive at a particular location without error. INS-only systems cannot typically perform this type of mission if the flying time approaches even one hour.

*1.1.5.3 How GPS Loss Affects Tactical Fighters.* Tactical fighters are often required to take off at night, fly over enemy territory without being detected, attack targets and return home without being shot down. Aircraft of this type often fly under high g-forces, in extreme attitudes, and these flight conditions can change very rapidly. Such an environment can make it even more difficult for an inertial system to operate accurately. PVAT is extremely important to these types of aircraft, as they are often required to pass this information to munitions before they can be

released from the host aircraft. Errors in the aircraft's navigation solution naturally translate directly to a weapon.

*1.1.5.4 How GPS Loss Affects Datalink Systems.* Datalink is becoming much more predominant, and this area offers some very unique challenges. Aircraft are becoming capable of transmitting and receiving very useful information while in-flight. This information comes in many forms:

1. Wingman location
2. Radar data to include radar lock and weapon fly-out information
3. Target location
4. Downed pilot location
5. Ground threats
6. Friendly or neutral ground personnel

Some of this information requires very accurate position data; otherwise it is not only useless, it can lead aircrew into potentially dangerous situations or geographical areas. One particular area of concern is the geographic correlation of data. This is an extremely complex task, and this must often occur between dissimilar platforms. Accurately passing coordinates between aircraft is one basis for correlating two separate sources of data into one. This correlation can increase the accuracy of the information known about the target aircraft (position, velocity, heading, radar parameters, etc). A certain amount of navigation error could cause the previously mentioned correlation to not occur. For example, a hostile contact reported by an airborne warning and control system (AWACS) aircraft to a fighter aircraft via datalink might not properly resolve with the fighter aircraft's own radar detection of the same hostile contact if one of the aircraft has navigation errors. This would cause both contacts to appear on the fighter aircraft radar scope. This can cause a great deal of confusion, and cause the fighter aircraft to waste time, energy, and

even weapons on a false target. This false target could even potentially drive tactical decisions. There are many other similar issues related to the datalink area. It is safe to say that navigation errors cause significant problems for datalink systems.

*1.1.6 How GPS Dependence Affects Munitions.* Many of the new weapons being developed for the US Air Force (USAF) are also heavily GPS-dependent. These weapons fill a much-needed niche that cannot be filled by the highly accurate laser guided bombs (LGB) already in the inventory. LGBs are not all-weather weapons. The target must be visible to the laser designator, and must be visible to the weapon a pre-determined time and distance from the target. This time and distance is largely dependent on the type of weapon and the geometry of the attack. The new GPS weapons are all-weather weapons that are not restricted by cloud cover, high humidity, or other problems associated with LGBs. Many of these new systems are mated with low-cost inertial systems. Therefore, these systems require either a short operating duration to keep the INS errors from drifting, or they must be integrated with GPS. The problem occurs when the flight duration is long and/or the GPS signal is lost. In such cases, the inertial errors grow rapidly until the PVA solution is no longer usable. Some of these new munitions are the Joint Direct Attack Munition (JDAM) [12], Joint Air-to-Surface Standoff Missile (JASSM) [10] and Joint Stand-off Weapon (JSOW) [11]. Some of these weapons are essentially point weapons, in that they need to hit very close to the target to be effective. A loss of GPS during the weapon fall time could cause the weapon to be completely ineffective by missing the target. This miss distance need not be very large for a point weapon to lose effectiveness. Even some of the area munitions could potentially hit far enough away from their intended impact point to be ineffective. A new type of visual measurement might help alleviate some of the problems associated with GPS signal loss by keeping the INS from drifting during a long fall time. Visual measurements could also be used with a target recognition system to refine the desired impact point as the weapon approaches a target.



## 1.2 *Problem to be Solved*

*1.2.1 Do Visual Measurements Enhance Navigation Accuracy?* It has been shown that INS/GPS systems are vulnerable to loss of the GPS signal (especially those systems outfitted with low-cost inertial equipment). Many of these systems are equipped with, or could be equipped with, visual sensors of some type. This visual equipment could be used to provide measurements to the navigation Kalman filter to update the navigation solution. These measurements could increase accuracy at all times (with and without GPS being available), but could prove invaluable during times of GPS system outages. A system of this type could also be used to determine target coordinates passively. This research seeks to determine the answers to these questions.

Specifically, simulated visual measurements will be incorporated into the navigation Kalman filter, with and without GPS, and compared to a truth source to determine if the inclusion of the visual measurements increases navigation system performance. These simulated measurements will be generated during a portion of the sortie when the aircraft is orbiting around a particular target area. This is so the same target area will be available to generate measurements that do not disappear from view.

## 1.3 *Scope*

This research is a navigation thesis and not a signal processing one. Therefore, no effort was made to obtain visual measurements via digital techniques. There are methods available, but they can be difficult and time consuming to implement. Some of these methods will be briefly reviewed in the Literature Review section (Section 1.4). Actual visual measurements were extracted even though simulated data was used in the analysis. A simple hand/eye technique was used to capture this data. This data is available, and it will be incorporated into the filter at a later time.

The data was post-processed, due to the increased burden imposed by real-time processing.

#### *1.4 Literature Review*

There is an abundance of research regarding navigation, motion estimation using visual techniques, and a combination of the two topics. Much of the latter research is limited to ground navigation or image identification and is fundamentally different than that proposed in this work. Also, much of the research is focused on the optical area only, and does not incorporate inertial systems, GPS or Kalman filter theory. The term navigation, as it is used in many of these articles, refers to the ability to move around in some autonomous fashion, but does not refer to the type of navigation used here, i.e., generating PVAT via an aided-INS.

*1.4.1 Navigation Using Imaging Techniques.* Current theory breaks motion estimation into two parts [9, 15], determining inter-frame image motion and using image motion to estimate camera motion. So, inter-frame image motion is typically determined by either the optic flow constraint equation (Equation (1.1)) or some type of correspondence (matching) technique. Some estimate of motion from frame to frame is generated via the first step, and this information is used in the second step to back out the motion of the camera. Whether Equation (1.1) or a matching technique is used, the end process generates measurements that can be incorporated into a Kalman filter. This research will implement a simplistic matching technique.

1.4.1.1 *Optic Flow Constraint Equation Techniques.* The first type of inter-frame motion estimation technique relies upon solving the optic flow constraint equation, Equation (1.1) [19]:

$$-\frac{\partial E}{\partial t} = \nabla E \cdot v \quad (1.1)$$

where:

$E$  is intensity

$\nabla E$  is the gradient of the intensity

$v$  is object velocity

Optic flow is the apparent motion of brightness patterns in an image [1, 19]. This method generates a motion vector for each element in the image. Some of the methods reviewed produced vectors that were wildly inaccurate and unusable due to camera shock, vibration and inherent inadequacies in the optic flow estimation technique. The second type of inter-frame motion estimation techniques are correspondence techniques.

1.4.1.2 *Correspondence Based Techniques.* This technique is a matching type of solution, and it also uses apparent motion of image brightness patterns. However, motion vectors are not generated for each image element. Objects are identified in one image and located again in the preceding images. The displacement between objects over time is used to estimate the inter-frame velocity, whether it be translational and/or rotational velocity.

## 1.5 Methodology

The original idea was to use a simple technique on a sequence of images to generate angular information for incorporation into the Kalman filter. The accuracy increase due to these measurements was to be determined experimentally using data obtained during the flight test phase of project PEEPING TALON at TPS. This would be accomplished by comparing system accuracy with visual measurements

being incorporated, to system accuracy without visual measurements being incorporated. This data was collected, but difficulties with the Kalman filter algorithm and several technical problems caused simulated data to be generated, and used, for the actual analysis of the algorithm. The flight test images will be incorporated into the navigation system once the technical difficulties have been overcome.

### *1.6 Assumptions*

It is assumed that readers are familiar with the field of navigation so certain topics are discussed without an in-depth background tutorial, i.e., Kalman filters, Inertial Navigation Systems, Global Positioning System, etc. The reader is directed to references [6], [7], [14], and [18] for a more in-depth review of the material presented here.

Images are assumed to be planar. No attempt is made to compensate for altitude changes in scene objects or local changes in the earth's surface. These simplifications will inject some error into the process of generating measurements with a camera.

### *1.7 Materials and Equipment*

*1.7.1 Air Force Flight Test Center.* The Air Force Flight Test Center (AFFTC) provided a many resources for the PEEPING TALON flight test. These resources included: range airspace, T-38 aircraft, aircraft modification engineering support, maintenance equipment and maintenance personnel.

*1.7.2 Matlab©.* Matlab© was used at AFIT to design the Kalman filter [5]. This was due to familiarity with the software since much of the curriculum at AFIT involved the use of this particular software package. It was also used after TPS for further algorithm development and data analysis [4].

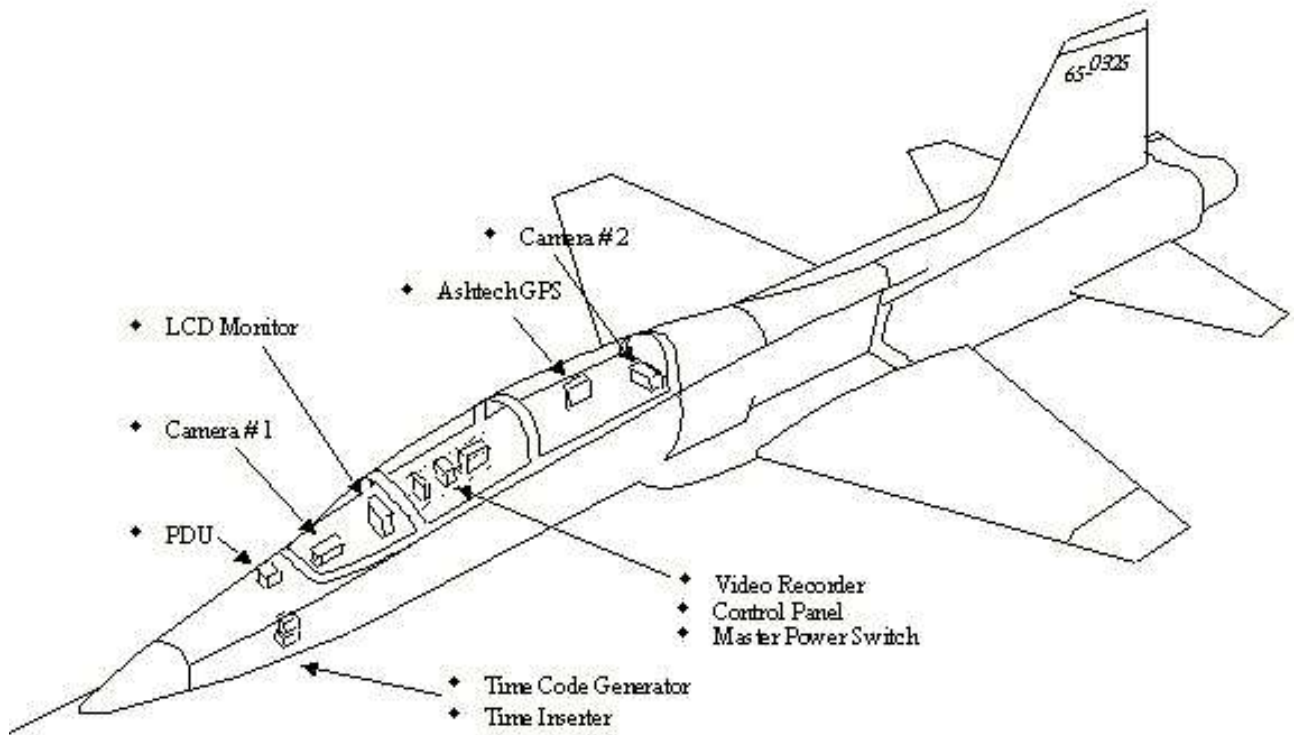


Figure 1.1 PEEPING TALON T-38

1.7.3 *T-38A Aircraft.* A T-38A aircraft, tail number 65-10325, was modified to support the PEEPING TALON test program. The test system included navigation, video, and recording components. It consisted of a GPS-Aided Inertial Navigation Reference system (GAINR), an Ashtech GPS receiver, two model 71A video cameras, a liquid crystal display (LCD) cockpit monitor, and a digital recording system.

1.7.4 *GAINR.* The GAINR system consisted of an Embedded GPS/INS (EGI), a Pre-Flight Panel (PFP), a Cockpit Control Panel (CCP), and an Intelligent Flash-memory Solid State Recorder (IFSSR). The GAINR recorded raw Inertial

Measurement Unit (IMU) data ( $\Delta v$  and  $\Delta\theta$ ) at a 256 Hz rate and a blended EGI position solution at a 64 Hz rate to an internal data card.

*1.7.5 Ashtech GPS Receiver.* The Ashtech Z-Surveyor was a 12-channel, dual frequency GPS receiver with a built-in battery and removable PC memory card. This receiver was capable of providing raw GPS signal data on the internal data card for post-processing. These data were stored at a 2 Hz rate. A second Ashtech GPS receiver was used to collect stationary data for differential GPS data purposes.

*1.7.6 Camera.* Both the forward and side cameras were Model 71A Ball Aerospace cameras. They were ruggedized all light level, high-performance, Gated Intensified Charge Coupled Device monochrome cameras. These cameras used a 3rd generation intensifier coupled to a 768 (H) x 484 (V) pixel interline charge coupled device image sensor. The analog video output contained 525 lines at a field rate of 60 Hz, a frame rate of 30 Hz, and with 2:1 positive interlace. The cameras operated from 28 volts direct current with a power consumption of less than 6 watts. Camera dimensions were 5 x 2.5 x 2 inches (L x H x W), and each weighed 1.1 pounds.

*1.7.7 Camera Lenses.* The collection of lenses used had three different fields-of-view. These were standard type video camera lenses, in that they were not optimized for night video even though the PEEPING TALON test collected video under low-light conditions using low-light cameras. The airborne video recorder was a Sony Digital Video Cassette Recorder, model GV-D300.

*1.7.8 Video Tapes.* The tapes used in the airborne video recorder were Panasonic mini-DV ME 80/120 cassettes. Recording was performed in the SP record mode as this was the highest image resolution mode.

*1.7.9 Time Code Generator/Inserter.* The GPS time code generator, Datum model 9390-3000, received the GPS signal from the externally mounted GPS

antenna and converted it to a digital format for the video time code inserter. The video time code inserter, Datum model 9559-835, received GPS data from the GPS time code generator and the video signal from the selected camera. The video time code inserter combined these two data streams to provide a single output, which was a video picture with GPS time in the bottom right hand corner of the video image. This enabled the test team to determine the precise GPS time when each frame of video was recorded.

*1.7.10 Video Monitor.* The video monitor for the front seat was a 5-in. Transvideo International Rainbow II LCD Monitor. The monitor was mounted on the front cockpit glare shield, and was rotated right approximately 40 degrees (in a clockwise direction). The video selector switch located in the front cockpit controlled which camera was displayed on the monitor and recorded on the video recorder.

## *1.8 Summary*

The previous was a broad overview of the work contained in the thesis effort and the flight test to collect the data. Basic navigation and aiding concepts were presented along with the problem at hand and the strategy for solving the problem. Where this thesis fits into the overall AFIT and TPS education programs was discussed, as well as a short literature review, project assumptions, and material/equipment intended for use in solving the problem. The groundwork is now in place to begin with project specifics beginning with Chapter 2, Background Theory. The specific design of the visual measurements are presented in Chapter 3. Chapter 4 covers the results obtained during the research as well as an analysis of those results. Chapter 5 wraps up the research and lays out follow-on work that could be accomplished. Appendix A covers the actual flight test that occurred at USAF Test Pilot School.

## 2. Background Theory

### 2.1 Overview

This chapter covers theory that is referenced in Chapter 3. Kalman filter basics are covered briefly, along with geometry relating to the shape of the Earth, the arc length equation, other necessary geometry equations, and a description of the technique used to generate the flight profile for the navigation orbit. The notation used throughout this work that pertains to the Kalman filter is taken from the three-course Stochastic Estimation and Control sequence at AFIT which uses the texts written by Dr Peter Maybeck. Vectors are bolded lower-case while matrices are bolded upper-case [6, 7].

### 2.2 Kalman Filter Basics

*2.2.1 Kalman Filter.* A Kalman filter takes a dynamic model of the system, measurements, deterministic inputs, and adds in statistical descriptions of the uncertainties in each of these and blends them together with real-world data to generate the best possible estimate of certain variables of interest. Linear Kalman filter equations are used and presented below with a brief explanation. This research encounters some nonlinearities in the measurements, and the method of dealing with this problem is also presented. Refer to [6, 7, 17] for a more lengthy derivation of Kalman filters.

*2.2.2 Kalman Filter Equations.* The system model in this research is a linear, time-invariant, discrete time system in the form of Equation (2.1), where  $\mathbf{x}(t_i)$  is an (n x 1) state process vector,  $\Phi(t_i, t_{i-1})$  is an (n x n) system transition matrix,  $\mathbf{G}_d(t_{i-1})$  is an (n x s) noise input matrix, and  $\mathbf{w}_d(t_{i-1})$  is an (s x 1) white Gaussian noise vector [3:2-2].

$$\mathbf{x}(t_i) = \Phi(t_i, t_{i-1})\mathbf{x}(t_{i-1}) + \mathbf{G}_d(t_{i-1})\mathbf{w}_d(t_{i-1}) \quad (2.1)$$



The discrete-time dynamics driving noise vector  $\mathbf{w}_d(t_{i-1})$  is assumed to be white, Gaussian, with a mean and covariance described by [3:2-3]:

$$E[\mathbf{w}_d(t_i)] = \mathbf{0} \quad (2.2)$$

$$E[\mathbf{w}_d(t_i)\mathbf{w}_d^T(t_j)] = \begin{cases} \mathbf{Q}_d & \text{for } t_i = t_j \\ \mathbf{0} & \text{for } t_i \neq t_j \end{cases} \quad (2.3)$$

Nonlinear measurements are available and are modelled by Equation (2.4), where  $\mathbf{z}(t_i)$  is an  $(m \times 1)$  measurement vector,  $\mathbf{h}[\mathbf{x}(t_i), t_i]$  is an  $(m \times 1)$  nonlinear measurement model vector, and  $\mathbf{v}(t_i)$  is an  $(m \times 1)$  white Gaussian measurement noise vector [3:2-6]

$$\mathbf{z}(t_i) = \mathbf{h}[\mathbf{x}(t_i), t_i] + \mathbf{v}(t_i) \quad (2.4)$$

The discrete-time noise vector  $\mathbf{v}(t_i)$  is assumed to be white, Gaussian, with a mean and covariance described by [3:2-6]:

$$E[\mathbf{v}(t_i)] = \mathbf{0} \quad (2.5)$$

$$E[\mathbf{v}(t_i)\mathbf{v}^T(t_j)] = \begin{cases} \mathbf{R}(t_i) & \text{for } t_i = t_j \\ \mathbf{0} & \text{for } t_i \neq t_j \end{cases} \quad (2.6)$$

Kalman filter equations can be broken up into three major categories: initial condition information, filter propagation, and filter update. Equations for each of these categories are presented below.

*2.2.2.1 Kalman Filter Initial Condition Equations.* Equation (2.7) provides the best information available about each of the states at the beginning of filter operation [6:217], while Equation (2.8) describes the initial covariance matrix,

which provides the best information available about the uncertainty in each of the states at the beginning of filter operation [6:217].

$$\hat{\mathbf{x}}(t_0) = E\{\mathbf{x}(t_0)\} = \hat{\mathbf{x}}_0 \quad (2.7)$$

$$\mathbf{P}(t_0) = E\{[\mathbf{x}(t_0) - \hat{\mathbf{x}}_0][\mathbf{x}(t_0) - \hat{\mathbf{x}}_0]^T\} = \mathbf{P}_0 \quad (2.8)$$

*2.2.2.2 Kalman Filter Propagation Equations.* Equation (2.9) is used to propagate the states forward in time from the initial conditions or the last measurement update, whichever is the case. This continues until a measurement is available for incorporation into the Kalman filter [3:2-4].

$$\hat{\mathbf{x}}(t_i^-) = \mathbf{\Phi}(t_i, t_{i-1})\hat{\mathbf{x}}(t_{i-1}^+) \quad (2.9)$$

Equation (2.10) is used to propagate the state covariance forward in time from the initial conditions or the last measurement update, whichever is the case. This continues until a measurement is available for incorporation into the Kalman filter [3:2-4].

$$\mathbf{P}(t_i^-) = \mathbf{\Phi}(t_i, t_{i-1})\mathbf{P}(t_{i-1}^+)\mathbf{\Phi}^T(t_i, t_{i-1}) + \mathbf{G}_d(t_{i-1})\mathbf{Q}_d(t_{i-1})\mathbf{G}_d^T(t_{i-1}) \quad (2.10)$$

2.2.2.3 *Kalman Filter Update Equations.* The Kalman filter gain equation (Equation (2.11)) is used to weight a measurement for incorporation into the Kalman filter. The relative uncertainty between the optimal estimates of what the states should be and the actual measurements determines their respective weighting [6:259].

$$\mathbf{K}(t_i) = \mathbf{P}(t_i^-) \mathbf{H}^T[t_i, \hat{\mathbf{x}}(t_i^-)] [\mathbf{H}[t_i, \hat{\mathbf{x}}(t_i^-)] \mathbf{P}(t_i^-) \mathbf{H}^T[t_i, \hat{\mathbf{x}}(t_i^-)] + \mathbf{R}(t_i)]^{-1} \quad (2.11)$$

where the  $\mathbf{H}[t_i, \hat{\mathbf{x}}(t_i^-)]$  matrix is generated by [3:2-10]:

$$\mathbf{H}[t_i, \hat{\mathbf{x}}(t_i^-)] = \left[ \frac{\partial \mathbf{h}[\mathbf{x}, t_i]}{\partial \mathbf{x}} \right]_{\mathbf{x}=\hat{\mathbf{x}}(t_i^-)} \quad (2.12)$$

The state update Equation (2.13) is used to update each of the states whenever a measurement is available [3:2-10], while Equation (2.14) is used to update the state covariance matrix each time a measurement is available [3:2-10].

$$\hat{\mathbf{x}}(t_i^+) = \hat{\mathbf{x}}(t_i^-) + \mathbf{K}(t_i) [\mathbf{z}_i - \mathbf{h}[\hat{\mathbf{x}}(t_i^-), t_i]] \quad (2.13)$$

$$\mathbf{P}(t_i^+) = \mathbf{P}(t_i^-) - \mathbf{K}(t_i) \mathbf{H}[t_i, \hat{\mathbf{x}}(t_i^-)] \mathbf{P}(t_i^-) \quad (2.14)$$

2.2.3 *Extended Kalman Filter.* An Extended Kalman Filter (EKF) incorporates nonlinearities in the system model, the measurements, or both, and is an extension of the aforementioned Kalman filter (hence the name). The basic idea is to linearize the nonlinear measurements, or dynamics models, about a redeclared nominal trajectory or point at certain intervals so linear Kalman filter concepts can be used. This is valid if the nonlinearity is not too great and/or if linearization errors remain small [7:41].

As stated previously, Kalman filters work best when using raw measurements as opposed to measurements that are pre-processed. Pre-processing measurements

creates time-correlation in the measurement noises, and this must be resolved. One way to deal with this problem is to incorporate measurements with enough time lapse between epochs that the assorted measurement noises are no longer time-correlated. Another method is to model the time-correlated noise with a linear system driven by white Gaussian noise [6:183]. Otherwise, one of the basic Kalman filter assumptions is violated, i.e., a linear system driven by white Gaussian noise [6:8].

*2.2.4 State Vector.* A Kalman filter is used to estimate variables of interest. These variables are contained in the  $(n \times 1)$  dimension state vector ( $\hat{\mathbf{x}}$ ) where the caret symbol is called a “hat” and indicates the variable under the symbol is an estimate and not the actual value. Therefore, the state vector  $\hat{\mathbf{x}}$  is an estimate of the actual state vector  $\mathbf{x}$ . The “n” in the  $(n \times 1)$  referenced above is the number of states being estimated. The state vector may be the actual variables of interest (a direct, or total state filter). These actual variables might be position and velocity of a vehicle. For an error state (or indirect) filter, the errors in the actual variables of interest are estimated. These might be the error in position and velocity of a vehicle [6:294]. Navigation Kalman filters typically use an error state implementation due to the high dynamic rates possible in aviation systems. These high dynamic rates would require a very high sample rate for a direct state filter. However, the errors in this type of system grow slowly and this allows an error state implementation and a much lower sample rate [6:291-297].

The twelve states implemented in this research are as follows:

$$\delta \hat{\mathbf{x}} = \begin{bmatrix} \delta l \hat{\alpha}_n \\ \delta l \hat{\alpha}_t \\ \delta a \hat{l}_t \\ \delta v \hat{v}_n \\ \delta v \hat{v}_e \\ \delta v \hat{v}_d \\ \delta \hat{\alpha} \\ \delta \hat{\beta} \\ \delta \hat{\gamma} \\ \delta \hat{h}_{baro} \\ \delta \hat{c}b \\ \delta \hat{c}d \end{bmatrix} = \begin{bmatrix} \text{Longitude Position Error Estimate (radians)} \\ \text{Latitude Position Error Estimate (radians)} \\ \text{Altitude Position Error Estimate (meters)} \\ \text{North Velocity Error Estimate (m/sec)} \\ \text{East Velocity Error Estimate (m/sec)} \\ \text{Down Velocity Error Estimate (m/sec)} \\ \text{North Axis Tilt Error Estimate (radians)} \\ \text{East Axis Tilt Error Estimate (radians)} \\ \text{Down Axis Tilt Error Estimate (radians)} \\ \text{Time-correlated Barometric Error Estimate (meters)} \\ \text{GPS Clock Bias Error Estimate (meters)} \\ \text{GPS Clock Drift Error Estimate (m/sec)} \end{bmatrix} \quad (2.15)$$

An estimate of the total state  $\mathbf{x}_{true}$  can be found from the error states and INS data available in the filter by correcting the INS data (States 1 - 9) via Equation (2.16):

$$\hat{\mathbf{x}}_{true} = \mathbf{x}_{ins} + \delta \hat{\mathbf{x}} \quad (2.16)$$

where:

$\hat{\mathbf{x}}_{true}$  is the corrected state value

$\mathbf{x}_{ins}$  is the INS calculated state value

$\delta \hat{\mathbf{x}}$  is the filter calculated state error value

*2.2.5 State Covariance Matrix.* The (n x n) dimension covariance matrix ( $\mathbf{P}$ ) is an estimate generated by the filter that provides a measure of filter performance. It is a statistical measure of the uncertainty in each of the states [17:73].

*2.2.6 Dynamics Driving Noise Covariance Matrix.* ( $\mathbf{Q}_d$ ) is an (s x s) dimension dynamics driving noise covariance matrix.  $\mathbf{Q}_d$  is a measure of the strength of the dynamics driving noise [8:252].

*2.2.7 State Transition Matrix.* The state transition matrix ( $\Phi$ ) is an (n x n) dimension matrix.  $\Phi$  is used to propagate the states forward in time using knowledge about how the system functions over time without external aiding.

*2.2.8 Measurement Matrices.* There is a measurement vector and a measurement matrix generated in this filter. The first is the nonlinear measurement vector function ( $\mathbf{h}(\hat{\mathbf{x}})$ ), and the second is the ( $\mathbf{H}$ ) matrix, which is a linearized version of the first. The  $\mathbf{h}(\hat{\mathbf{x}})$  vector is used to generate the filter residuals [6:218]. The residuals are the difference between the measurements and the filter predictions of those measurements. The residuals provide information about the accuracy in the measurements.

*2.2.9 Measurement Noise.* The measurement noise covariance matrix ( $\mathbf{R}$ ) represents the uncertainty introduced in the measurement process due to imperfect sensors, noise, etc. The  $\mathbf{R}$  matrix has the same number of elements as there are measurements.

*2.2.10 Kalman Filter Cycle.* A Kalman filter can use two different techniques during a filter cycle—propagation and update. Propagation refers to using the system dynamic equations to move the states and covariance forward over time, and update refers to using measurements to increase the accuracy of those same states and covariance at a specific instant in time. A cycle does not require that an update occur. If no measurements are available, the states continue to propagate forward using the system dynamic equations. This is, in fact, commonly the case in a navigation filter. Vehicle PVA are computed many times per second, while updates are typically incorporated once or twice a second (and sometimes much less



Figure 2.1 Kalman Filter Cycle

frequently than that). If measurement incorporation once per minute produces acceptable navigation performance, then a much faster update rate may be abandoned to reduce unnecessary computational loading.

Figure 2.1 shows a typical Kalman filter cycle [6:207]. There are two different time epochs shown ( $t_{i-1}$  is an arbitrary epoch and  $t_i$  is one epoch later). The state is represented at different times by the filled-in circles. The superscript - and + represent the time just before, and just after, a measurement update, respectively. The circle at  $t_{i-1}^+$  represents the state just after an update is performed at time  $t_{i-1}$ . The state is then propagated via the system dynamic equations to time  $t_i$ , and is represented by  $t_i^-$  indicating the state immediately prior to update incorporation. As before, the state at  $t_i^+$  represents the state just after an update is performed at time  $t_i$ . This represents only one cycle; in reality this process is repeated many times, but the underlying concept remains unchanged.

### 2.3 Arc Length Equation

The arc length equation is used repeatedly during this research. This equation states that the length of an arc (on a circle) can be found by multiplying the radius by the angle (in radians). The radius used here is either the transverse radius of curvature ( $R_e$ ) or the meridian radius of curvature ( $R_n$ ) [16:305-306].

$$\text{arc length} = r\theta \quad (2.17)$$

where:

$r$  = radius

$\theta$  = angle (in radians)

*2.3.1 Meridian Radius of Curvature.* The meridian radius of curvature ( $R_n$ ) is used to determine the approximate radius of the Earth at the given latitude for a line of constant longitude [18:54]:

$$R_n = \frac{R(1 - e^2)}{[1 - e^2 \sin^2(L)]^{\frac{3}{2}}} \quad (2.18)$$

where:

$R$  = Earth's radius at the equator

$e$  = Earth's ellipticity

$L$  = Aircraft Latitude



2.3.2 *Transverse Radius of Curvature.* The transverse radius of curvature ( $R_e$ ) is used to determine an equivalent Earth radius at a given line of constant latitude [18:54]:

$$R_e = \frac{R \cos(L)}{[1 - e^2 \sin^2(L)]^{\frac{1}{2}}} \quad (2.19)$$

where:

R = Earth's radius at the equator

e = Earth's ellipticity

L = Aircraft Latitude

The distance generated by using  $R_e$  in conjunction with the arc length equation does not change when a change occurs in latitude. However, the conversion from distance to longitudinal angle (degrees or radians) does change when a change occurs in latitude. This is due to lines of longitude converging together as they move away from the equator. This explains the  $\cos(L)$  term in the numerator of Equation (2.19).

## 2.4 *Geometry*

Both tangent and inverse tangent functions are used repeatedly in this research. The partial derivative of the inverse tangent will also be required, and for this reason it will be reviewed below.

2.4.1 *Derivative of Inverse Tangent Function.* The partial derivative of an inverse tangent function is not a trivial calculation. However, it will be needed to generate the visual measurement **H** matrix, and therefore it will be demonstrated below. The lower case variables a, b, and c are all functions of at least one of the states. In this formulation, the variable c represents the measurement to be incorporated, the variable a represents distance, and the variable b represents another distance.

$$c = \tan^{-1} \left( \frac{a}{b} \right) \quad (2.20)$$

Taking the tangent of both sides of the equation eliminates the arctangent function and simplifies the right side of the equation.

$$\tan(c) = \tan \left[ \tan^{-1} \left( \frac{a}{b} \right) \right] = \left( \frac{a}{b} \right) \quad (2.21)$$

Then take the partial derivative of both sides of the equation with respect to the states ( $\mathbf{x}$ ).

$$\frac{\partial}{\partial x} \tan(c) = \frac{\partial}{\partial x} \left( \frac{a}{b} \right) \quad (2.22)$$

Expanding the left hand side of Equation (2.22) removes the tangent function from the partial derivative which simplifies the equation and sets the equation up for a substitution in the next step:

$$\frac{\partial}{\partial x} \tan(c) = \sec^2(c) \frac{\partial c}{\partial x} = (1 + \tan^2(c)) \frac{\partial c}{\partial x} = \frac{\partial}{\partial x} \left( \frac{a}{b} \right) \quad (2.23)$$

Recalling from Equation (2.21) that  $\tan(c) = \frac{a}{b}$ , this value is substituted into Equation (2.23), to simplify the left hand side by further removing the tangent function:

$$\left[ 1 + \left( \frac{a}{b} \right)^2 \right] \frac{\partial c}{\partial x} = \left[ 1 + \frac{a^2}{b^2} \right] \frac{\partial c}{\partial x} = \frac{\partial}{\partial x} \left( \frac{a}{b} \right) \quad (2.24)$$

Then, solve for the partial derivative of  $\frac{\partial c}{\partial x}$ :

$$\frac{\partial c}{\partial x} = \left[ \frac{b^2}{a^2 + b^2} \right] \frac{\partial}{\partial x} \left( \frac{a}{b} \right) \quad (2.25)$$

Finally, after expanding the partial derivative portion on the right of Equation (2.25) and cancelling the appropriate terms, the final form for  $\frac{\partial c}{\partial x}$  is obtained:

$$\frac{\partial c}{\partial x} = \left[ \frac{b^2}{a^2 + b^2} \right] \frac{\left( \frac{\partial a}{\partial x} \right) (b) - (a) \left( \frac{\partial b}{\partial x} \right)}{b^2} = \frac{\left( \frac{\partial a}{\partial x} \right) (b) - (a) \left( \frac{\partial b}{\partial x} \right)}{a^2 + b^2} \quad (2.26)$$

## 2.5 *Navigation Orbit Geometry Determination*

The navigation orbit was designed so that a particular target area would be within the camera FOV continuously for a ten minute period. A circular orbit was used in an effort to make this as easy as possible for the pilot.

*2.5.1 Assumptions.* There were several simplifying assumptions made:

1. No wind. This was so simple geometric equations could be used to determine an approximate airspeed and orbit size for the navigation orbit.
2. A side-mounted camera points out the right side of the aircraft. Assuming it points down the right wing line is an approximation since the camera-to-body frame rotation is not known. This approximation is accurate enough for flying the navigation orbit since the pilot will not be able to fly the exact profile.

The first assumption caused some difficulties while the second did not. The difficulties encountered will be addressed later in the “lessons learned” section in the appendices.

## 2.6 *Summary*

This chapter covered some basic theory that is needed in Chapter 3. Kalman filter basics were covered briefly, along with geometry relating to the arc length equation and other necessary geometric relationships. A description of the assumptions pertaining to the flight profile for the navigation orbit was also presented.

## 3. Methodology

### 3.1 Overview

The thrust of this research is the incorporation of a new type of visual measurement into a navigation Kalman filter. This measurement is formulated in two parts, each of which is an angle. The measurements as implemented in this research were simulated; however, a method for generating the measurements using a camera is presented at the end of this chapter. The chapter is broken up into five major parts: 3.2) Visual Measurements, 3.3) Visual Measurement Generation, 3.4) Visual Measurement Error Estimation, 3.5) Visual Measurement Generation using a Camera, and 3.6 Estimation of Attitude Error States. These last two sections extend the research to using an actual camera, even though one was not implemented in this thesis.

### 3.2 Visual Measurements

Each visual measurement is made up of two different parts — azimuth and elevation angles. These angles are measured from the aircraft to the target relative to the North - East - Down (NED) navigation frame. The angles used here are referenced from the Down vector and not out the nose of the aircraft (the way azimuth and elevation are typically referred to in an Air-to-Air radar). This means a point on the ground directly under the aircraft would be 0 degrees elevation and 0 degrees azimuth. Elevation and azimuth angles increase from 0 as the point of interest moves away from a point directly under the aircraft. The sense for these measurements is listed in Table 3.1.

The previously mentioned NED navigation frame is a local-level frame. As defined for the NED frame, elevation is along a line of constant longitude and azimuth is along a line of constant latitude. Aircraft altitude is known, and target altitude is assumed known. This assumption is considered reasonable in light of digital terrain

Table 3.1 NED Frame Elevation and Azimuth Sense

Target Direction from Aircraft in NED Frame	Elevation	Azimuth
North	+	n/a
South	-	n/a
East	n/a	+
West	n/a	-

elevation data (DTED) being readily available. This information is not incorporated into this research, but the data is available and could be included at a later date.

### 3.3 Visual Measurement Generation

The visual measurements are formed according to the geometry between the aircraft and the location of the selected target. The visual measurements were generated in the manner described below.

At visual measurement incorporation time, a vector was formed from the aircraft location to a known target location, expressed in the NED frame. This known target location was used with, and without, errors being injected in the target location (by adding errors into the stored angle values as they are used). Aircraft and target latitude, longitude and altitude were used to form this vector. No error is shown for  $tgt_{lat}$ ,  $tgt_{lon}$ , or  $tgt_{alt}$ . It is acknowledged that there would be errors in these values, but this added complexity is not dealt with in this formulation. See Chapter 5 for recommendations extending the research in this area.

The difference between the target latitude and the latitude of the aircraft (in radians) is calculated by:

$$\Delta lat = tgt_{lat} - acft_{lat} - \delta \hat{lat} \tag{3.1}$$

where:

$\Delta lat$  is the difference between aircraft and target latitude (radians)

$tgt_{lat}$  is the target latitude (radians)

$acft_{lat}$  is the aircraft INS-reported latitude (radians)

$\delta\hat{lat}$  is the filter-estimated aircraft latitude error (radians)

$(acft_{lat} + \delta\hat{lat})$  is the best estimate of the true latitude of the aircraft

Next, the distance correlating to the  $\Delta lat$  from the previous step is calculated using the arc length equation, with a radius defined by Equation (2.18). This will then be the distance from the aircraft to the target projected along a line of constant longitude. This projected distance is the North component of a vector from the aircraft to the target in the NED frame.

$$el_{dist} = R_n \Delta lat = R_n (tgt_{lat} - acft_{lat} - \delta\hat{lat}) \quad (3.2)$$

The difference between the target longitude and the longitude of the aircraft (in radians) is calculated by:

$$\Delta lon = tgt_{lon} - acft_{lon} - \delta\hat{lon} \quad (3.3)$$

where:

$\Delta lon$  is the difference between aircraft and target longitude (radians)

$tgt_{lon}$  is the target longitude (radians)

$acft_{lon}$  is the aircraft INS-reported longitude (radians)

$\delta\hat{lon}$  is the filter-estimated aircraft longitude error (radians)

$(acft_{lon} + \delta\hat{lon})$  is the best estimate of the true longitude of the aircraft

Finally, the distance correlating to the  $\Delta lon$  from the previous step is determined using the arc length equation. This is the distance from the aircraft to the target projected along a line of constant latitude. This projected distance is the East

component of a vector from the aircraft to the target in the NED frame.

$$az_{dist} = R_e \Delta lon = R_e (tgt_{lon} - acft_{lon} - \delta \hat{lon}) \quad (3.4)$$

The difference between the target altitude and the altitude of the aircraft is calculated slightly differently in keeping with the sign convention listed in Table 3.1 for the North and East directions in the NED frame. North is positive, East is positive, so according to the right-hand rule, Down is positive. This calculation is given by:

$$alt_{dist} = acft_{alt} + \delta \hat{alt} - tgt_{alt} \quad (3.5)$$

where:

$alt_{dist}$  is the difference between aircraft and target altitude (meters)

$acft_{alt}$  is the aircraft INS-reported altitude (meters)

$\delta \hat{alt}$  is the filter-estimated aircraft altitude error (meters)

$tgt_{alt}$  is the target altitude (meters)

$(acft_{alt} + \delta \hat{alt})$  is the best estimate of the true altitude of the aircraft

The aircraft-to-target vector in the NED frame is formed by the North, East, and Down components generated in the previous three steps.

$$\mathbf{n}^n = \begin{bmatrix} el_{dist} \\ az_{dist} \\ alt_{dist} \end{bmatrix} = \begin{bmatrix} R_n \Delta lat \\ R_e \Delta lon \\ alt_{dist} \end{bmatrix} = \begin{bmatrix} R_n (tgt_{lat} - acft_{lat} - \delta \hat{lat}) \\ R_e (tgt_{lon} - acft_{lon} - \delta \hat{lon}) \\ acft_{alt} + \delta \hat{alt} - tgt_{alt} \end{bmatrix} \quad (3.6)$$

Finally, the NED frame vector is used to determine the elevation and azimuth angles from the aircraft to the target via Equations (3.7) and Equations (3.8):

$$Elevation = \tan^{-1} \left( \frac{el_{dist}}{alt_{dist}} \right) \quad (3.7)$$

$$Azimuth = \tan^{-1} \left( \frac{az_{dist}}{alt_{dist}} \right) \quad (3.8)$$

### 3.4 Visual Measurement Error Estimation

During filter operation, simulated measurements and filter predictions of those same measurements are differenced and used as measurements in the filter. The filter predicts the measurements by taking the equations used to generate the estimated measurements to form the  $\mathbf{h}(\hat{\mathbf{x}}^-)$  vector. The nonlinear  $\mathbf{h}(\cdot)$  vector is then used to generate the linearized  $\mathbf{H}(\hat{\mathbf{x}}^-)$  matrix. This is done by taking the partial derivative of  $\mathbf{h}(\cdot)$  with respect to each state in the filter.

*3.4.1 Generating the  $\mathbf{H}(\hat{\mathbf{x}}^-)$  Matrix.* The first row of the  $\mathbf{H}(\hat{\mathbf{x}}^-)$  matrix corresponds with the azimuth measurements, while the second row corresponds with the elevation measurements. The fully populated  $\mathbf{H}(\hat{\mathbf{x}}^-)$  will look like Figure 3.9.

$$\mathbf{H}(\hat{\mathbf{x}}^-) = \begin{bmatrix} \text{az row} \\ \text{el row} \end{bmatrix} = \begin{bmatrix} \frac{\partial az}{\partial \delta lon} & 0 & \frac{\partial az}{\partial \delta alt} & 0 & 0 & 0 & 0 & 0 & 0 & 0 & 0 & 0 \\ 0 & \frac{\partial el}{\partial \delta lat} & \frac{\partial el}{\partial \delta alt} & 0 & 0 & 0 & 0 & 0 & 0 & 0 & 0 & 0 \end{bmatrix} \quad (3.9)$$

Generation of the first element of the azimuth row is shown below in Section 3.4.1.1. Equation (2.25) is repeated here, as it is needed to generate each of the 12 components of the  $\mathbf{H}(\hat{\mathbf{x}}^-)$  matrix first row:

$$\frac{\partial \tan^{-1} \left( \frac{a}{b} \right)}{\partial x} = \frac{\left( \frac{\partial a}{\partial x} \right) (b) - (a) \left( \frac{\partial b}{\partial x} \right)}{a^2 + b^2} \quad (3.10)$$



3.4.1.1 *Azimuth Row Generation.* The right side of Equation (3.11) must be calculated with respect to each of the twelve states in the Kalman filter state matrix. The end result for azimuth will populate row 1 of Equation (3.9). The elements that are zero are due to the partial derivatives all being zero. This is due to the right side of Equation (3.11) not being a function of any of those states.

First, the  $\frac{\partial \tan^{-1} \left( \frac{az_{dist}}{alt_{dist}} \right)}{\partial \delta \hat{lon}}$  component of the  $\mathbf{H}(\hat{\mathbf{x}}^-)$  matrix will be calculated (element for row 1, column 1). The generic equation is given by Equation (3.11):

$$\frac{\partial \tan^{-1} \left( \frac{az_{dist}}{alt_{dist}} \right)}{\partial state_i} = \frac{\left( \frac{\partial az_{dist}}{\partial state_i} \right) (alt_{dist}) - (az_{dist}) \left( \frac{\partial alt_{dist}}{\partial state_i} \right)}{az_{dist}^2 + alt_{dist}^2} \quad (3.11)$$

The generic equation becomes more specific when the partial derivative is taken with respect to a particular state:

$$\frac{\partial \tan^{-1} \left( \frac{az_{dist}}{alt_{dist}} \right)}{\partial \delta \hat{lon}} = \frac{\left( \frac{\partial az_{dist}}{\partial \delta \hat{lon}} \right) (alt_{dist}) - (az_{dist}) \left( \frac{\partial alt_{dist}}{\partial \delta \hat{lon}} \right)}{az_{dist}^2 + alt_{dist}^2} \quad (3.12)$$

The equation is then best broken into two parts. The partial derivative on the left side of the numerator is shown here:

$$\left( \frac{\partial az_{dist}}{\partial \delta \hat{lon}} \right) = \frac{\partial}{\partial \delta \hat{lon}} [R_e (tgt_{lon} - acft_{lon} - \delta \hat{lon})] = -R_e \quad (3.13)$$

while the partial derivative on the right side of the numerator is:

$$\left( \frac{\partial alt_{dist}}{\partial \delta \hat{lon}} \right) = \frac{\partial}{\partial \delta \hat{lon}} (acft_{alt} + \delta \hat{alt} - tgt_{alt}) = 0 \quad (3.14)$$

The results of the two partial derivative calculations are then substituted back into Equation 3.12, which can now be solved in this more simplistic form:

$$\frac{\partial \tan^{-1} \left( \frac{az_{dist}}{alt_{dist}} \right)}{\partial \delta \hat{l}_{on}} = \frac{(-R_e)(acft_{alt} + \delta \hat{alt} - tgt_{alt}) - (R_e[tgt_{lon} - acft_{lon} - \delta \hat{l}_{on}])(0)}{(R_e[tgt_{lon} - acft_{lon} - \delta \hat{l}_{on}])^2 + (acft_{alt} + \delta \hat{alt} - tgt_{alt})^2} \quad (3.15)$$

which reduces to:

$$\frac{\partial \tan^{-1} \left( \frac{az_{dist}}{alt_{dist}} \right)}{\partial \delta \hat{l}_{on}} = \frac{-R_e(acft_{alt} + \delta \hat{alt} - tgt_{alt})}{(R_e[tgt_{lon} - acft_{lon} - \delta \hat{l}_{on}])^2 + (acft_{alt} + \delta \hat{alt} - tgt_{alt})^2} \quad (3.16)$$

The remaining three elements from Equation 3.9 are calculated in a like manner, and the results are shown below. Intermediate calculations are omitted, because they are similar to the  $\frac{\partial}{\partial \delta \hat{l}_{on}} \tan^{-1} \left( \frac{az_{dist}}{alt_{dist}} \right)$  example given above.

$$\frac{\partial \tan^{-1} \left( \frac{az_{dist}}{alt_{dist}} \right)}{\partial \delta \hat{alt}} = \frac{-R_e(tgt_{lon} - acft_{lon} - \delta \hat{l}_{on})}{(R_e[tgt_{lon} - acft_{lon} - \delta \hat{l}_{on}])^2 + (acft_{alt} + \delta \hat{alt} - tgt_{alt})^2} \quad (3.17)$$

$$\frac{\partial \tan^{-1} \left( \frac{el_{dist}}{alt_{dist}} \right)}{\partial \delta \hat{l}_{at}} = \frac{-R_n(acft_{alt} + \delta \hat{alt} - tgt_{alt})}{(R_n[tgt_{lat} - acft_{lat} - \delta \hat{l}_{at}])^2 + (acft_{alt} + \delta \hat{alt} - tgt_{alt})^2} \quad (3.18)$$

$$\frac{\partial \tan^{-1} \left( \frac{el_{dist}}{alt_{dist}} \right)}{\partial \delta \hat{alt}} = \frac{-R_n(tgt_{lat} - acft_{lat} - \delta \hat{l}_{at})}{(R_n[tgt_{lat} - acft_{lat} - \delta \hat{l}_{at}])^2 + (acft_{alt} + \delta \hat{alt} - tgt_{alt})^2} \quad (3.19)$$

### 3.5 Visual Measurement Generation using a Camera

Section 3.5 is not actually implemented in this thesis. It is presented here to support follow-on work.

*3.5.1 Required Camera Specifications.* Certain camera specifications are required to relate camera frame geometry to navigation frame geometry. Camera focal length ( $f$ ) must be known, and one of the following must be known to determine the width and height of the viewed image. This information is used to determine the vertical and horizontal pixel size.

1. Vertical and horizontal field-of-view ( $fov_v^c$  and  $fov_h^c$  respectively), where the  $v$  and  $h$  subscripts are for vertical and horizontal, respectively. The superscript  $c$  indicates the variable is in the camera frame.
2. If the fields-of-view are not known, vertical and horizontal coverage ( $cov_v^c$  and  $cov_h^c$  respectively) can be used to generate these angles by:

$$fov_v^c = 2tan^{-1} \left( \frac{cov_v^c}{2f} \right) \quad (3.20)$$

$$fov_h^c = 2tan^{-1} \left( \frac{cov_h^c}{2f} \right) \quad (3.21)$$

Then, the vertical and horizontal pixel size can be calculated by:

$$pixel_v = \frac{cov_v^c}{\text{ver pixel count}} \quad (3.22)$$

$$pixel_h = \frac{cov_h^c}{\text{hor pixel count}} \quad (3.23)$$

*3.5.2 Generate Target Latitude/Longitude.* The camera geometry is used to translate target pixel location into a geometrical reference. This can then be rotated into the body frame and ultimately into the NED navigation frame.

Targets in an image are selected, and this selection generates pixel locations for each target. These pixel locations are referenced from the center of the image.

This vector is shown in Equation (3.24).

$$\mathbf{n} = \begin{bmatrix} n_x \\ n_y \end{bmatrix} = \begin{bmatrix} \text{vertical component of target in pixels} \\ \text{horizontal component of target in pixels} \end{bmatrix} \quad (3.24)$$

The camera frame sense is similar to that previously described in the navigation frame. This camera sense is shown below in Table 3.2 and is echoed in Figure 3.1.

Table 3.2 Camera Frame Elevation and Azimuth Sense

Target Direction from Center of Camera Frame	Elevation	Azimuth
Up	+	n/a
Down	-	n/a
Right	n/a	+
Left	n/a	-

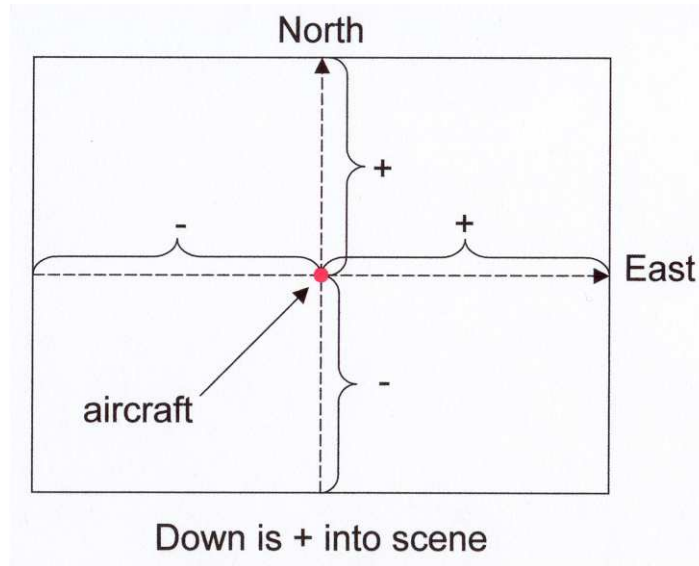


Figure 3.1 Sign Convention

Vector  $\mathbf{n}$  is generated in a fashion similar to that show in Figure 3.2, and can then be formed into a 3D vector in the camera frame by multiplying by the proper pixel size to get a distance in the camera frame. Knowledge of the camera focal length

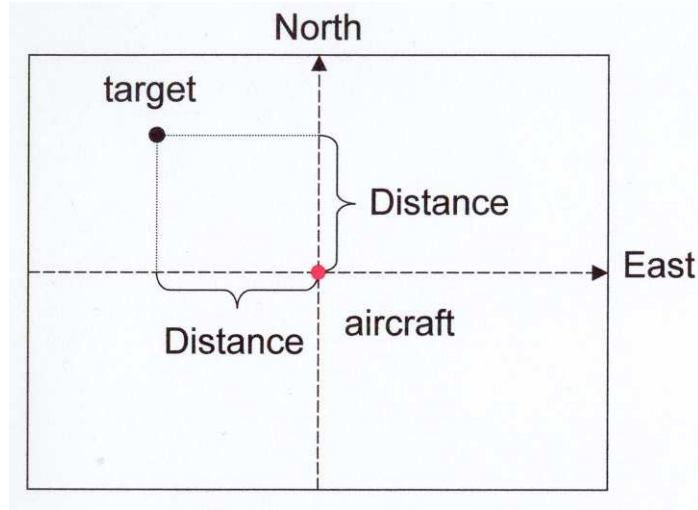


Figure 3.2 Distances

provides the third dimension. Equation (3.5.2) now forms a vector to the target(s) in the camera frame. This is captured by the following equation:

$$\mathbf{n}^c = \begin{bmatrix} (pixel_v)(n_x) \\ (pixel_h)(n_y) \\ f \end{bmatrix} = \begin{bmatrix} n_x^c \\ n_y^c \\ f \end{bmatrix} \quad (3.25)$$

Camera errors due to deficiencies in the optics must now be removed so the above vector points to the actual target location as opposed to the skewed location shown on the photo. The camera errors generated during the camera calibration procedure discussed in Section 3.5.7 are stored in an angular format, so vector  $\mathbf{n}^c$  is used to generate the uncorrected azimuth ( $az_{uncorr}$ ) (Equation (3.26)) and the uncorrected elevation ( $el_{uncorr}$ ) (Equation (3.27)). Figure 3.3 graphically demonstrates these angles. They are the azimuth and elevation angles with optical errors still present.

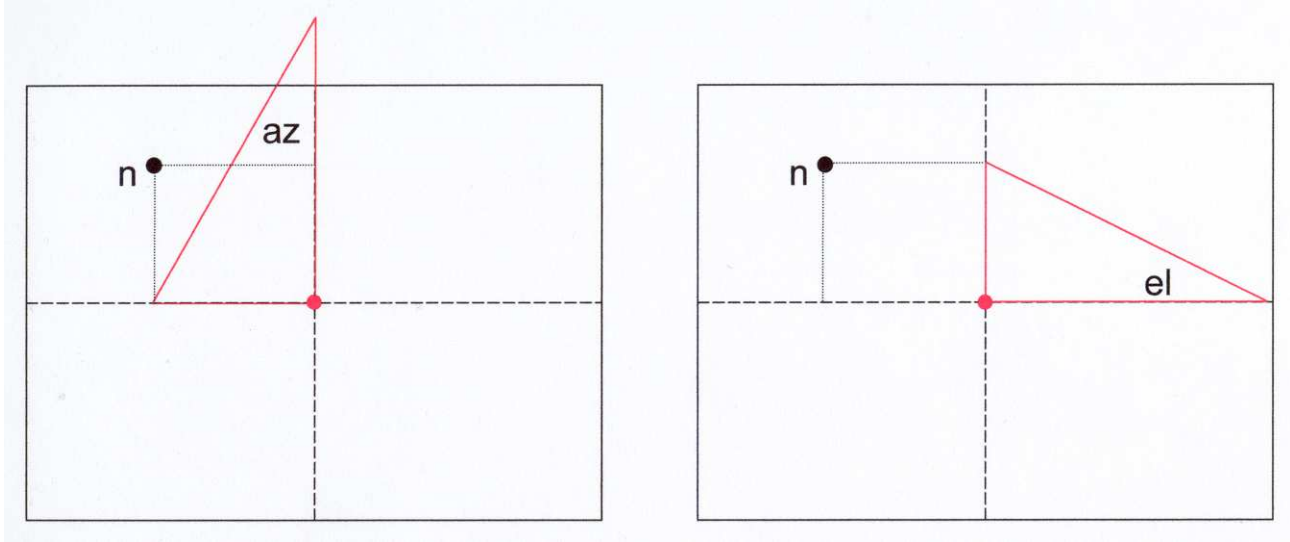


Figure 3.3 Angles

$$az_{uncorr}^c = \tan^{-1} \left( \frac{n_y^c}{f} \right) \quad (3.26)$$

$$el_{uncorr}^c = \tan^{-1} \left( \frac{n_x^c}{f} \right) \quad (3.27)$$

These angles will become azimuth in the camera frame ( $az^c$ ) and elevation in the camera frame ( $el^c$ ) once the errors are removed via Equations (3.28) and (3.29). The values for the optical azimuth error ( $optical_{azerror}$ ) and the optical elevation error ( $optical_{elerror}$ ) are pre-computed during the camera alignment procedure (see Section 3.5.7).

$$az^c = az_{uncorr}^c - optical_{azerror} \quad (3.28)$$

$$el^c = el_{uncorr}^c - optical_{elerror} \quad (3.29)$$

The corrected  $az^c$  and  $el^c$  must be converted back to a vector so target information can be rotated from the camera frame, through the body frame (via Equation (3.31)),

to the navigation frame (via Equation (3.32)).

$$\mathbf{n}^c = \begin{bmatrix} (f)(\tan(el^c)) \\ (f)(\tan(az^c)) \\ f \end{bmatrix} = \begin{bmatrix} n_x^c \\ n_y^c \\ f \end{bmatrix} \text{ (Vector in Camera Frame)} \quad (3.30)$$

This is accomplished by pre-multiplying the camera frame vector by the camera-to-body direction cosine matrix (DCM) ( $C_c^b$ ) in Equation (3.31):

$$\mathbf{n}^b = \mathbf{C}_c^b \mathbf{n}^c \text{ (Vector in Body Frame)} \quad (3.31)$$

Then the body frame vector is pre-multiplied by the body-to-navigation frame DCM ( $C_b^n$ ) to transform the vector into the navigation frame:

$$\mathbf{n}^n = \mathbf{C}_b^n \mathbf{n}^b \text{ (Vector in Nav Frame)} \quad (3.32)$$

The  $az^n$  (Equation (3.33)) and  $el^n$  (Equation (3.34)) angles can then be determined from the components of vector  $\mathbf{n}^n$ . These angles are NED frame angles:

$$az^n = \tan^{-1} \left( \frac{n_y^n}{n_z^n} \right) \quad (3.33)$$

$$el^n = \tan^{-1} \left( \frac{n_x^n}{n_z^n} \right) \quad (3.34)$$

The next step is to determine target longitude and latitude. Longitude will be calculated by first determining Earth radius ( $R_e$ ) along a line of constant latitude at the current aircraft latitude. Then  $az^n$  is used to determine distance along a line of constant latitude ( $az_{dist}$ ) from aircraft longitude to target longitude:

$$az_{dist} = (alt_{dist})\tan(az^n) \quad (3.35)$$

Then the arc length equation is used to determine the radian change in longitude from the aircraft to the target:

$$\Delta lon = \frac{az_{dist}}{R_e} \quad (3.36)$$

Target longitude can then be calculated by the relationship:

$$tgt_{lon} = \Delta lon + acft_{lon} + \delta \hat{lon} \quad (3.37)$$

A similar procedure is used to determine target latitude by first determining Earth radius ( $R_n$ ) along a line of constant longitude at the current aircraft latitude. This is analogous with  $R_e$  above, except the change in latitude is along a line of constant longitude which is an ellipse rather than a circle. Use  $el^n$  to determine distance along a line of constant longitude ( $el_{dist}$ ) from aircraft latitude to target latitude:

$$el_{dist} = (alt_{dist}) \tan(el^n) \quad (3.38)$$

$el_{dist}$  is then combined with the arc length equation to determine the radian change in latitude from the aircraft to the target:

$$\Delta lat = \frac{el_{dist}}{R_n} \quad (3.39)$$

Target latitude can then be determined by the relationship:

$$tgt_{lat} = \Delta lat + acft_{lat} + \delta \hat{lat} \quad (3.40)$$

*3.5.3 Generate Measurements from an Image.* The procedure for generating measurements from an image is exactly the same as in Section 3.5.2, steps 3.5.2 through 3.5.2. The remaining steps in Section 3.5.2 need not be accomplished to



generate measurements because target latitude/longitude is estimated the first time the target was incorporated.

*3.5.4 Generate Measurement Estimates.* The procedure for estimating measurements is very similar to that of Section 3.5.2, except the procedure is performed backwards. First,  $\hat{az}_n$  is determined from the estimate of target longitude by re-arranging Equation (3.37) to get the change in longitude from the current INS longitude to the target longitude:

$$\Delta\hat{lon} = tgt_{lon} - acft_{lon} - \delta\hat{lon} \quad (3.41)$$

Then Equation (3.36) is re-arranged to get the estimated  $\hat{az}_{dist}$ :

$$\hat{az}_{dist} = R_e\Delta lon \quad (3.42)$$

Similarly,  $\hat{el}_n$  can be determined from the estimate of target latitude by re-arranging Equation (3.40) to get the change in latitude from the current INS latitude to the target latitude:

$$\Delta\hat{lat} = tgt_{lat} - acft_{lat} - \delta\hat{lat} \quad (3.43)$$

Then Equation (3.39) is manipulated to get the estimated  $\hat{el}_{dist}$ :

$$\hat{el}_{dist} = R_n\Delta lat \quad (3.44)$$

The previously determined  $\hat{az}_{dist}$  and  $\hat{el}_{dist}$  can be combined with altitude data to form the vector to the target in the navigation frame:

$$\hat{\mathbf{n}}^n = \begin{bmatrix} R_n\Delta lat \\ R_e\Delta lon \\ altitude \end{bmatrix} = \begin{bmatrix} n_x^n \\ n_y^n \\ n_z^n \end{bmatrix} = \begin{bmatrix} \hat{el}_{dist} \\ \hat{az}_{dist} \\ \hat{alt}_{dist} \end{bmatrix} \quad (3.45)$$

The  $\mathbf{C}_n^b$  DCM is used to rotate the navigation frame vector to the body frame:

$$\hat{\mathbf{n}}^b = \mathbf{C}_n^b \hat{\mathbf{n}}^n \quad (3.46)$$

Then the  $\mathbf{C}_b^c$  DCM is used to rotate the body frame vector to the camera frame:

$$\hat{\mathbf{n}}^c = \mathbf{C}_b^c \hat{\mathbf{n}}^b \quad (3.47)$$

Determine estimates of  $\hat{az}^c$  and  $\hat{el}^c$  in camera frame from the components of the camera frame vector  $\mathbf{n}^c$ :

$$\hat{az}^c = \tan^{-1} \left( \frac{\hat{n}_y^c}{\hat{n}_z^c} \right) \quad (3.48)$$

$$\hat{el}^c = \tan^{-1} \left( \frac{\hat{n}_x^c}{\hat{n}_z^c} \right) \quad (3.49)$$

*3.5.5 Camera-to-Body DCM Generation .* The camera-to-body DCM ( $\mathbf{C}_c^b$ ) is generated by tracking targets with surveyed coordinates. A vector to the target is generated in the camera frame and a vector to the target is generated in the nav frame. The nav frame vector is rotated into the body frame. The two vectors are now related through  $\mathbf{C}_c^b$ .

*3.5.6 Visual Measurement  $\mathbf{R}$  Matrix Generation.* Generating the uncertainty in a measurement is somewhat arbitrary. It should be based on sound reasoning even though the final value that works best in the actual filter may be quite different. This value is typically found by “tuning” the Kalman filter. This is a process in which different uncertainties in the filter are adjusted to generate the best possible filter performance. In a perfect world the measurements would have zero error. However, this is not the case so errors that exist must be approximated. This is so the uncertainty in the measurements can be used to weight the measurements

properly. The following phenomena cause errors in the visual measurements and will be addressed individually: faulty pixel selection and optical deficiencies.

Faulty pixel selection is due to the inability to select the exact same point on a target each time that target is used to generate a measurement. An error of several pixels is realistic in such a procedure. This error will inject itself directly into the measurements as an angle error. The vector generated in Section 3.5.2, Equation (3.24) will contain this error and inject it directly into Equations (3.51) and (3.52).

$$\mathbf{n}^c = \begin{bmatrix} (pixel_v)(n_x + \delta n_x) \\ (pixel_h)(n_y + \delta n_y) \\ f \end{bmatrix} = \begin{bmatrix} n_x^c + \delta n_x^c \\ n_y^c + \delta n_y^c \\ f \end{bmatrix} \quad (3.50)$$

$$az_{uncorr}^c = az_{uncorr_{true}}^c + \delta az_{uncorr}^c = \tan^{-1} \left( \frac{n_{y_{true}}^c + \delta n_y^c}{f} \right) \quad (3.51)$$

$$el_{uncorr}^c = el_{uncorr_{true}}^c + \delta el_{uncorr}^c = \tan^{-1} \left( \frac{n_{x_{true}}^c + \delta n_x^c}{f} \right) \quad (3.52)$$

The worst case angle error for faulty pixel selection occurs when the selected pixel location is supposed to be in the exact center of the image but is off by some error amount. A typical case is demonstrated below using camera specs for the camera in use during algorithm development at AFIT (not used during flight test). The uncorrected true azimuth ( $az_{uncorr_{true}}^c$ ) and uncorrected true elevation ( $el_{uncorr_{true}}^c$ ) are each zero since they are supposed to be in the image center. Two pixels of error is assumed as a nominal case and 0.0074mm and 0.0073mm are the pixel sizes for azimuth and elevation pixels, respectively:

$$\delta az_{uncorr}^c = (az_{uncorrtrue}^c + \delta az_{uncorr}^c) - az_{uncorrtrue}^c = \quad (3.53)$$

$$= \tan^{-1} \left( \frac{n_{ytrue}^c + \delta n_y^c}{f} \right) - \tan^{-1} \left( \frac{n_{ytrue}^c}{f} \right) \quad (3.54)$$

$$= \tan^{-1} \left( \frac{(0.0074 * 0) + (0.0074 * 2)}{5.2} \right) - \tan^{-1} \left( \frac{0.0074 * 0}{5.2} \right) = \quad (3.55)$$

$$= 0.0028 - 0 = \quad (3.56)$$

$$= 0.0028 \text{ radian error} \quad (3.57)$$

$$\delta el_{uncorr}^c = (el_{uncorrtrue}^c + \delta el_{uncorr}^c) - el_{uncorrtrue}^c = \quad (3.58)$$

$$= \tan^{-1} \left( \frac{n_{xtrue}^c + \delta n_x^c}{f} \right) - \tan^{-1} \left( \frac{n_{xtrue}^c}{f} \right) = \quad (3.59)$$

$$= \tan^{-1} \left( \frac{(0.0073 * 0) + (0.0073 * 2)}{5.2} \right) - \tan^{-1} \left( \frac{0.0073 * 0}{5.2} \right) = \quad (3.60)$$

$$= 0.0028 - 0 = \quad (3.61)$$

$$= 0.0028 \text{ radian error} \quad (3.62)$$

The errors incurred above inject directly into the next type of error, which are optical deficiencies. Optical deficiencies are due to abnormalities in the camera lens, imperfections in camera component alignment, software resident in the camera as well as other physical camera phenomenon. A calibration procedure is performed in Section 3.5.7, but this cannot remove all the errors present. This is especially true when the angles generated in the previous section have errors due to improper pixel selection.

$$az^c = az_{true}^c + \delta az^c = \quad (3.63)$$

$$= az_{uncorr_{true}}^c + \delta az_{uncorr}^c + OptErr_x \quad (3.64)$$

where  $OptErr_x$  is generated from the optical error surface determined from the camera calibration procedure (i.e.,  $OptErr_0 = -0.00135$  and  $OptErr_2 = -0.00154$ ). This optical error must be estimated since it cannot be solved for deterministically.

$$\delta az^c = (az_{true}^c + \delta az^c) - az_{true}^c = \quad (3.65)$$

$$= az_{uncorr_{true}}^c + \delta az_{uncorr}^c - az_{uncorr_{true}}^c + OptErr_0 - OptErr_2 = \quad (3.66)$$

$$= \tan^{-1} \left( \frac{n_{y_{true}}^c + \delta n_y^c}{f} \right) - \left( \tan^{-1} \left( \frac{n_{y_{true}}^c}{f} \right) \right) + OptErr_0 - OptErr_2 = \quad (3.67)$$

$$= \tan^{-1} \left( \frac{(0.0074 * 0) + (0.0074 * 2)}{5.2} \right) - \tan^{-1} \left( \frac{0.0074 * 0}{5.2} \right) - 0.00135 + 0.00154 = \quad (3.68)$$

$$= 0.0028 - 0 - 0.0013 + 0.0015 = \quad (3.69)$$

$$= 0.003 \quad (3.70)$$

The same effect occurs for errors in the elevation measurements. These values are for only one point and would need to be analyzed for the entire error surface to generate a more accurate characterization of the errors. This analysis could be used to generate an appropriate order of magnitude for the  $1-\sigma$  values for these errors. This  $1-\sigma$  value could then be used as a first cut at an  $\mathbf{R}$  value for the filter.

*3.5.7 Camera Calibration Procedures.* The camera must be calibrated before it is used for a mission. Errors are resident that must be removed. This cannot be done deterministically, so a procedure is used to estimate the errors. The

camera is set up a known distance from a calibration target (similar to that shown in Figure 3.4). The camera must be carefully aligned so its focal plane is parallel to the target or errors will be injected into the final result since this will skew the geometry between the camera and the target. A mis-alignment of this sort essentially changes the physical geometry of the setup. Since this error is not detected it will pollute the error surface being generated. Then a picture is taken of the calibration target. This picture is used to generate the azimuth and elevation angles to each element in the calibration photo. These angles are then compared with the known angles that are generated from the known physical geometry between the camera and the calibration target. The  $az_{error}$  and  $el_{error}$  are defined in Equations (3.71) and (3.72) respectively:

$$az_{error} = az_{true} - az_{meas} \quad (3.71)$$

$$el_{error} = el_{true} - el_{meas} \quad (3.72)$$

These azimuth and elevation errors generate an error surface for the entire camera field-of-view. The azimuth error surface generated at AFIT during development is shown below in Figure 3.5. This figure describes the error in azimuth as a function of horizontal and vertical position in the image. The surface appears as a planar image due to the sign convention described previously. The elevation error surface is similar in appearance.

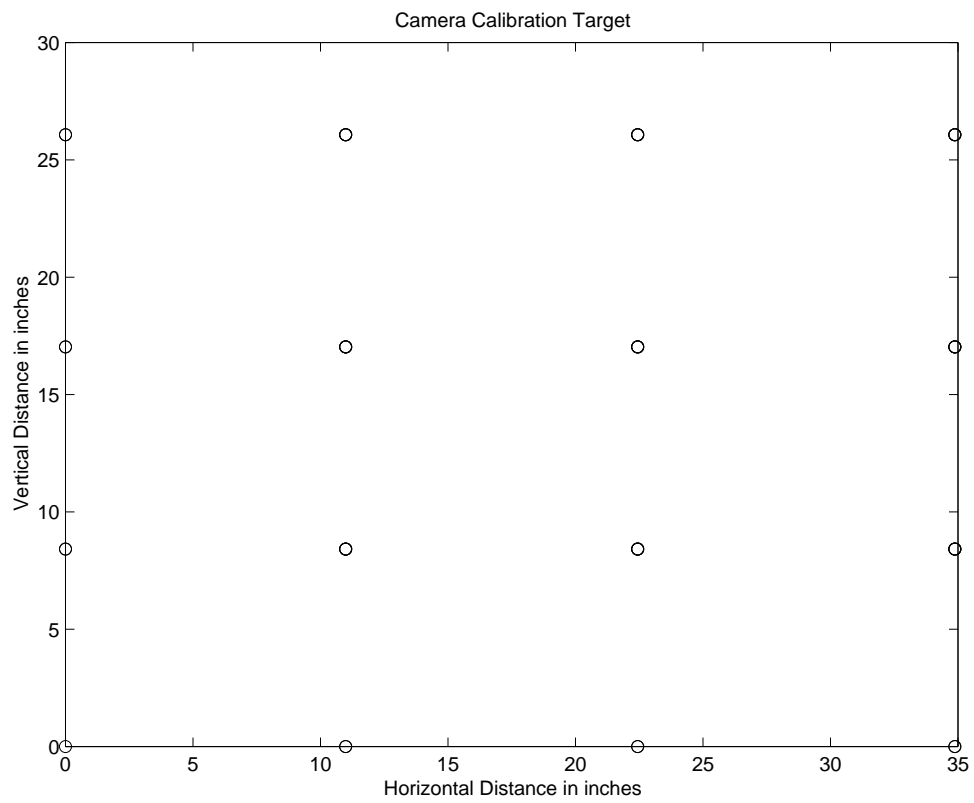


Figure 3.4 Camera Calibration Target

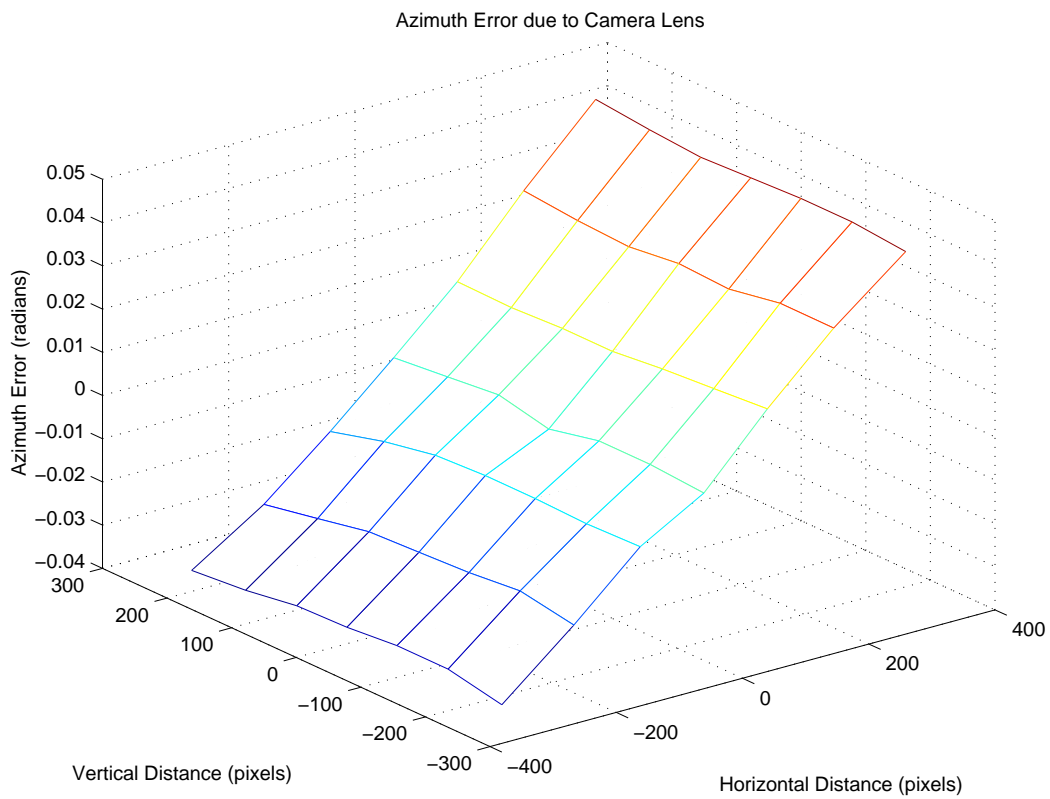


Figure 3.5 Azimuth Error Surface



### 3.6 Estimation of Attitude Error States

The method for estimating the attitude error states presented below is not actually implemented in this thesis. It is presented here to support follow-on work.

This section is similar to Section 3.4, in that the  $\mathbf{H}(\hat{\mathbf{x}}^-)$  matrix must be derived and calculated. However, the attitude error terms must also be populated in this matrix, in addition to the four terms already described.

Recall that the camera frame vector  $\mathbf{n}^c$  must be rotated through two frames to generate  $\mathbf{n}^n$ :

$$\mathbf{n}^c = \mathbf{C}_b^n \mathbf{C}_c^b \mathbf{n}^c \quad (3.73)$$

The camera-to-body frame DCM ( $\mathbf{C}_c^b$ ) is a fixed DCM in this research. However, the body-to-navigation frame DCM ( $\mathbf{C}_b^n$ ) changes every epoch and contains errors associated with three of the states. Those states are North axis tilt error ( $\delta\alpha$ ), East axis tilt error ( $\delta\beta$ ), and Down axis tilt error ( $\delta\gamma$ ). This means the partial derivative of the measurements with respect to the states will have more elements that are non-zero. Those elements are shown in Equation (3.74) with the first three columns being the same as presented previously. The incorporation of a camera into this research will certainly cause filter performance to suffer somewhat. How much is to be determined. However, the errors should be small enough, at least initially, that visual measurements still generate better filter performance. The point where the tilt errors grow too large for visual measurements to be effective is also to be determined.

$$\mathbf{H}(\hat{\mathbf{x}}^-) = \begin{bmatrix} \text{az row} \\ \text{el row} \end{bmatrix} = \begin{bmatrix} \frac{\partial \text{az}}{\partial \delta \hat{\text{lon}}} & 0 & \frac{\partial \text{az}}{\partial \delta \text{alt}} & 0 & 0 & 0 & \frac{\partial \text{az}}{\partial \delta \alpha} & \frac{\partial \text{az}}{\partial \delta \beta} & \frac{\partial \text{az}}{\partial \delta \gamma} & 0 & 0 & 0 \\ 0 & \frac{\partial \text{el}}{\partial \delta \text{lat}} & \frac{\partial \text{el}}{\partial \delta \text{alt}} & 0 & 0 & 0 & \frac{\partial \text{el}}{\partial \delta \alpha} & \frac{\partial \text{el}}{\partial \delta \beta} & \frac{\partial \text{el}}{\partial \delta \gamma} & 0 & 0 & 0 \end{bmatrix} \quad (3.74)$$

The actual formulation of this new  $\mathbf{H}(\hat{\mathbf{x}}^-)$  is not derived here, but it should be similar in derivation to that from Section 3.4.

### *3.7 Summary*

This chapter defined the visual measurements to be incorporated into the Kalman filter and demonstrated the formulation of these angles. The method of generating visual measurement errors was covered in detail, as well as the theory for incorporating visual measurements from an actual camera. The effects of the simulated measurements as implemented in this thesis are analyzed in the next chapter.

## 4. Results and Analysis

### 4.1 Sortie Overview

Simulated visual measurements were generated during Kalman filter operation. Elevation and azimuth angles were generated at a 2 Hz rate during the 6-minute 27-second navigation portion from time 244995 to time 245382 (GPS week seconds). This was accomplished by running the GPS filter (see Table 4.1 for an explanation of the different filter types) and generating azimuth and elevation angles at each image incorporation time. This data was then stored in a data file for incorporation into the Kalman filter for analysis.

The sortie chosen for analysis in this research was a daylight flight from Edwards AFB to the Channel Islands (off the coast of Los Angeles) and back. A navigation orbit was performed right after takeoff, with the remainder of the flight dedicated to the camera evaluation. The ground track for the sortie is shown in Figure 4.1, with the altitude displayed in Figure 4.2. These figures are given to demonstrate the sortie profile visually. The filter data shown here incorporated GPS measurements only, and no baro or visual measurements were used. This data was saved and used as a truth source. There were other truth sources available (i.e., Ashtech-only, EGI-only, and a differential GPS solution). The Ashtech-only and EGI-only solutions were less smooth than the filter-generated truth solution. Their solutions showed position jumps on the order of several meters, and for this reason they were discarded as potential truth sources. The differential GPS solution generated by the airborne Ashtech receiver and the ground based Ashtech receiver had data dropouts that made this solution unsuitable. The filter-generated truth data is not ideal, but it is appropriate to demonstrate navigation accuracy increase or decrease as GPS measurements are removed, and baro and visual measurements take their place.

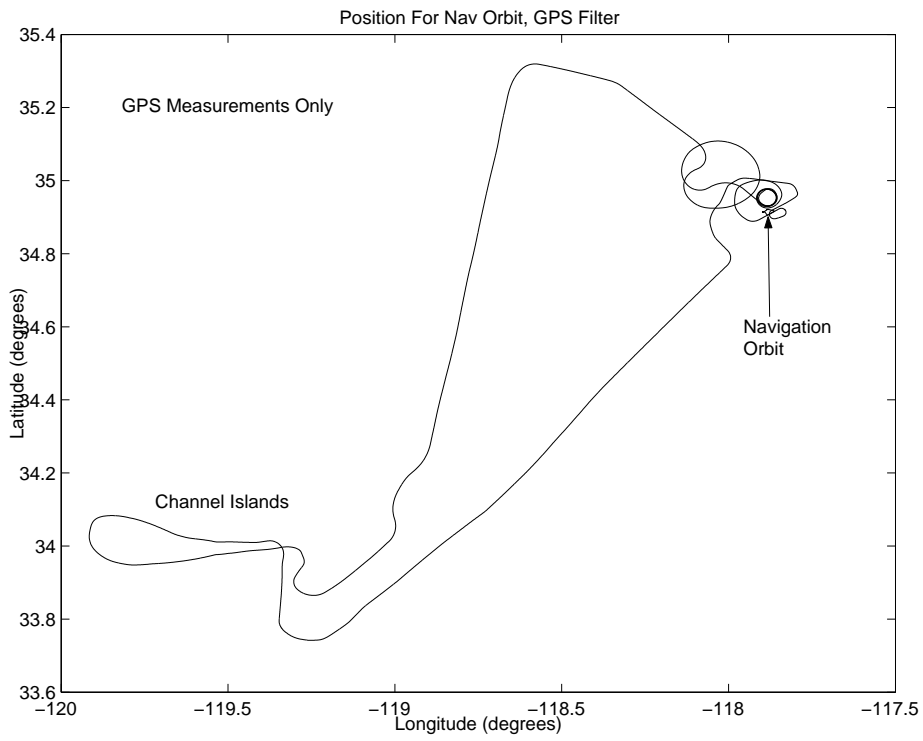


Figure 4.1 Ground Track

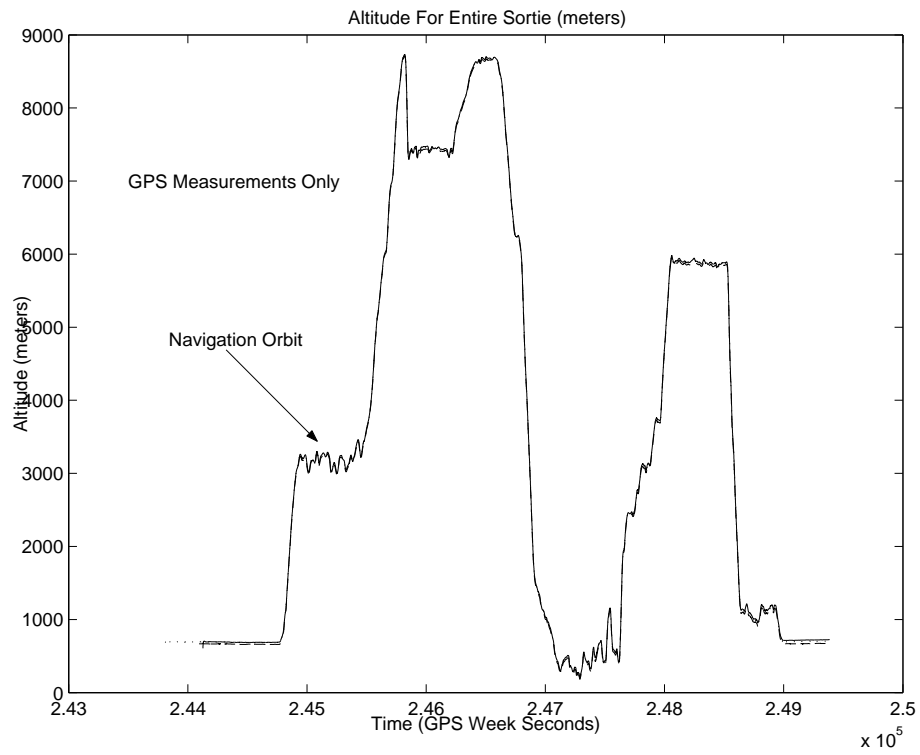


Figure 4.2 Altitude for Entire Sortie

Table 4.1 Filter Configurations

<b>Filter Name</b>	<b>Filter Description</b>
GPS Filter	GPS measurements incorporated before, during, and after the navigation orbit
Unaided Filter	No measurements incorporated during the navigation orbit
Baro Filter	Only Baro measurements incorporated during the navigation orbit
Baro/Vis Filter	Only Baro and Visual measurements incorporated during the navigation orbit
Vis Filter	Only Visual measurements incorporated during the navigation orbit

Unfortunately, generating simulated visual measurements using the GPS filter resulted in minor errors in the “truth” position due to time tagging errors (the GPS measurements were not synchronous with the simulated visual measurements). This produced an error of less than one meter from the “truth” position used to generate visual measurements. This is acceptable since the best performing filter under analysis has an approximate average error of 10 meters (under optimum conditions). There are five different filter configurations that will be discussed. Each filter has GPS measurements incorporated before and after the navigation orbit. They differ only in the type, or lack of, measurements that are incorporated during the navigation orbit. They are listed in Table 4.1, along with how they will be referenced from this point forward in this thesis.

Figure 4.1 shows the start of navigation in the upper right corner along with the navigation orbit. The Channel Island overflight is in the lower left corner. Figure 4.2 shows the altitude for the entire sortie (in meters). The first level-off at approximately 3200 meters is the navigation orbit. The figure clearly shows some altitude deviations during the orbit. This was due to difficulties in flying a constant orbit. These altitude variations will be investigated in greater detail later in this section.

Figure 4.3 highlights the navigation orbit area. This orbit was flown at approximately 3,300 meters above the ground and at an airspeed of 154 meters/second

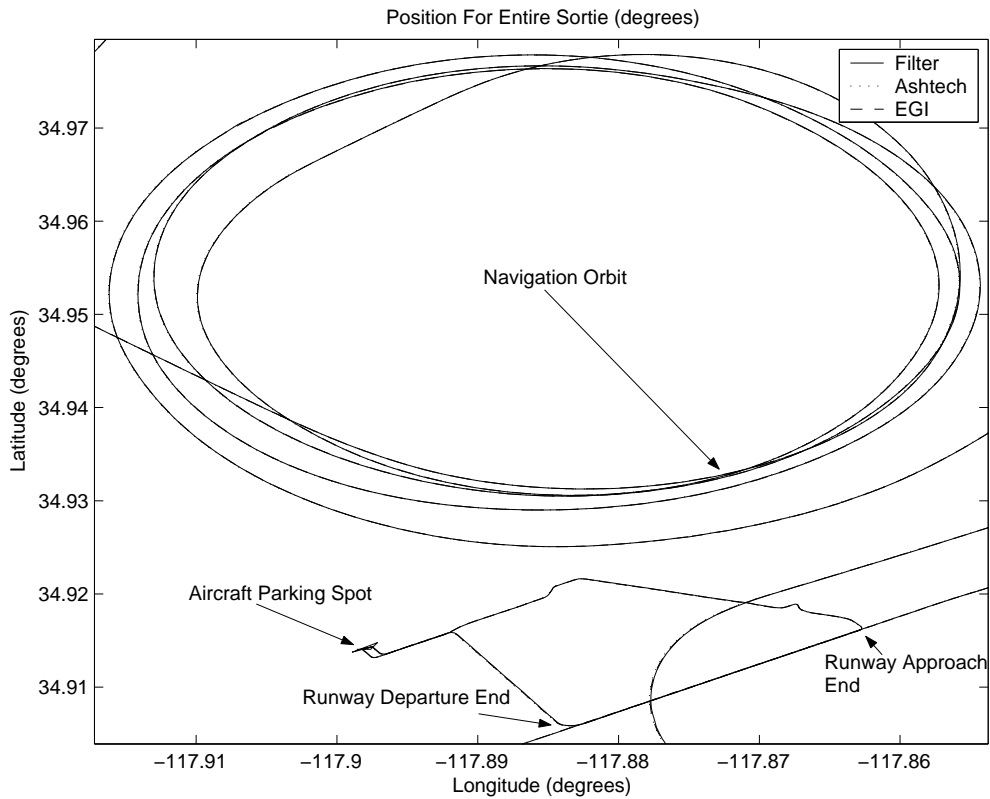


Figure 4.3 Ramp Area and Navigation Orbit

(300 knots indicated airspeed). This resulted in the navigation orbit diameter being roughly 5,721 meters (3.1 nautical miles). Figure 4.3 also shows the parking area for the test aircraft, the ground taxi, both the takeoff and landing, as well as the navigation orbit. The analysis will concentrate on the navigation orbit. Different combinations of measurements will be incorporated during this orbit and compared with each other to determine which filter operates the best.

The orbit is shown in Figure 4.4. The data was generated using the GPS filter during the entire orbit. This is the truth data, against which the Unaided filter, the Baro filter, and the Baro/Vis filter navigation orbits will be compared.

It is clear that the GPS filter performs much better than the Unaided filter from a comparison of Figures 4.4 and 4.5, respectively. It is also clear that some sort

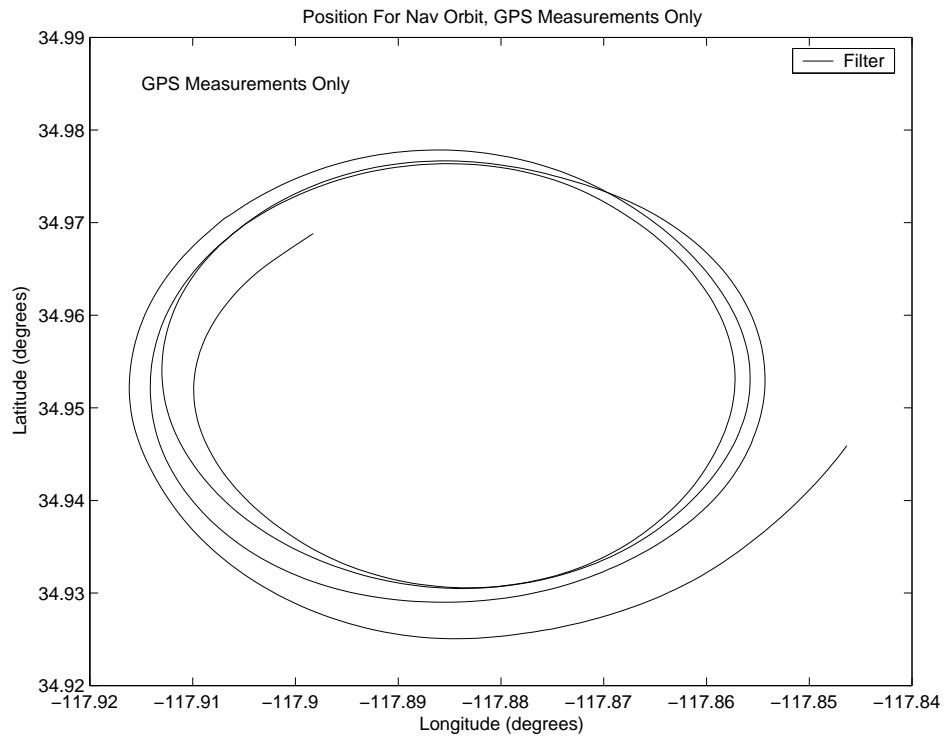


Figure 4.4 GPS Filter Navigation Orbit

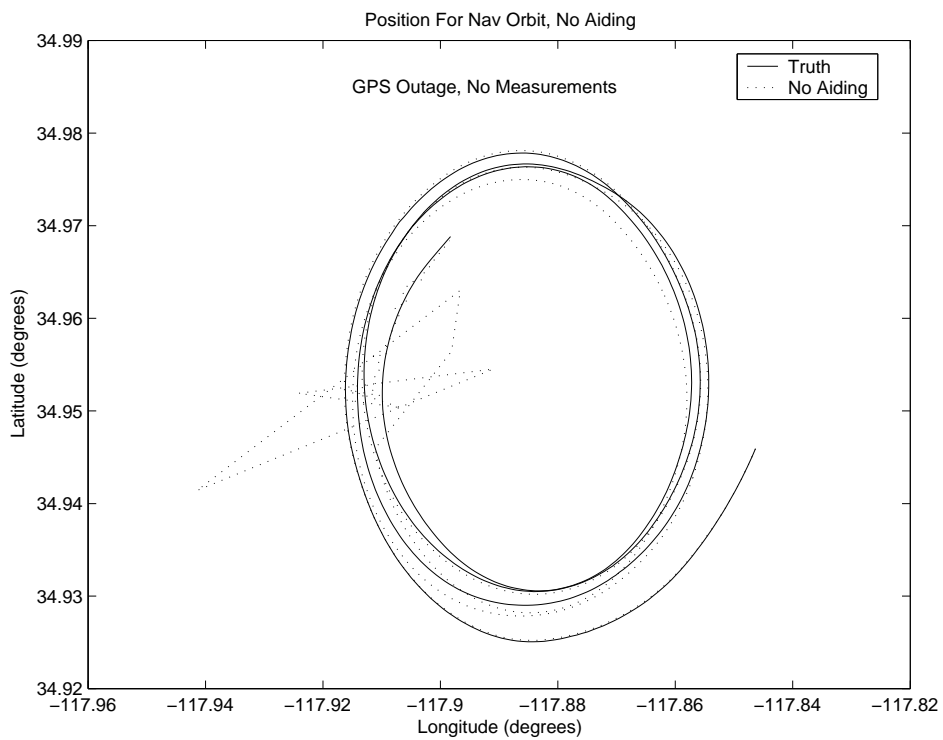


Figure 4.5 Navigation Orbit for Unaided Filter

of aiding is required during the navigation orbit GPS outage to improve navigational accuracy. The end portion of the Unaided filter orbit, when GPS measurements are re-incorporated, is cause for concern. With GPS measurements again available, the Unaided filter operates more poorly than the Baro or Baro/Vis filter (not shown). The larger the disparity between the filter estimates and the incorporated measurements, the larger the filter gyrations until everything smoothes out. The Unaided filter shows a much larger lateral fluctuation than the Baro or Baro/Vis filters. The reason for this is unclear when only looking at Figure 4.5, this is cause for further investigation.

#### *4.2 General Filter Comments*

The Kalman filter used in this research is a twelve-state filter. There are some minor problems with the implementation that cause the filter to require aiding. These problems appear to reside in the vertical channel. Problems in the vertical channel are normal in inertial navigation systems, but this filter implementation appears to be worse than normal. These difficulties were allowed to remain, as the filter would be continuously aided in some fashion, and the navigation accuracy increase or decrease can still be determined when incorporating visual measurements. These problems are shown in Figure 4.5 where there was no aiding during the navigation orbit. The Unaided lateral position solution clearly diverges from the true position.

GPS measurements are re-incorporated at the end of the  $6\frac{1}{2}$ -minute navigation orbit. The large lateral fluctuations that are visible at the end of the navigation orbit are due to the large discrepancy between the GPS measurements and the filter estimates of position.

#### *4.3 Unaided and Baro Filter Cases*

The results of the filters without visual aiding (Unaided and Baro) will be shown for comparison purposes with the Baro/Vis and Vis filters. The three dimen-



sional (3D) error for each of these two filters is shown in Figures 4.6. The Unaided filter is clearly prone to very large errors. However, this is mostly due to vertical errors and not horizontal errors. The Unaided filter has the same approximate lateral error as the Baro filter (350m). The Baro filter 3D error is much smaller, but still significant at about 350m for the lateral direction (approximately 4m vertical error). It appears that the Baro filter performs better than the Unaided filter in the lateral because of the large disparity in the vertical error between the two filters (note the different scales).

#### 4.4 Different Cases

Several different cases were investigated to determine the effect that various visual measurements error levels had on navigation accuracy. Measurement errors were modelled as white Gaussian noise with a standard deviation of  $\sigma_{meas}$ . A name is given to each  $\sigma_{meas}$  value incorporated into the filter and listed along with that  $\sigma$  value Table 4.2 below:

Table 4.2 Measurement Cases

Case	Case Description
Case 1	“Perfect” Visual Measurements $\sigma_{meas} = 5 \times 10^{-13}$ (radians)
Case 2	Nominal Visual Measurements $\sigma_{meas} = 0.005$ (radians)
Case 3	Marginal Visual Measurements $\sigma_{meas} = 0.05$ (radians)
Case 4	Bad Visual Measurements $\sigma_{meas} = 0.5$ (radians)

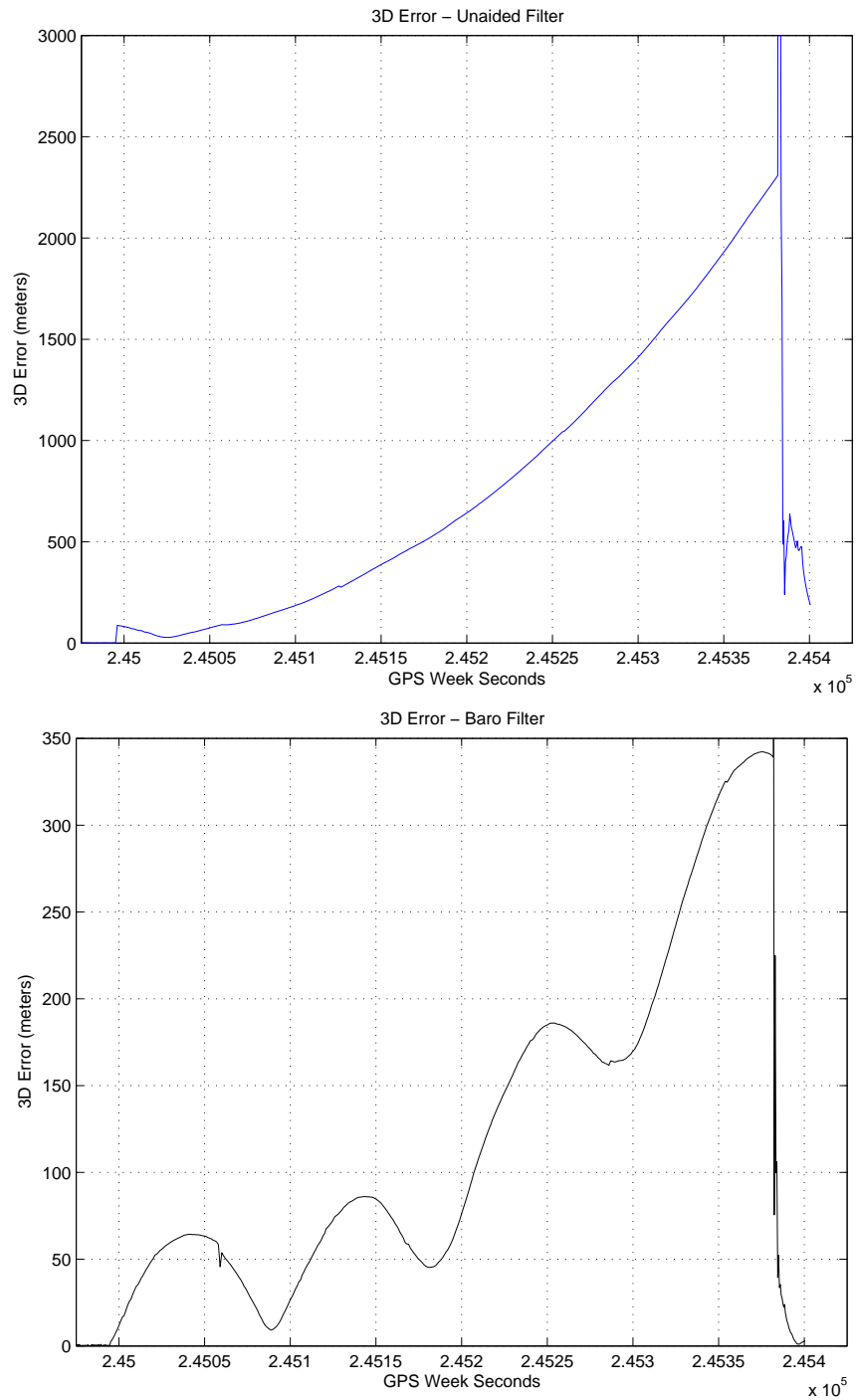


Figure 4.6 3D Position Error for Unaided Filter (top) and Baro Filter (bottom)

#### 4.5 Perfect Measurement Case

The perfect measurement case uses a standard deviation for the measurement noise uncertainty of  $\sigma = 5 \times 10^{-13}$  (radians). This small number means that the errors are essentially zero. This test is done to demonstrate the best theoretically possible level of performance that can be obtained using visual measurements. Figures 4.7 and 4.8 show the 3D error for the Baro/Vis and Vis filters for Case 1. This figure uses the same scale as the Baro filter in Figure 4.6 to demonstrate how much better these two filters perform than the non-visual-measurement-aided filters.

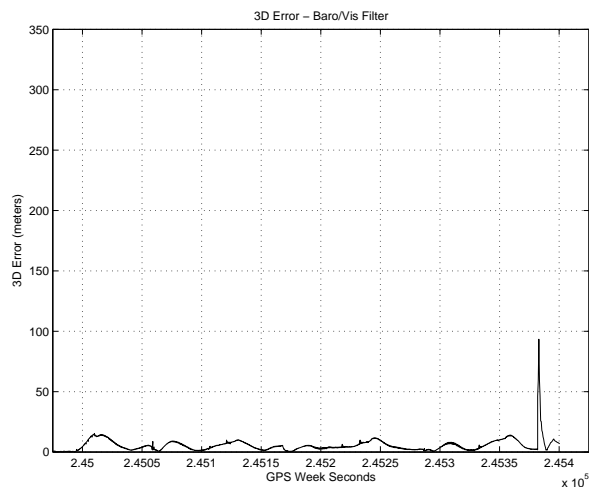


Figure 4.7 Case 1 — 3D Position Error for Baro/Vis Filter

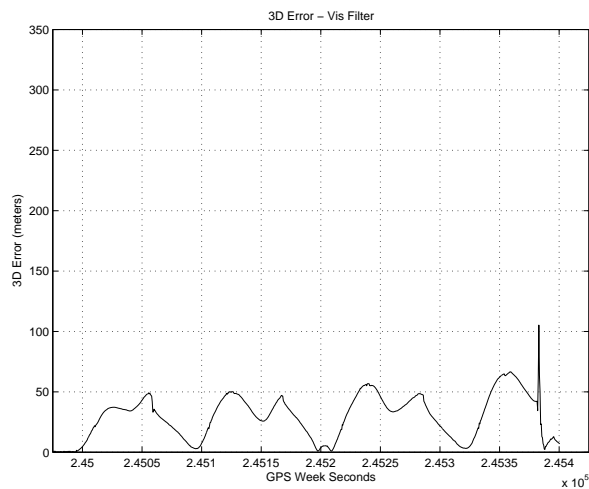


Figure 4.8 Case 1 — 3D Position Error for Vis Filter

#### 4.6 Nominal Case

A measurement error standard deviation of  $\sigma = 0.005$  radians is chosen as the nominal case, using the reasoning described in Section 3.5.6. The calculated errors in Section 3.5.6 were for a single point, so the  $\sigma_{meas}$  used here is roughly 50% higher to be conservative. While not exact, the nominal  $\sigma_{meas}$  value is close to what would generally be expected from an actual camera. Figures 4.9, 4.10 and 4.11 compare the Baro, Baro/Vis, and Vis filters for Case 2. Visual measurements clearly improve navigation accuracy when nominal measurement accuracy is used. A more in-depth analysis of the nominal case follows.

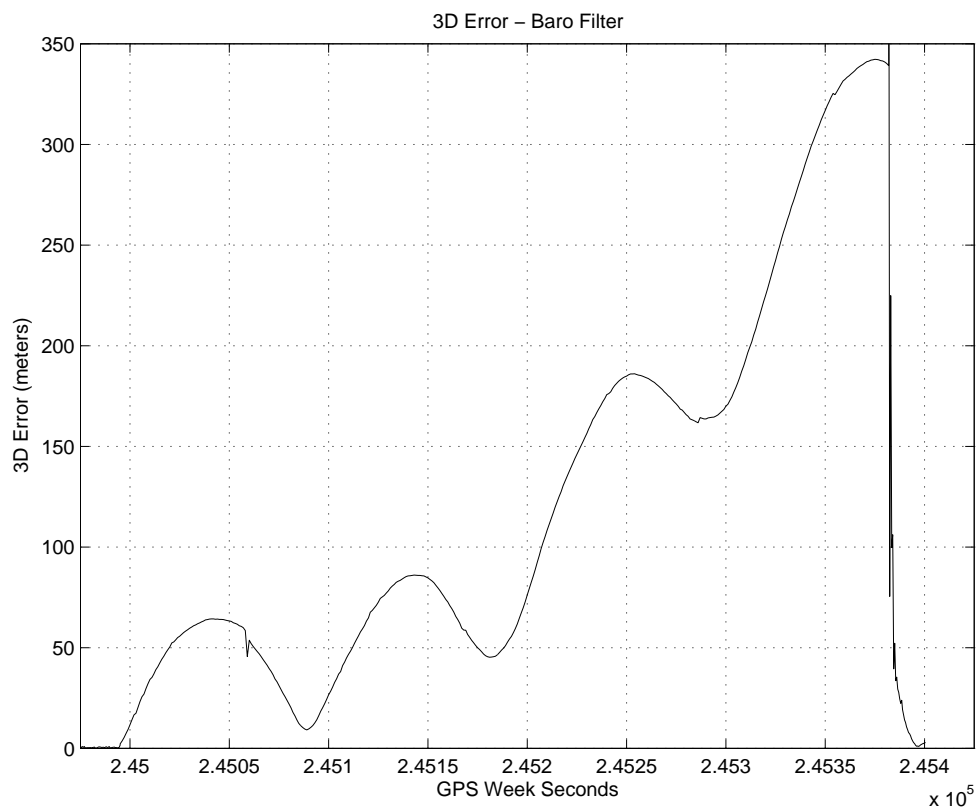


Figure 4.9 Case 2 — 3D Position Error for Baro Filter

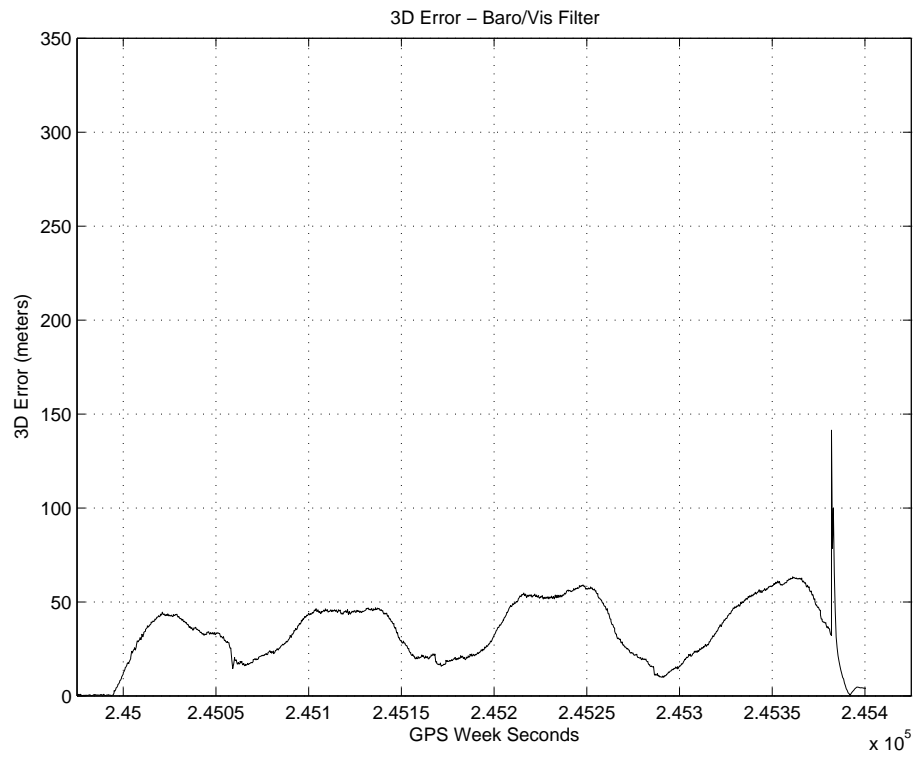


Figure 4.10 Case 2 — 3D Position Error for Baro/Vis Filter

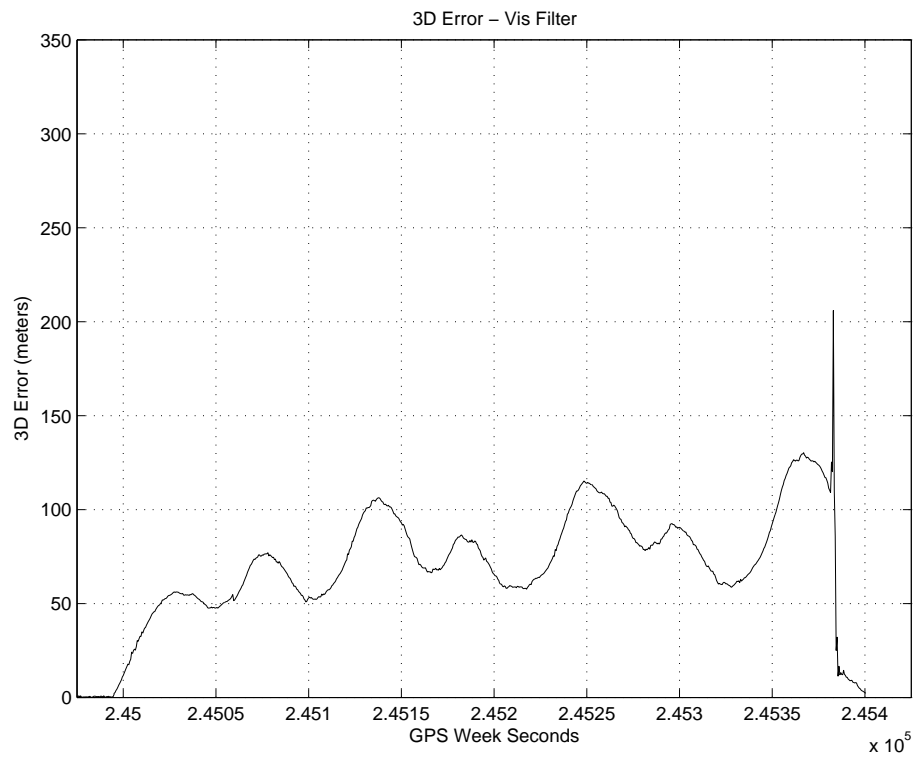


Figure 4.11 Case 2 — 3D Position Error for Vis Filter

#### 4.7 Individual Axis Position Comparison

Evaluating position errors in each axis is another way of comparing filter performance. In this section, filter comparisons will typically be placed in a figure composed of three parts, with the Unaided filter on the top, the Baro filter in the middle, and the Baro/Vis filter at the bottom. The appropriate covariances will be plotted on each figure as dashed lines. This is demonstrated in Figure 4.12. The Baro/Vis filter used for the position and velocity comparisons used a nominal measurement uncertainty value.

Useful information can be gleaned by comparing each of the filters to the truth data. Figure 4.12 does this for the North position error between the three filters and the truth data. The North error for each filter is plotted using the same scale, and again there is no clear difference between the Unaided and Baro filter, while the Baro/Vis filter performs substantially better. The Unaided filter actually peaks at a slightly lower error value than the Baro filter. The Unaided and Baro filter North errors appear to be growing larger. This divergent behavior was expected for the Unaided and Baro filters. The Baro/Vis filter shows no divergence, is bounded about zero, and four times better than the Unaided or Baro filter by the end of the time frame in question.

The East position error comparison in Figure 4.13 shows similar performance to the North position error comparison. Both the Unaided and the Baro filters appear to diverge to the same approximate value. The Baro/Vis filter shows about an 80 percent reduction in East error by the end of the navigation orbit time frame, is bounded about zero, and does not appear divergent.

The Down error of Figure 4.14 shows much more information pertinent to the lateral error in the Unaided filter performance in Figure 4.5. The Unaided filter performance is so much worse than the Baro or the Baro/Vis filters, that different scales were required on the Unaided filter plot to capture all the relevant data. The Unaided filter diverges immediately away from zero and continues its divergence all

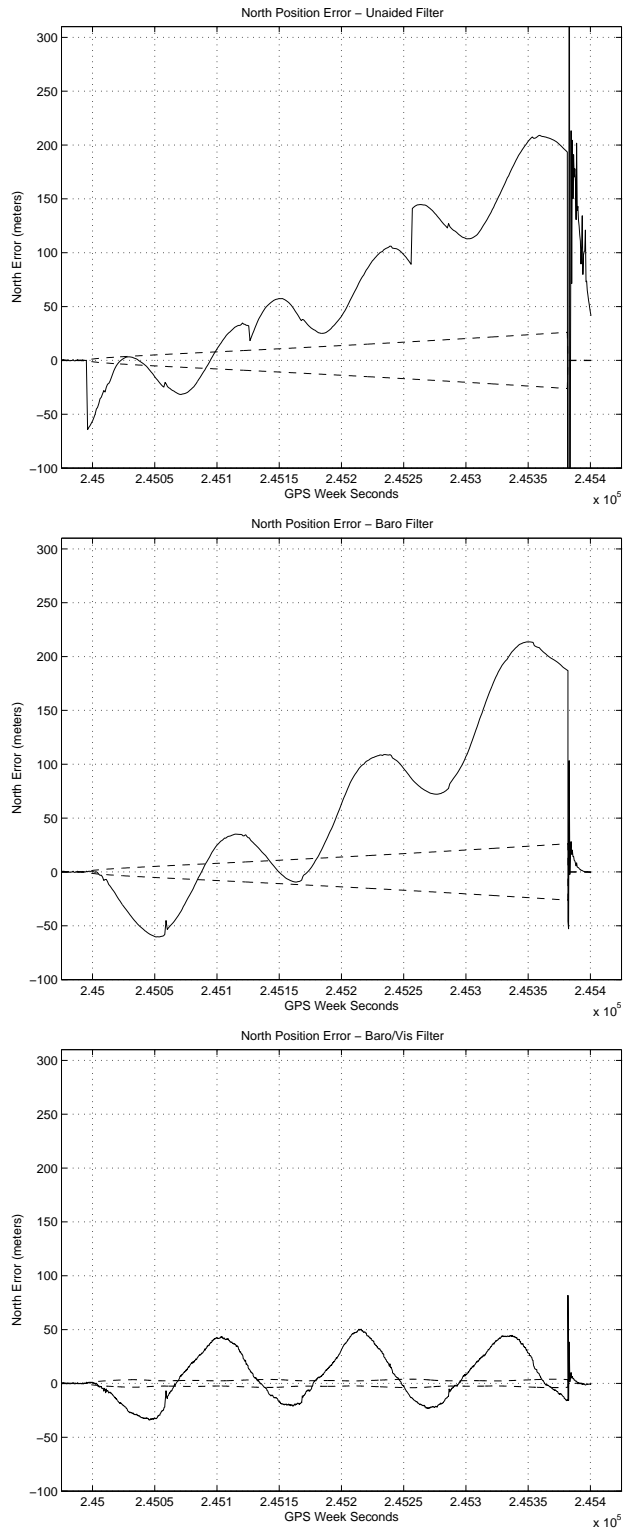


Figure 4.12 North Position Error for Unaided Filter (top), Baro Filter (middle), and Baro/Vis Filter (bottom). (Dashed Lines Indicate  $\pm 1\text{-}\sigma$  Filter-Compensated Covariance)

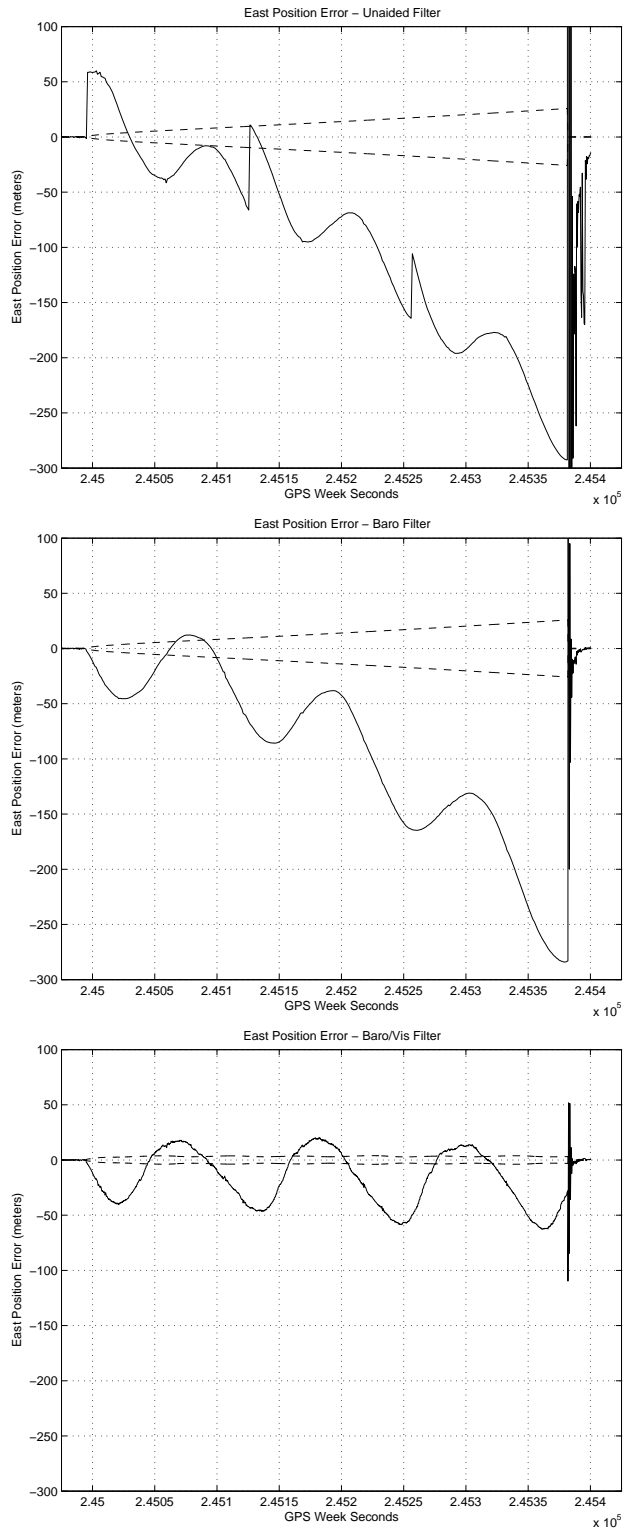


Figure 4.13 East Position Error for Unaided Filter (top), Baro Filter (middle), and Baro/Vis Filter (bottom). (Dashed Lines Indicate  $\pm 1\text{-}\sigma$  Filter-Compensated Covariance)



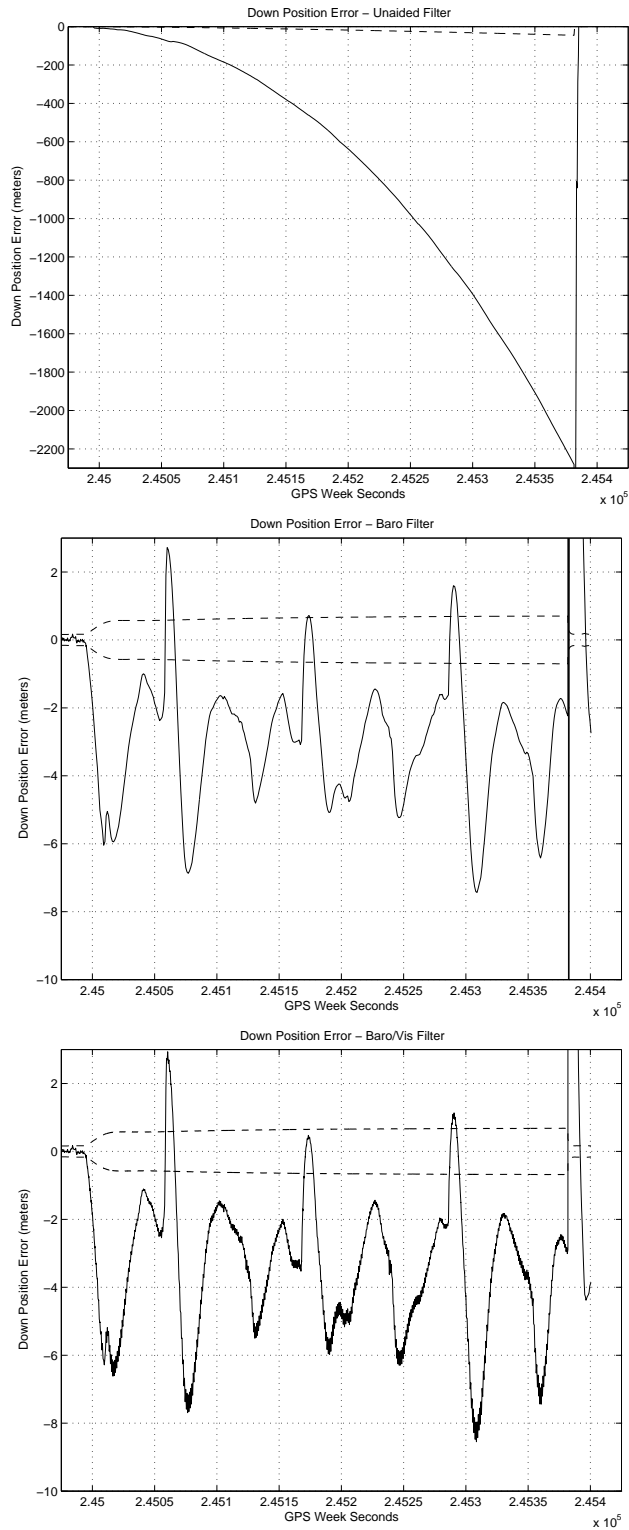


Figure 4.14 Down Position Error for Unaided Filter (top), Baro Filter (middle), and Baro/Vis Filter (bottom). (Dashed Lines Indicate  $\pm 1\text{-}\sigma$  Filter-Compensated Covariance)

the way to -2200 meters. This divergence would eventually lead the filter estimates to become worthless, if measurements were not re-incorporated. The disparity between the filter altitude estimate and the GPS measurement indication of altitude is very large at the end of the navigation orbit. The Baro and Baro/Vis filters perform much better and show no divergence. Their error is biased to about 3 meters, and there is no discernable difference between them.

All three of the channels errors are well outside the one- $\sigma$  bound predicted by the filter (and well outside the three- $\sigma$  bound also). This indicated that the filter has not yet been tuned to perform optimally. The Unaided and Baro filter covariance for the North and East channels (and the Unaided vertical channel) grow over the time frame of interest. This is due to the divergent nature of the errors. The Baro/Vis filter in all channels (and the Baro filter vertical channel) show covariances that are relatively constant over the navigation orbit time. This is due to the non-divergent nature of the errors in these channels.

#### *4.8 Position State Error Comparison*

The first three states in the filter correspond to position, with State 1 corresponding to east ( $\delta\hat{l}o\hat{n}$ ), State 2 to north ( $\delta\hat{l}a\hat{t}$ ), and State 3 to down ( $\delta\hat{a}l\hat{t}$ ). All plots in each figure use the same scale for ease of comparison and show the GPS “truth” filter as a dashed line. Each plot also has a circle placed at the point when the takeoff was begun. This was placed on each plot to discern between ground and airborne data. This was deemed to be of interest, because each of the filters shows some error during the ground portion of the sortie, especially since the aircraft was stationary for certain portions of this time.

The Baro/Vis filter performance is almost exactly the same as that of the GPS filter (see Figures 4.15 and 4.16). The filter performance when GPS signals are re-incorporated show the Unaided and Baro filters are further away from the real position than the Baro/Vis filter. This is demonstrated by the large position jumps

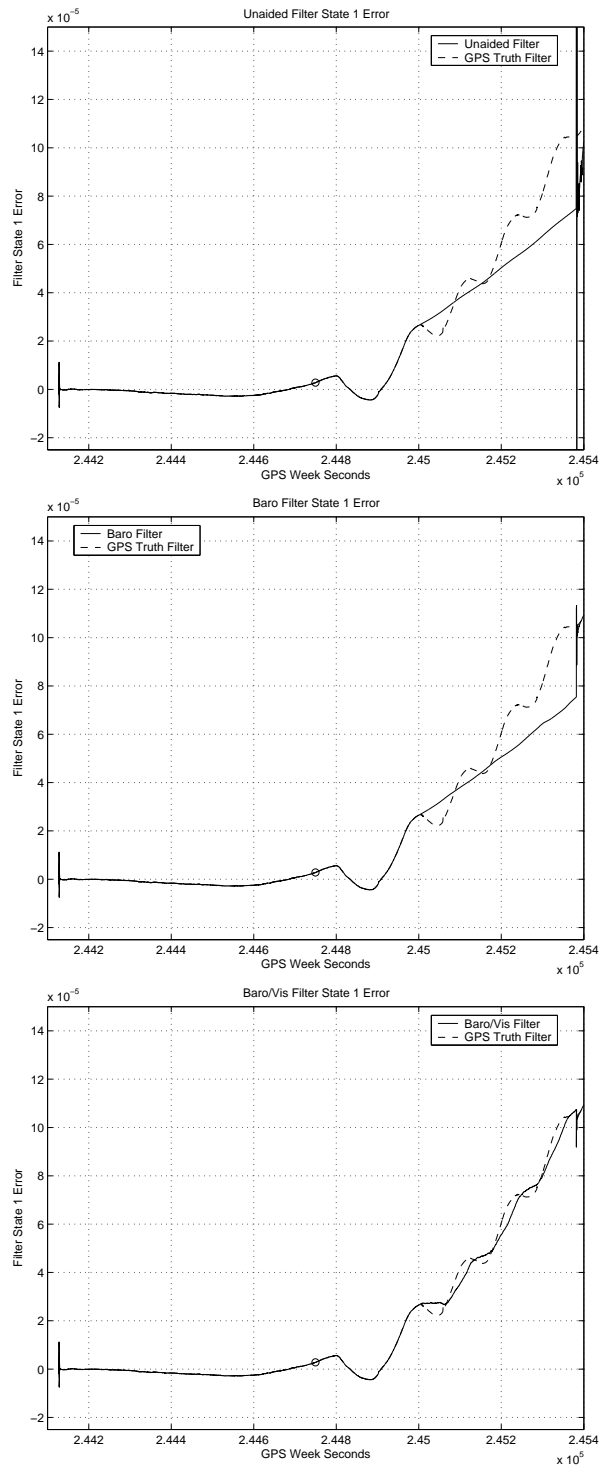


Figure 4.15 State 1 (East) Position Error for Unaided Filter (top), Baro Filter (middle), and Baro/Vis Filter (bottom)

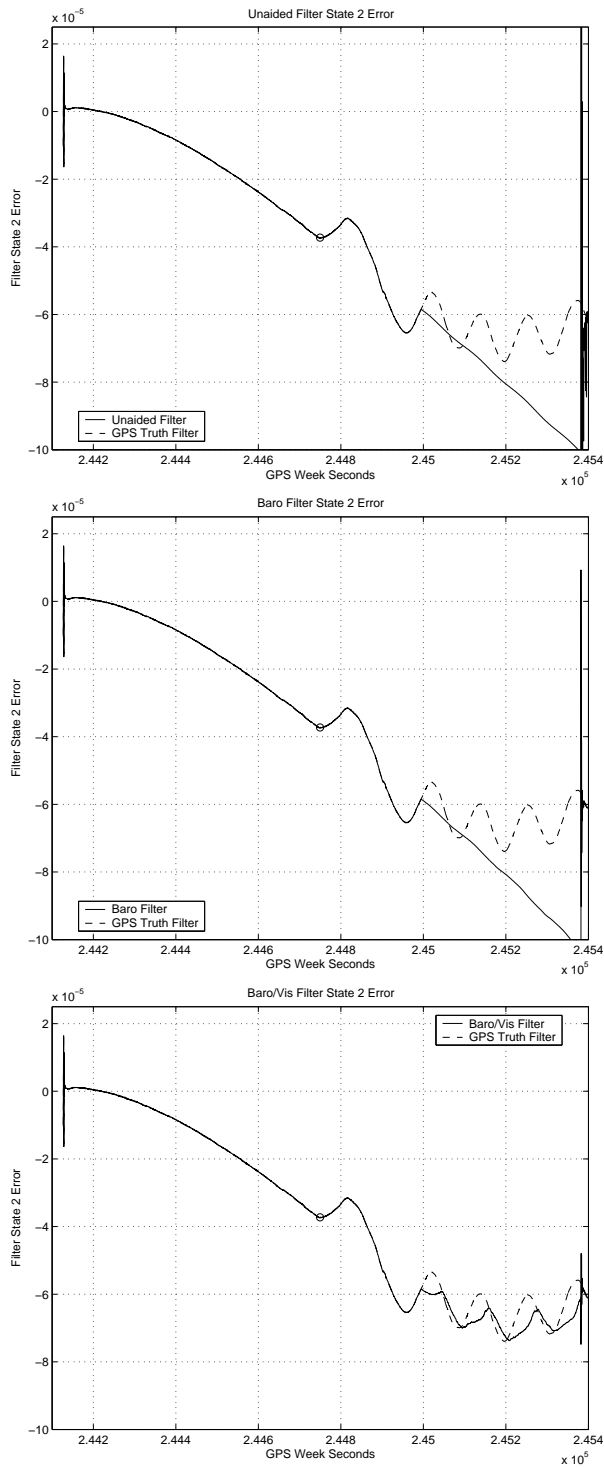


Figure 4.16 State 2 (North) Position Error for Unaided Filter (top), Baro Filter (middle), and Baro/Vis Filter (bottom)

when the GPS signal is again available, as compared to the much smaller position disparity for the Baro/Vis filter. Position error for State 3 (Down position error) is not shown since the GPS, Baro, and Baro/Vis filters all appear to perform similarly. The Unaided filter performance is much worse than the other three, but this is to be expected. Also, the filter implementation is known to err in the vertical channel, so this channel is not analyzed here. The same argument is applicable to State 6, the Down velocity error. The North position error states are not much different in performance from the East channel. The Unaided and Baro filters yield worse performance than the GPS or Baro/Vis filter, but nothing else is significant to note when compared to the East channel.

#### *4.9 Velocity Comparison*

Next, a comparison is made between the North, East, and Down velocities of the Unaided, Baro, and Baro/Vis filters with respect to the GPS filter. The plots in this section are formulated similarly to those of Sections 4.7 and 4.8 except that the Unaided filter figures are all scaled differently, since this filter performs more poorly than the Baro or Baro/Vis filters.

The North velocity for the Unaided, Baro and Baro/Vis filters are shown in Figures 4.17, 4.18, and 4.19 respectively. The North velocity for the Unaided filter starts out approximately 10 times that of the Baro filter. The error is bounded about zero and appears to be converging back to that same value. The Baro filter performs much better than the Unaided filter initially, and is still performing better at the end of the navigation orbit. However, the Baro filter is divergent. The Baro/Vis filter performs much better than either of the other filters. Its errors are much smaller and not divergent at all. It is noisier (small amplitude noise) due to the many visual images incorporated into the filter. This can be seen in many of the plots produced throughout this thesis.

East velocity errors are very similar to the North errors. The Unaided filter error magnitude is several times larger than that of the Baro or Baro/Vis filters. The East velocity may be slightly divergent (this is based upon the local maximums in the positive direction). The Baro filter is clearly divergent, while the Baro/Vis filter error is much smaller than that of the other two filters and is not divergent.

Down velocity for the three filters is presented in Figure 4.19. The Unaided filter diverges immediately away from zero and the error increases in a linear fashion. The Baro filter and the Baro/Vis filter are similar in performance to each other. They appear to be slightly offset above zero, but are clearly not divergent over the time frame in question. As seen in Section 4.7, the visual measurements seem to offer no discernable advantage in the vertical channel.

The covariance plots on Figures 4.17, 4.18, and 4.19 indicated filter performance similar to the position error covariance plots discussed previously. The filter performances are not nearly as good as their own estimates. Divergent channels show divergence in their associated covariance, while channels that do not diverge reach a steady-state covariance value.

#### *4.10 Velocity State Error Estimate Comparison*

Next, the velocity error states are compared. The GPS filter is shown in each figure as a dashed line for comparison. All three of the velocities diverge away from zero for North velocity error. The Baro/Vis filter generates a larger estimated error than the Unaided or Baro filters. The Unaided and Baro filter estimates of their performance are approximately the same. These estimates do not agree with the actual errors that were generated in Section 4.9, so the filters are mis-estimating the velocity errors.

The East velocity error has all three of the filters behaving similarly initially. The Unaided and Baro filters maintain their bias throughout the remainder of the time frame of interest, while the Baro/Vis filter converges back toward zero. The

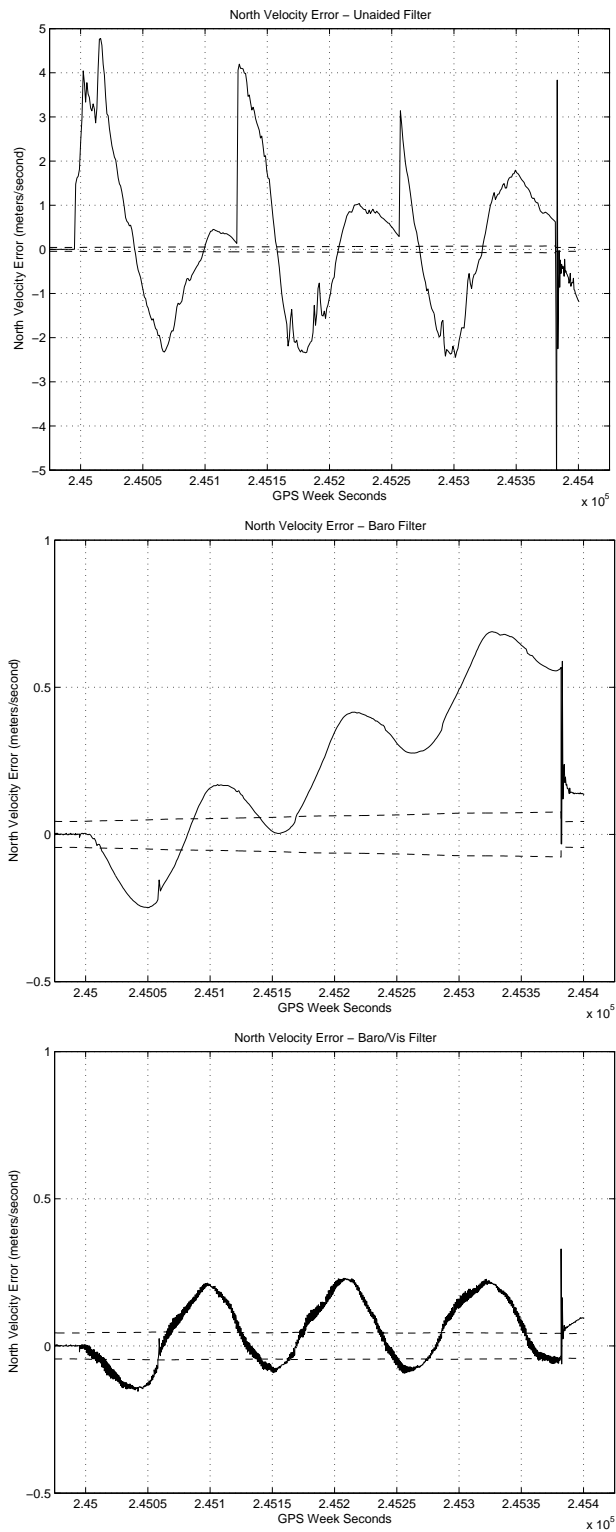


Figure 4.17 North Velocity Error for Unaided Filter (top), Baro Filter (middle), and Baro/Vis Filter (bottom). (Dashed Lines Indicate  $\pm 1\text{-}\sigma$  Filter-Compensated Covariance)

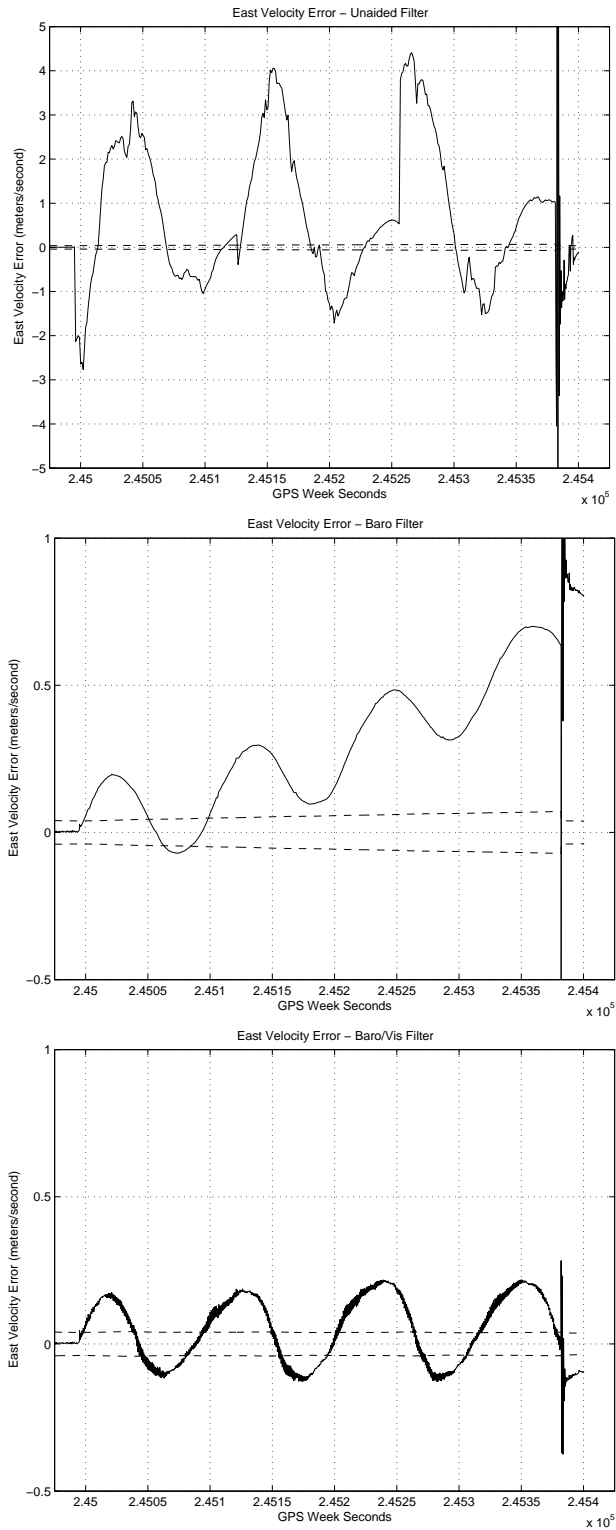


Figure 4.18 East Velocity Error for Unaided Filter (top), Baro Filter (middle), and Baro/Vis Filter (bottom). (Dashed Lines Indicate  $\pm 1\text{-}\sigma$  Filter-Compensated Covariance)



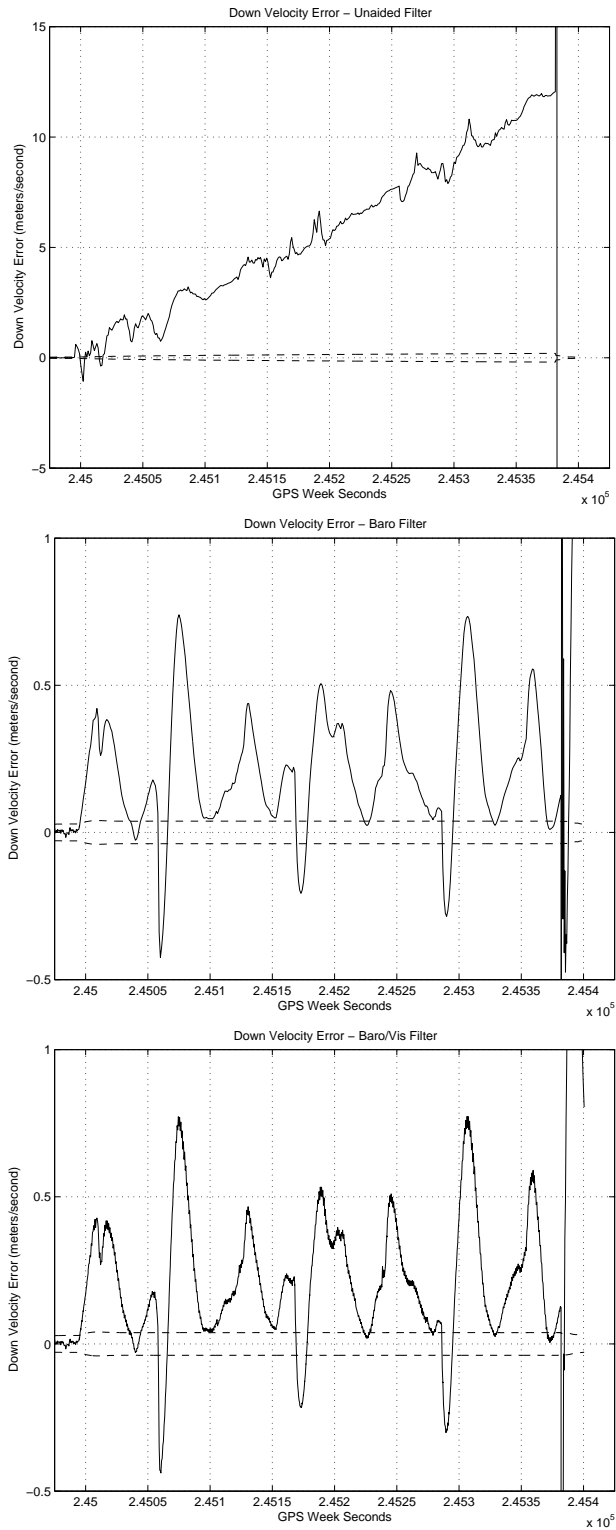


Figure 4.19 Down Velocity Error for Unaided Filter (top), Baro Filter (middle), and Baro/Vis Filter (bottom). (Dashed Lines Indicate  $\pm 1\text{-}\sigma$  Filter-Compensated Covariance)

navigation orbit occurs during the four oscillations on the right side of the plots for the GPS, Unaided, and Baro filters. The fact that the Unaided and Baro filters maintain their error offset is another indication that the filter improperly considers its model accuracy to be too high during a GPS outage. The filter is estimating its performance to be much better than it actually is.

#### 4.11 Visual Residuals

Measurement residuals provide indications of filter performance. The residuals are given by:

$$\mathbf{r} = \mathbf{z} - \mathbf{h}(\hat{\mathbf{x}}^-) \quad (4.1)$$

where  $\mathbf{z}$  is the measurement vector and  $\mathbf{h}(\hat{\mathbf{x}}^-)$  is the best prediction of the measurement before it arrives based on the measurement model vector.

Residuals should be white and Gaussian with a mean of zero and a covariance of  $[\mathbf{H}(t_i)\mathbf{P}(t_i^-)\mathbf{H}^T(t_i) + \mathbf{R}(t_i)]$  [6:229]. This is approximately true to first order for an extended Kalman filter. Figure 4.22 clearly shows that the residuals for this simulation do not exhibit these characteristics. This is probably due to a combination of modelling errors (both process model and measurement model), including nonlinear effects that the EKF linearization ignores and system errors not modelled in the filter (such as estimated target location error).

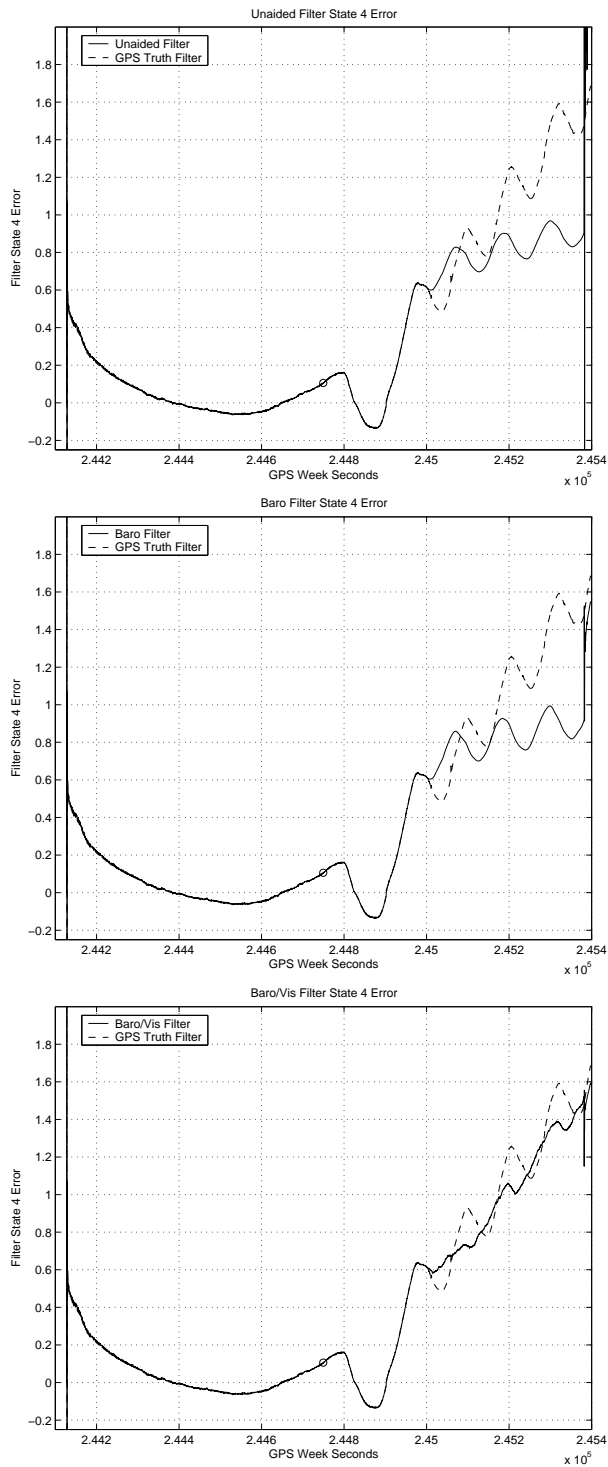


Figure 4.20 State 4 (North) Velocity Error for Unaided Filter (top), Baro Filter (middle), and Baro/Vis Filter (bottom)

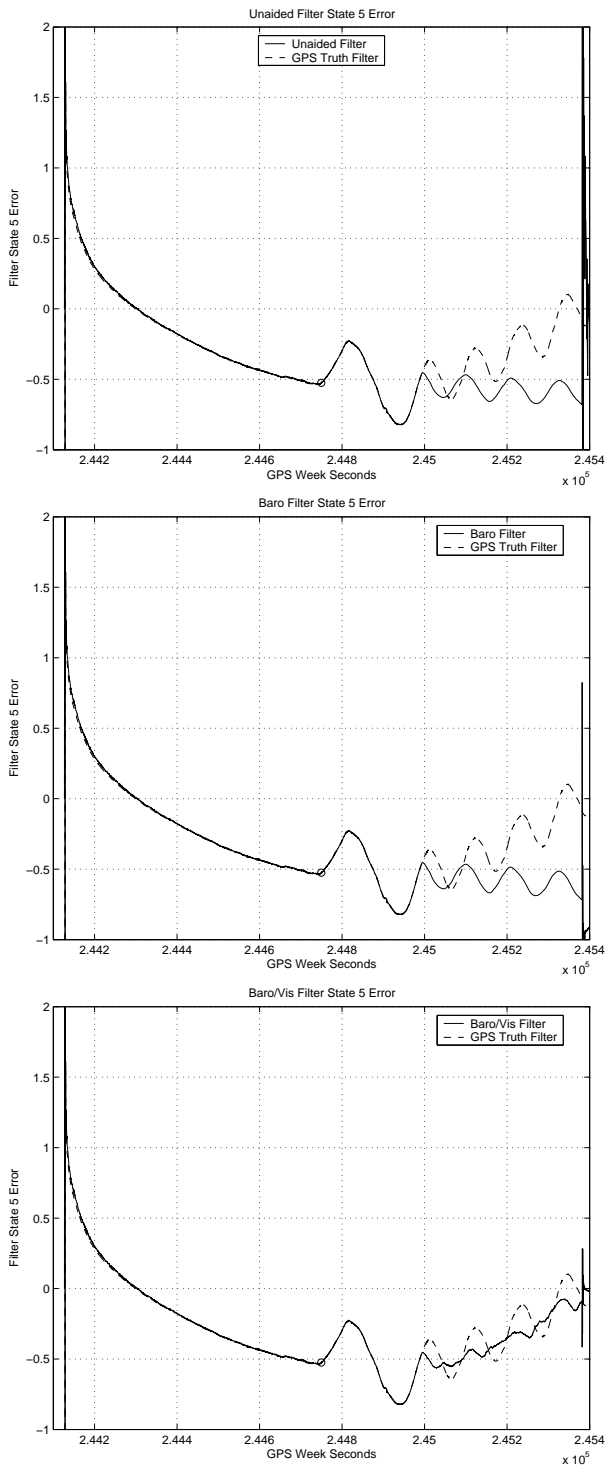


Figure 4.21 State 5 (East) Velocity Error for Unaided Filter (top), Baro Filter (middle), and Baro/Vis Filter (bottom)

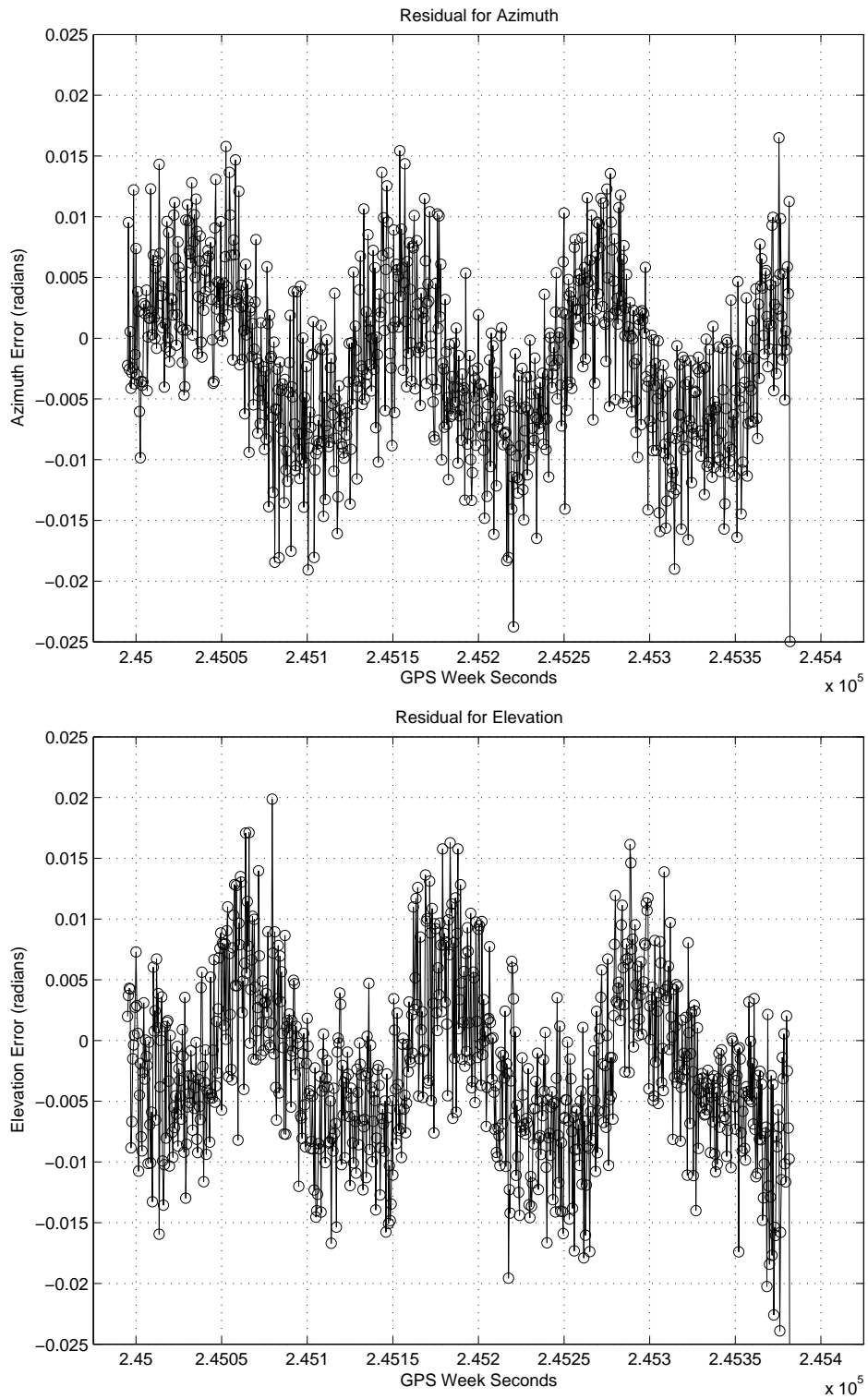


Figure 4.22 Visual Residuals for the Baro/Vis Filter

#### 4.12 **R** Sensitivity Analysis

A sensitivity analysis is conducted to determine the effect that the vision system's measurement error has on the Baro/Vis filter performance. Figure 4.23 shows Case 1 through Case 4 (described in Table 4.2), and the various levels of filter performance suggest other visual measurement  $\sigma_{meas}$  levels be investigated. The difference between Case 2 and Case 3 is quite significant. Case 2 is very slightly divergent, and has a maximum error of approximately 50 meters. Additional cases were run with different  $\sigma_{meas}$  values centered around Case 2, and then several values were chosen between Case 3 and Case 4. Cases 1 through 4, and the new sigma values under investigation along with their Case number are listed in Table 4.3.

Table 4.3 Additional Measurement Cases

Case	Case Description
Case 1	$\sigma_{meas} = 5 \times 10^{-13}$ (radians)
Case 1.5	$\sigma_{meas} = 0.0025$ (radians)
Case 2 (nominal)	$\sigma_{meas} = 0.005$ (radians)
Case 2.125	$\sigma_{meas} = 0.0106$ (radians)
Case 2.25	$\sigma_{meas} = 0.0163$ (radians)
Case 2.5	$\sigma_{meas} = 0.0275$ (radians)
Case 3	$\sigma_{meas} = 0.05$ (radians)
Case 3.10	$\sigma_{meas} = 0.1745$ (radians)
Case 3.20	$\sigma_{meas} = 0.349$ (radians)
Case 4	$\sigma_{meas} = 0.5$ (radians)

The results of all the  $\sigma_{meas}$  values are shown on Figure 4.24. The cost vs benefit analysis in Figure 4.25 is very useful for determining how much angular accuracy is required for a given position error. For example, an application that requires a 265m or smaller error could have an optical system with up to about 10 degrees of error. This information is strictly for this filter and the single data set used to generate the points.

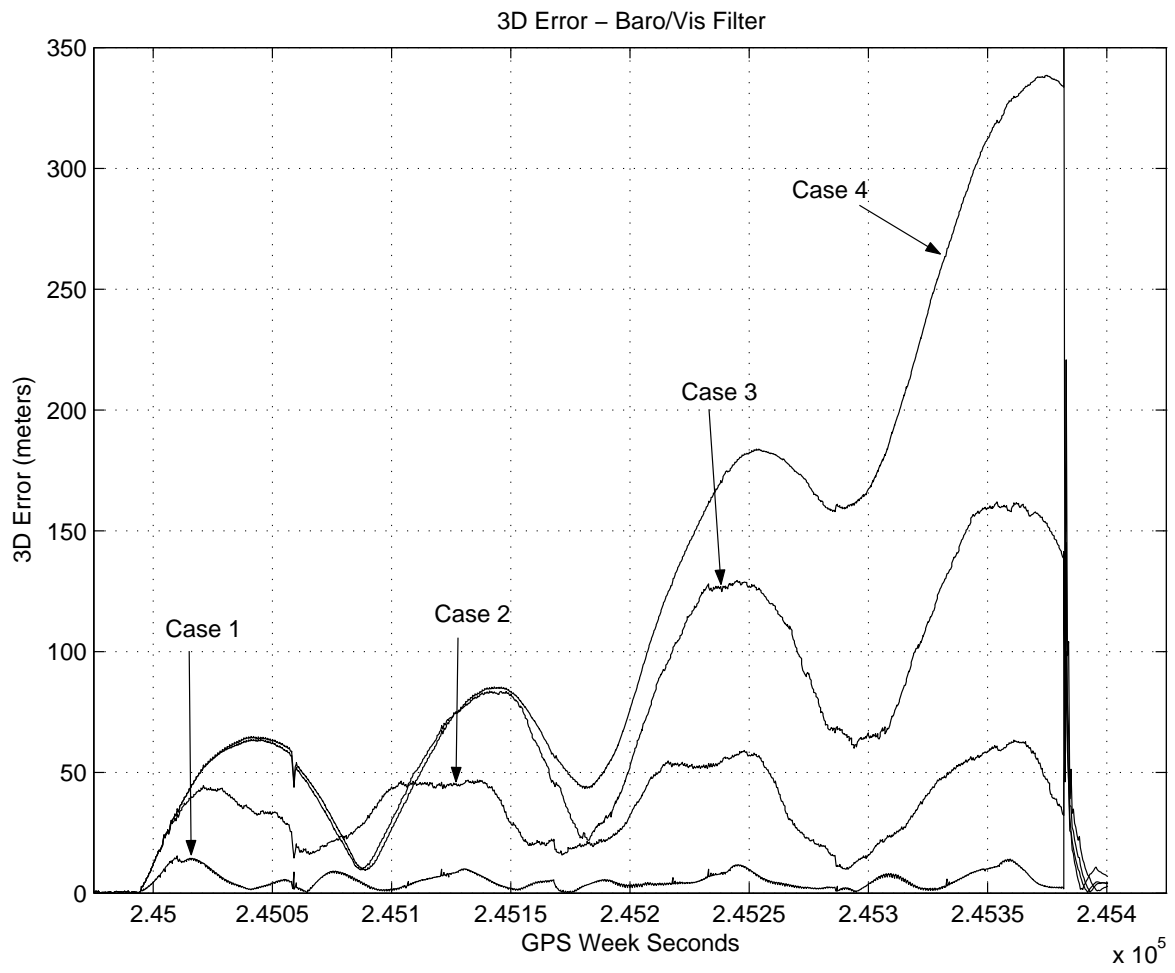


Figure 4.23 3D Position Error for Cases 1 through 4

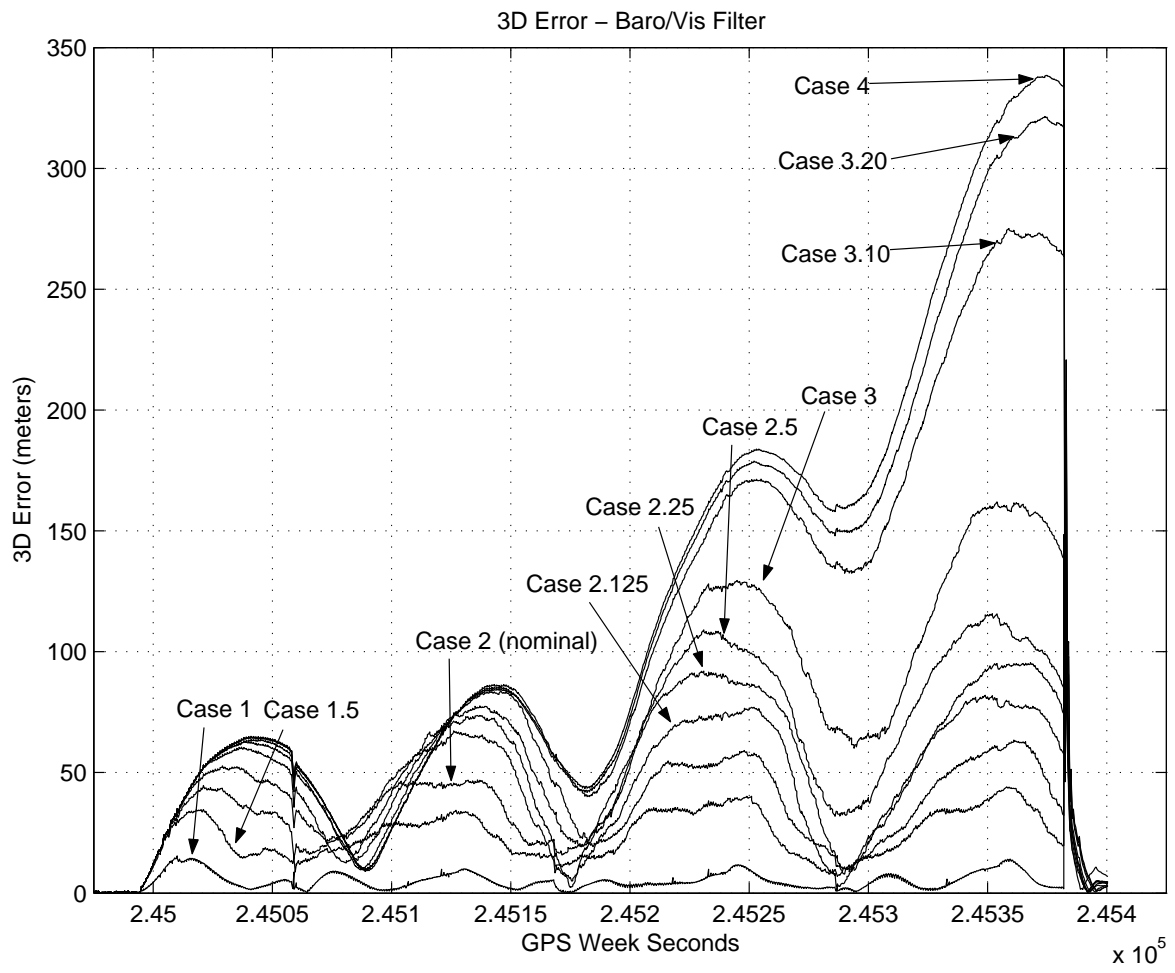


Figure 4.24 3D Position Error for All Cases



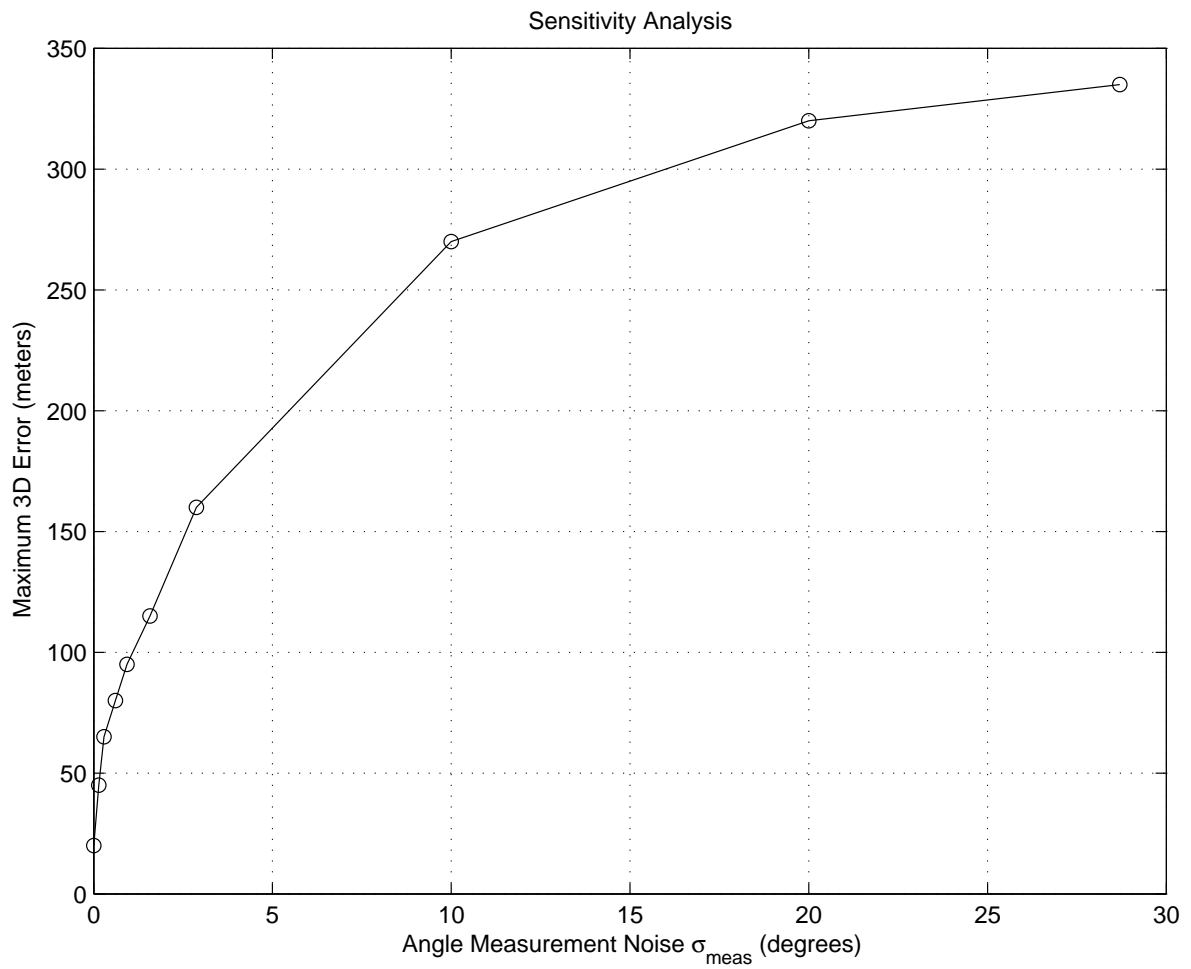


Figure 4.25 Case 2 — Cost vs Benefit for Baro/Vis Filter

#### 4.13 *Error Correlation with Angular Measurements*

Figure 4.26 shows north position error plotted in parallel with the azimuth and elevation angles. The data indicates there is correlation between the north error and the elevation angles. This is to be expected since the elevation angle is defined strictly in the north portion of the NED frame. All three of the local minimums for north error correspond roughly to zero for elevation. This would suggest that the north position errors grows as the elevation angle gets smaller and smaller. Then, as the elevation angle passes through zero and begins to grow larger, the north position error is corrected back toward zero. The three local maximums in north position error also occur when elevation error is passing through zero.

Figure 4.27 shows the same data for East position error as that previously shown in Figure 4.26 for North error. The data also indicates there is correlation between the east error and the azimuth angles. All three of the local maximums for east error correspond roughly to zero for azimuth, and all three of the local minimums correspond to the azimuth angle passing through zero as well. The north and east position error plots (Figure 4.28) are basically mirror-image versions of each other with about a 90 degree phase shift in them. This is consistent with the circular orbit being flown, and the slightly asymmetric nature of the plot may be due to the circular orbit actually being elliptical in nature due to wind effects on the aircraft.

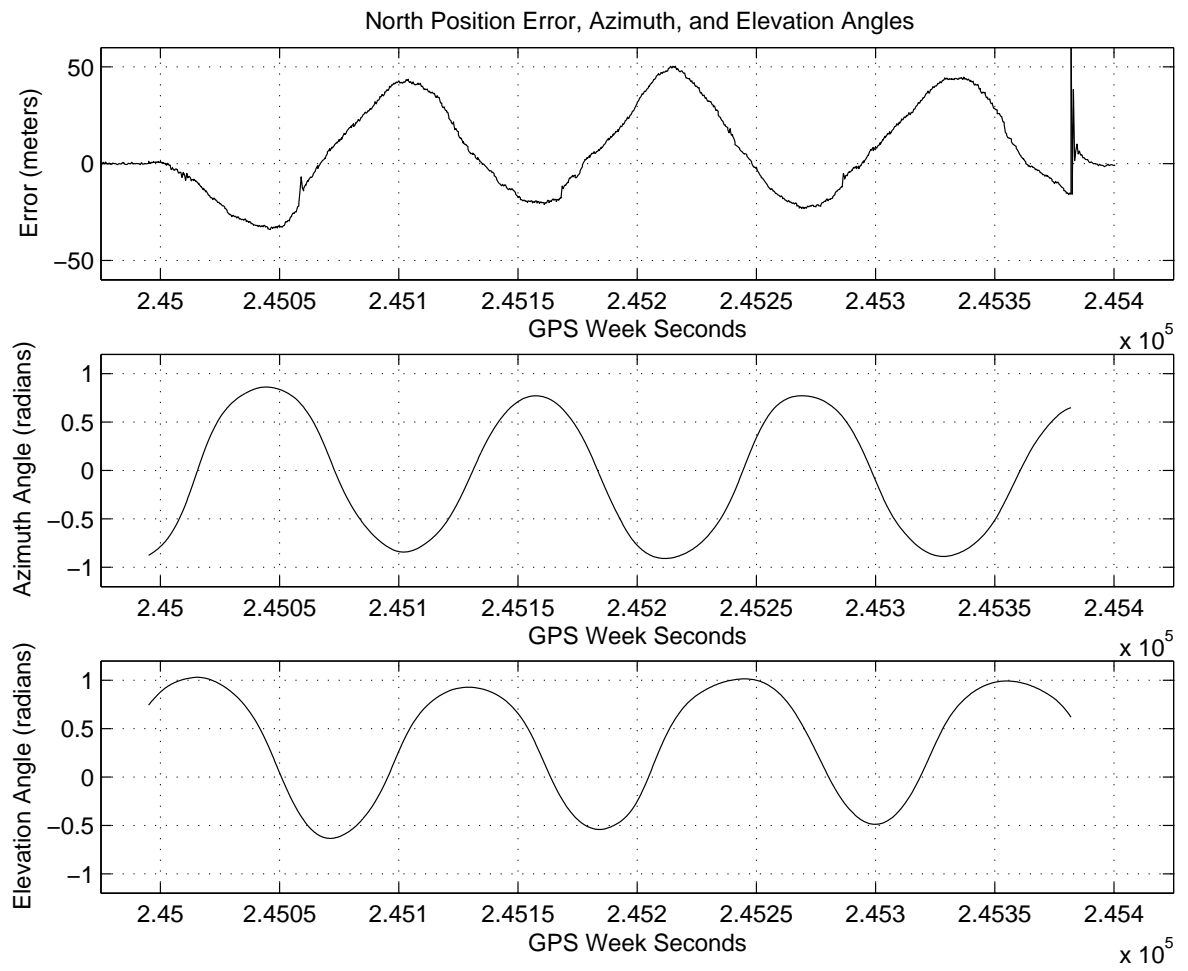


Figure 4.26 North Position Error and Angular Measurements

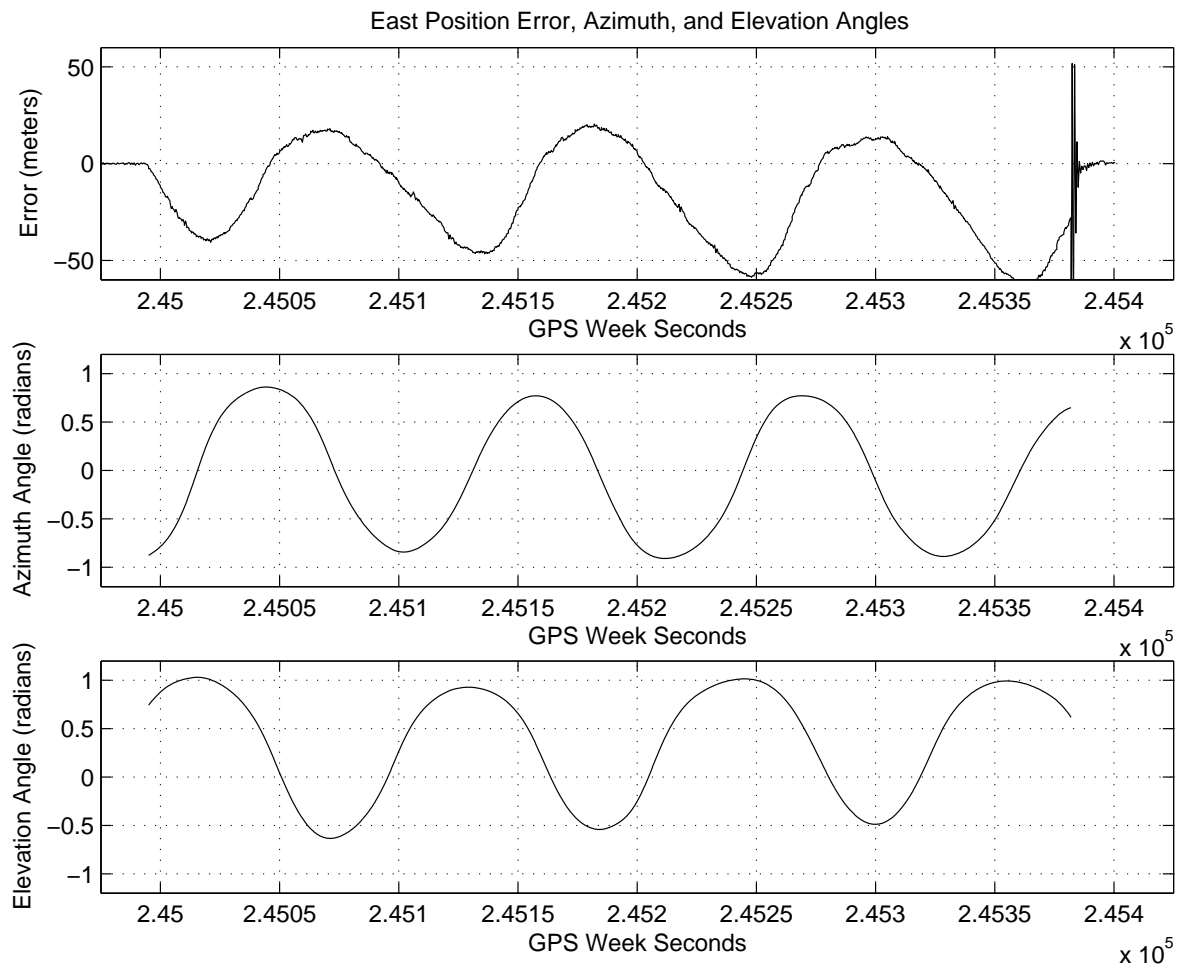


Figure 4.27 East Position Error and Angular Measurements

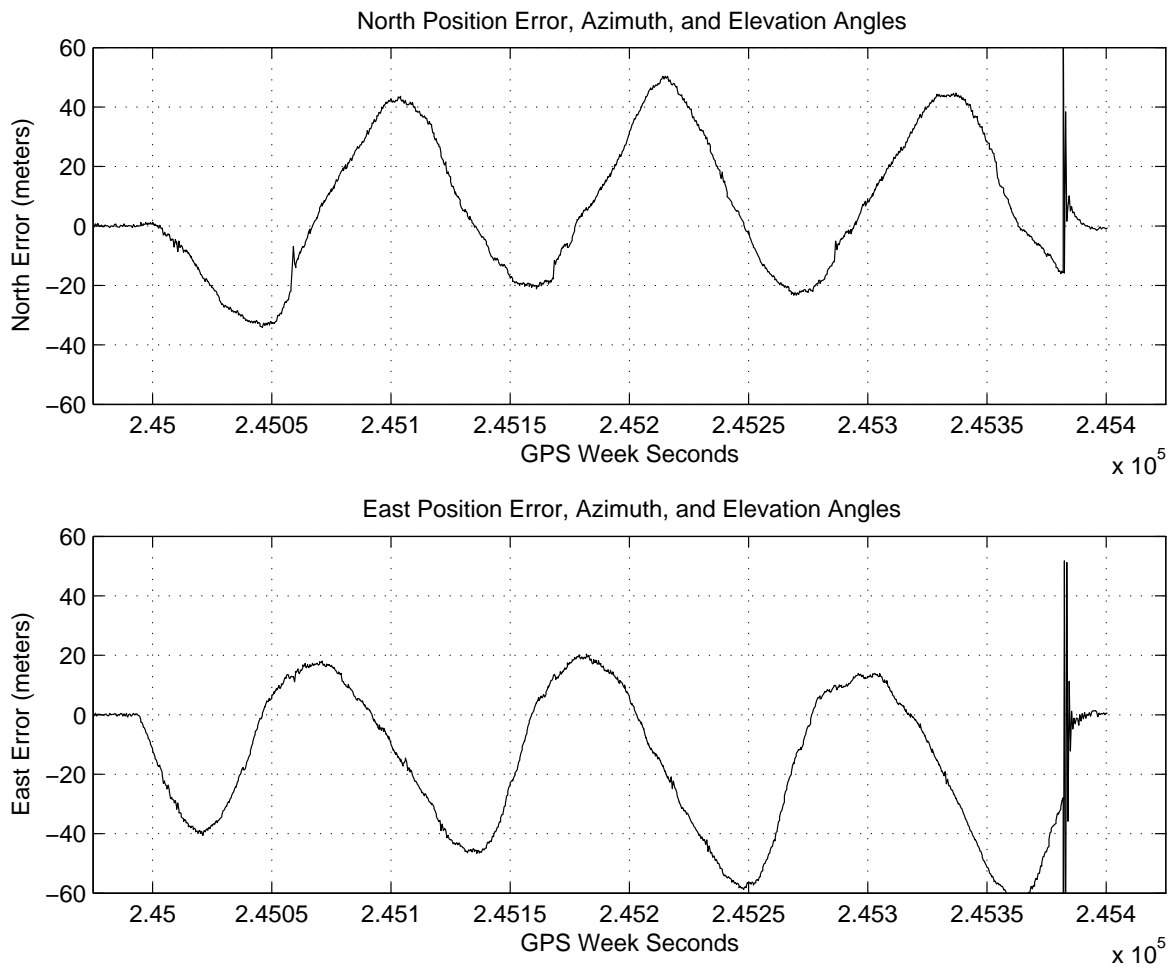


Figure 4.28 North and East Position Error

#### 4.14 Summary

A brief description was given for the sortie flown to collect the data used in this research, to include the navigation orbit where the brunt of the analysis occurred. The five filter configurations analyzed were explained. The perfect measurement case was shown to indicate the best possible results that could be expected from this implementation. Then, a case was analyzed in depth for the nominal error case of  $\sigma_{meas} = 0.005$  radians. The Baro/Vis filter clearly outperformed the Unaided and the Baro filters. The Vis filter also showed promising results. Residuals were discussed, as well as reasons for their clearly being non-white and time correlated. Lastly, a sensitivity analysis was performed for  $\mathbf{R}$  that generate a cost vs benefit curve.

## 5. *Conclusions and Recommendations*

### 5.1 *Conclusions*

The results generated in this research are clear as to the viability of using angular visual measurements for improving navigation accuracy. This was proved by incorporating “perfect” visual measurements which showed the maximum errors in this case were 20m. This is the best performance that can be expected from this formulation. Using a nominal value of visual measurement error (0.005 radians), the barometric/visual measurement filter showed performance was still quite good, as the maximum position error after the 6  $\frac{1}{2}$ -minute navigation orbit was 60m. Errors in the horizontal position and velocity channels were much better for the barometric/visual than for any of the other filters, when compared to the GPS filter. The visual measurements alone performed better than a filter with barometric measurements only during the navigation orbit (125m maximum error vs 340m maximum error respectively).

The simulation results should be valid, even though an actual camera was not used. If an camera is used, the INS tilt errors will have an effect on performance, but these errors grow slowly and are estimated in the filter. Therefore, tilt error effects can be estimated and removed, ensuring that visual measurements from a real camera can be used in a similar manner to that shown in this research.

### 5.2 *Recommendations*

The following recommendations are listed in order of importance (most important first):

1. Incorporate multiple simulated targets to determine the effect of more than a single measurement on navigation accuracy. An **R** sensitivity analysis should be performed for 2, 3, 4, and 5 targets for comparison with the single target

cost vs benefit curve provided in this thesis. This would provide invaluable information as to the level of angular measurement error that could be tolerated for different numbers of tracked targets.

2. Incorporate actual visual measurements into the filter. This needs to be accomplished to prove the above statement that implementing a camera into this research will not invalidate the method developed in this research.
3. Include target azimuth and elevation angles as states in the filter. This would allow for errors in the target coordinates ( $tgt_{lat}$ ,  $tgt_{lon}$ , and  $tgt_{alt}$ ) to be estimated and dealt with in the filter. An additional **R** sensitivity analysis should then be performed to determine how accurately the filter can passively determine target coordinates with different levels of angular measurement error. This should be accomplished for at least one to five tracked targets to match the preceding simulated measurement data.
4. Extend research to include DTED data so the planar image assumption can be removed from this research. This would allow for local changes in the earth's surface to be dealt with in the filter



## *Appendix A. Flight Test Methodology*

### *A.1 Overview*

The PEEPING TALON flight test actually supported two different efforts. The main focus of the project was the navigation section required for this research. Of secondary focus was a limited camera evaluation conducted on the forward and side-looking video cameras. The limited camera evaluation required much more video, under more varying conditions, so this portion of the project tended to drive sortie profile generation. This profile generation scheme was deemed appropriate since the navigation portion of each sortie was only ten minutes long and had more flexible data requirements.

### *A.2 Sortie Breakdown*

The limited camera evaluation had some unique lighting condition requirements that dictated where during the sortie the navigation section was placed. Sometimes the navigation portion was at the beginning of the sortie, and sometimes the navigation portion was placed in the middle or at the end of the sortie.

### *A.3 Prior to Flight*

The Ashtech GPS base station was setup in the TPS parking lot so data could be collected for use by an Ashtech proprietary program to turn the mobile Ashtech position solution into a truth source. This receiver typically collected data between 30 minutes and 1 hour prior to engine start until approximately 30 minutes to 1 hour after engine shutdown. This extra time before and after the sortie is so the Ashtech proprietary software has enough data to better characterize the errors present in the GPS signal.

#### *A.4 Pre-flight and Taxi*

The GAINR system required a pre-flight before each sortie. This was so the data card could be inserted into the system, and so the Range Group technicians could verify the system was working and the GPS was tracking satellites. The TPS special instrumentation (SI) technicians put the appropriate lenses on the cameras. Video was recorded from both cameras so the system could be verified as working properly prior to flight.

Once the aircraft engines were started the instrumentation master power was applied so the GAINR could begin alignment. This typically required between 4  $\frac{1}{2}$  to 6 minutes. The instrumentation power-on sequence was expedited due to the GAINR alignment requiring more time than that required to prepare the aircraft to taxi.

#### *A.5 Takeoff*

The video recorder was turned on prior to taking the runway for takeoff. After takeoff the side-looking camera was selected when turning around the Edwards AFB housing complex so easily identifiable points could be seen in the camera FOV. These points were then surveyed with an Ashtech GPS receiver to accurately determine their coordinates. This information was used to determine the camera-to-body DCM ( $C_c^b$ ) for that sortie.

#### *A.6 Navigation Portion of Sortie*

The main objective of the navigation portion of each sortie was to record a specific target area, continuously, for five minutes during a ten minute block of flight time. The requirement was for at least one measurement from each target intended for use be available every ten seconds over that five minute period. This would allow for visual measurements to be incorporated into the Kalman filter for at least five continuous minutes. The best way to do this was to fly a circular orbit around the

target area at a reasonable angle of bank. This was to keep the g-level at a low value for aircrew comfort, to make the flying task easy and repeatable, and so aircraft energy could be maintained without the need for a higher engine power setting. This last was due to the limited fuel capacity of the T-38 aircraft.

### *A.7 Lessons Learned*

As with any flight test venture, there were things that did not go as planned or that required some re-thinking. Some of these things are included here in the hope they might help follow-on efforts to avoid the same pitfalls.

*A.7.1 Ground Test.* It is very easy to expect things to work as planned, and therefore not to plan for unexpected events. It is quite natural for things to go wrong, especially when humans are involved.

The aircraft was modified well in advance of the beginning of flight test to allow extra time for problem resolution. The modular equipment (listed in Table A.1) was then removed from the aircraft so it could return to the general fleet. This was done so the equipment would not be inadvertently damaged. The modular equipment was then placed back into the aircraft and ground tested to ensure the system was working properly before the first flight. The ground test consisted of starting the aircraft engines, aligning the navigation systems, and taxiing down to the ATC tower and back to the same parking spot. Everything worked as advertised until the video tape was checked to see how the cameras handled the taxi. The tape was blank and it was determined the Radio Corporation of America (RCA) connectors from the cameras to the digital video recorder were never plugged into the RCA jacks. The first test mission would have provided no usable video data if this had not been discovered. This problem led to the implementation of a video check prior to each flight. During the aircraft pre-flight checks, video segments were recorded with each camera and checked to ensure proper operation prior to each flight.

Table A.1 Modular Aircraft Components

Ashtech GPS Receiver
Video Recorder
Forward-looking Camera
Side-looking Camera
Digital Video Recorder
LCD Monitor

*A.7.2 Station Keeping During Circling Navigation Maneuver.* The LCD monitor was intended for use as a secondary reference when flying the navigation portion of the sortie. The intent was to use it to ensure the target area remained in the side-looking camera FOV during the entire navigation orbit. It was unable to be used as a primary flight reference because it was not certified for that function.

It turns out the resolution on the LCD screen was not very good, so sometimes it was difficult to tell exactly what segment of the ground was being captured by the side-looking camera. The LCD monitor being rotated to the right and displaying information from a camera pointing out the right wing was not a very intuitive setup. One of the test pilots (Maj Bill "Ajax" Peris) came up with another way to tell where the camera was pointing. The pilot would set his seat to the height intended for use during flight, lower and lock the front canopy, and draw a border on the canopy that captured the same scene as that depicted on the LCD monitor. This way the pilot had a more intuitive means of station keeping on the target area by looking out the canopy rather than having to rely only on the off-axis displaying LCD monitor.

*A.7.3 Things Do Not Always Work The Way They Are Supposed To Work.*

It would seem that systems should work as they are reported to work. There were two instances during the test where systems failed to function normally.

The GAINR twice initialized in the wrong location. The start-up procedures were followed, and system indications were all normal. However, the GAINR initialized itself in the incorrect location and did not correct itself until sometime after

takeoff. These errors were correctable by running the data through the Range Groups MOSES Kalman filter program, but this added an additional \$2,000 data processing charge for each sortie.

The GAINR did not align during taxi as advertised. The PEEPING TALON program manager specifically asked Range Group personnel if this capability existed, and was told that it did. Takeoff time was a critical factor on one of the night sorties, so the aircraft was taxied prior to GAINR alignment to save time. The GAINR ready light (indicating a properly aligned system) never illuminated before takeoff, so the rear seat occupant placed the system in record mode. No data was recorded to the internal data card. This error was not recoverable.

*A.7.4 Selected Target(s) Being Visible To Camera.* The initial target chosen was the Compass Rose on the dry lakebed in the Edwards AFB complex. It was chosen because it can easily be seen from the air, and there are multiple lines intersecting each other that were easily identifiable and would make good targets. Sortie 0 was not an actual test mission, but we were flying the test aircraft and decided to collect data. We orbited the Compass Rose and it turns out the target on the lakebed was only visible during certain portions of the orbit. At times the Compass Rose had excellent contrast against the lakebed, and at other times the it was completely lost in the image. A set of five buildings just to the west of the Compass Rose was noticed to bloom brightly in the image when the aircraft was across the circle from the sun. The target area was shifted so these buildings were in the center because they could be easily seen under almost all circumstances. These buildings were close enough to the Compass Rose so the original aircraft orbit would not be noticeably different than that originally planned.

## *A.8 Summary*

This was a brief overview of the PEEPING TALON flight test mission that generated the data being analyzed in this thesis. Sortie flow was presented along with some of the lessons that were learned when flying real world test missions. The next chapter analysis this data and presents the results obtained by incorporating visual measurements into a navigation Kalman filter.<sup>6</sup>

## Bibliography

1. Campani, Marco, Andrea Giachetti and Vincent Torre. "Optic Flow and Autonomous Navigation," *Perception*, 24:253–267 (1995).
2. Giebner, Michael G. *PEEPING TALON Test Report*. Technical Report, 2002.
3. Henderson, Paul E., "Development and Testing of a Multiple Filter Approach for Precise DGPS Positioning and Carrier-Phase Ambiguity Resolution."
4. Mathworks, The. "Matlab©," *version 6.5.0.180913a, Release 13* (June 18, 2002).
5. Mathworks, The. "Matlab©," *version 6.1.0.450, Release 12.1* (May 18, 2001).
6. Maybeck, Peter S. *Stochastic Models, Estimation, and Control Volume 1, 141-1*. Mathematics in Science and Engineering. Navtech Book & Software Store, republished with permission of author, 1994.
7. Maybeck, Peter S. *Stochastic Models, Estimation, and Control Volume 2, 141-2*. Mathematics in Science and Engineering. Navtech Book & Software Store, republished with permission of author, 1994.
8. Maybeck, Peter S. "Class Handout (Instructor Notes), EENG 765, Stochastic Estimation and Control I." Summer 2000.
9. Michael Bosse, W.C. Karl, David Castañon and Paul DeBitetto. "A Vision Augmented Navigation System," *IEEE*, 1028–1033 (1998).
10. of American Scientists, Federation. "AGM-158 Joint Air to Surface Standoff Missile (JASSM)," *Internet Website*, <http://www.fas.org/man/dod-101/sys/smart/jassm.htm> (2002).
11. of American Scientists, Federation. "AGM-158 Joint Air to Surface Standoff Missile (JASSM)," *Internet Website*, <http://www.fas.org/man/dod-101/sys/smart/jsow.htm> (2002).
12. of American Scientists, Federation. "Joint Direct Attack Munition (JDAM), GBU-29, GBU-30, GBU-31, GBU-32," *Internet Website*, <http://www.fas.org/man/dod-101/sys/smart/jdam.htm> (2002).
13. Raquet, John F. "Class Handout, EENG 633, Advanced GPS Theory and Applications." Summer 2000.
14. Rogers, Robert M. *Applied Mathematics in Integrated Navigation Systems*. AIAA Education Series, American Institute of Aeronautics and Astronautics, Inc., 2000.

15. Silva, César and José Santos-Victor. "Direct Egomotion Estimation," *Proceedings of ICPR*, 702–706 (1996).
16. Silver, Howard A. *Algebra and Trigonometry*. Prentice Hall, 1986.
17. Technical Staff, The Analytic Sciences Corporation. *Applied Optimal Estimation*. The M.I.T.Press, 1974.
18. Titterton, D. H. and J. L. Weston. *Strapdown Inertial Navigation Technology*. Radar, Sonar, Navigation and Avionics Series 5, Peter Peregrinus Ltd., on behalf of the Institution of Electrical Engineers, London, United Kingdom, 1997.
19. Vega-Riveros, J. F. and K. Jabbour. "Review of Motion Analysis Techniques," *IEE Proceedings*, 136:397–404 (1989).



## *Vita*

Captain Michael G. Giebner was born and raised in Columbia, South Carolina and graduated from Spring Valley High School in 1983. He entered active duty with the Air Force as an Airman Basic via Lackland Air Force Base in 1984. After four years on active duty he remained at Charleston AFB, SC and joined the 707th Airlift Squadron of the Air Force Reserve where he transitioned to the C-141B as a flight engineer. He was a distinguished graduate of basic flight engineer school during his upgrade training in the C-141 program.

After becoming operationally qualified on the C-141B, he entered Clemson University to study electrical engineering. He graduated Cum Laude from Clemson in 1994 while maintaining C-141B mission qualification, flying during Desert Storm/Desert Calm/Provide Comfort and many other real world missions all over the globe.

He re-entered active duty with the Air Force through Officer Training School where he was a distinguished graduate. After commissioning he was assigned to the 422nd Test and Evaluation Squadron, Nellis AFB, NV. He spent four years as an F-16 flight test engineer with the 422nd before being assigned to the Integrated Avionics Test Facility at Tyndall AFB, FL. He applied for, and was accepted to, the AFIT/Test Pilot School education program in 2000.

He entered the Air Force Institute of Technology master's degree program in August of 2000. He completed the required AFIT coursework in September 2001 and was re-assigned to USAF Test Pilot School in January 2002. His thesis project was one of four flight test projects during the Test Management Program graduation exercises phase for TPS. This flight test was flown during October and November 2002. This thesis provides the final document required for him to earn his Master of Sciences Degree in Electrical Engineering. Captain Giebner is a graduate of USAF Test Pilot School class 02A.

REPORT DOCUMENTATION PAGE			Form Approved OMB No. 074-0188		
<p>The public reporting burden for this collection of information is estimated to average 1 hour per response, including the time for reviewing instructions, searching existing data sources, gathering and maintaining the data needed, and completing and reviewing the collection of information. Send comments regarding this burden estimate or any other aspect of the collection of information, including suggestions for reducing this burden to Department of Defense, Washington Headquarters Services, Directorate for Information Operations and Reports (0704-0188), 1215 Jefferson Davis Highway, Suite 1204, Arlington, VA 22202-4302. Respondents should be aware that notwithstanding any other provision of law, no person shall be subject to a penalty for failing to comply with a collection of information if it does not display a currently valid OMB control number.</p> <p><b>PLEASE DO NOT RETURN YOUR FORM TO THE ABOVE ADDRESS.</b></p>					
1. REPORT DATE (DD-MM-YYYY) 25-03-2002		2. REPORT TYPE Master's Thesis		3. DATES COVERED (From - To) Aug 2001 - Mar 2003	
4. TITLE AND SUBTITLE  TIGHTLY-COUPLED IMAGE-AIDED INERTIAL NAVIGATION SYSTEM VIA A KALMAN FILTER			5a. CONTRACT NUMBER		
			5b. GRANT NUMBER		
			5c. PROGRAM ELEMENT NUMBER		
6. AUTHOR(S)  Giebner, Michael G., Captain, USAF			5d. PROJECT NUMBER		
			5e. TASK NUMBER		
			5f. WORK UNIT NUMBER		
7. PERFORMING ORGANIZATION NAME(S) AND ADDRESS(S) Air Force Institute of Technology Graduate School of Engineering and Management (AFIT/EN) 2950 Hobson Way, Building 640 WPAFB OH 45433-7765			8. PERFORMING ORGANIZATION REPORT NUMBER  AFIT/GE/ENG/03-10		
9. SPONSORING/MONITORING AGENCY NAME(S) AND ADDRESS(ES) AFRL/MNGI (AFMC) DSN: 872-9443 x1290 Attn: 1Lt Virgil Zetterland e-mail: Virgil.Zetterland@eglin.af.mil Bldg A10, Eglin AFB, FL 32542-6810			10. SPONSOR/MONITOR'S ACRONYM(S)		
			11. SPONSOR/MONITOR'S REPORT NUMBER(S)		
12. DISTRIBUTION/AVAILABILITY STATEMENT  APPROVED FOR PUBLIC RELEASE; DISTRIBUTION UNLIMITED.					
13. SUPPLEMENTARY NOTES					
14. ABSTRACT <p>Inertial navigation systems and GPS systems have revolutionized the world of navigation. Inertial systems are incapable of being jammed and are the backbone of most navigation systems. GPS is highly accurate over long periods of time, and it is an excellent aid to inertial navigation systems. However, as a military force we must be prepared to deal with the denial of the GPS signal. This thesis seeks to determine if, via simulation, it is viable to aid an INS with visual measurements. Visual measurements represent a source of data that is essentially incapable of being jammed, and as such they could be highly valuable for improving navigation accuracy in a military environment.</p> <p>The simulated visual measurements are two angles formed from the aircraft with respect to a target on the ground. Only one target is incorporated into this research. Five different measurement combinations were incorporated into a Kalman filter and compared to each other over a six-minute circular navigation orbit. The measurement combinations included were with respect to the navigation orbit: 1) GPS signals throughout the orbit, 2) no measurements during the orbit, 3) simulated barometric measurements during the orbit, 4) simulated barometric and visual measurements during the orbit, 5) and visual measurements only during the orbit.</p> <p>The visual measurements were shown to significantly improve navigation accuracy during a GPS outage, decreasing the total 3-dimensional error after six minutes without GPS from 350m to 50m (with visual measurements). The barometric/visual measurement formulation was the most accurate non-GPS combination tested, with the pure visual measurement formulation being the next best visual measurement configuration. The results obtained indicate visual measurements can effectively aid an INS. Ideas for follow-on work are also presented.</p>					
15. SUBJECT TERMS Kalman Filtering, Navigation Aids, Inertial Navigation, Vision					
16. SECURITY CLASSIFICATION OF:			17. LIMITATION OF ABSTRACT	18. NUMBER OF PAGES	19a. NAME OF RESPONSIBLE PERSON
a. REPORT	b. ABSTRACT	c. THIS PAGE			Michael G. Giebner, Capt, USAF (ENG)
U	U	U	UU	114	19b. TELEPHONE NUMBER (Include area code) (661) 816-6830; e-mail: mikegiebner@mindspring.com